A measurement of parity-violating asymmetries in the G^0 experiment in forward mode

Thesis by
Silviu Doru Covrig

In Partial Fulfillment of the Requirements
for the Degree of
Doctor of Philosophy

California Institute of Technology
Pasadena, California

2004

A measurement of parity-violating asymmetries in the G^0 experiment in forward mode

by

Silviu Doru Covrig

Submitted to the Department of Physics
on September 28, 2004, in partial fulfillment of the
requirements for the degree of
Doctor of Philosophy

Abstract

The G0 (or G^0) experiment in Hall C at Jefferson Lab measures the parity-violating asymmetry in elastic electron scattering off hydrogen and quasielastic electron scattering off deuterium in the Q^2 range from 0.1 to 1 $(GeV/c)^2$ in both forward and backward running modes by using a longitudinally polarized electron beam on unpolarized liquid targets. By measuring three independent asymmetries, one in forward running mode off liquid hydrogen and two in backward running mode, one off liquid hydrogen and one off liquid deuterium, the experiment aims to perform for the first time a complete separation and mapping of the strange vector form factors of the nucleon (G^s_M, G^s_E) and the isovector axial form factor ($G^e_A(T=1)$) in three Q^2 bins over the Q^2 range from 0.1 to 1 $(GeV/c)^2$. To complete the physics program in both forward and backward modes it will take about five years. To accomplish the forward running mode program some 100 C of data are needed. This thesis is based on 9 C of physics data taken during the first chekout of the G^0 apparatus during October 2002 - January 2003.

Thesis Supervisor: Professor Robert D. McKeown
Title: Professor of Physics

”What we cannot speak about we must pass over in silence.”

L. Wittgenstein

To my parents

Acknowledgements

I would like to take this opportunity and thank my advisor, Robert McKeown, for his support, understanding and guidance. I would like to extend my thanks to the whole Kellogg group at Caltech, people that have made my stay at Caltech a very pleasant experience.

I am very thankful to Greg Smith, my JLab advisor, for his support and guidance while at JLab. Greg's dedication to the G^0 target made my job that much easier.

I would like to extend thanks to the whole G^0 collaboration. Working in G^0 has been an interesting experience and I am greatful to all members of the collaboration for their dedication and creativity, which have been a source of inspiration for me.

For outstanding help with target activities I'd like to thank Hall C technical staff and Jefferson Lab's Polarized Target Group.

Contents

Chapter 1

Introduction and Theory

1.1 Introduction

The conception of an atomistic theory dates back to about 400 BC. It has been proposed by two Greek philosophers, Leucippus and Democritus (believed to be the disciple of Leucippus). According to their theory, matter is made of *atoms*, and nature is made of two things, atoms and the void that surrounds them. Atoms were conceived as indivisible, indestructible and massive elemental parts of matter. The atomic theory opposed the commonly held belief, among natural philosophers of that period, in monism that "everything is one". It is said that Plato disliked Democritus' atomistic conception so much that he wished to have all his books burned. Although Plato's dislike with atomistic theory may be apocryphal, he does not mention Democritus at all in his works (Democritus lived to be 90 and wrote some 70 books).

Democritus' philosophical speculations about the atomic nature of matter have been found to be correct in the sense that nowadays it is accepted in the scientific community that matter has atomic structure. It is somewhat of a historical perspective which objects have been called atoms in the sense of being indivisible or having no internal structure. In the XIX century, chemistry called atoms the elements of the periodic table. There were two discoveries in physics that showed that the chemical atom has internal structure: the electron, by Thompson in 1897, and the nucleus, by Rutherford in 1911. Subsequently, the nucleus has been found to have internal structure and the components of the nucleus have been named nucleons. There are two kinds of nucleons: protons and neutrons, and they have been found to have internal structure of their own. The components of nucleons are called quarks. The fragmentation of matter seems to end here.

Elucidating the structure of matter is hardly the whole story about how nature works in a theory. The interactions among matter's building blocks have to be described in the theory and quantitative predictions checked empirically through experiments. A string of quantum based theories have culminated with the advent in 1978 of the standard model (SM), which is considered to offer a correct, though incomplete, picture of the subatomic domain. At large distance scales a correct, though also incomplete, picture is considered to be offered by general relativity. In terms of interactions the SM describes the strong, electromagnetic and weak interactions in two formalisms, quantum chromodynamics (or QCD), which describes the strong interaction and the electroweak theory, which describes in a unified picture electromagnetic and weak interactions. The measurement presented here is described by the SM physics.

The rest of this chapter is organized in sections that address the motivation for the experiment, the parity-violating asymmetry formalism, the theoretical models touching on strange form factors of the nucleon, the experiments related to the G^0 measurement, and the G^0 physics program. Chapter 2 contains a description of the experimental apparatus used in the G^0 forward angle mode. Chapter 3 contains the analysis of the asymmetry data taken during the first engineering run with the G^0 apparatus set in the forward angle mode. There are three addenda at the end, the first one contains the studies done about summing asymmetries in the experiment, the second one contains the target density variations studies that were done over the two engineering runs in G^0, and the third one contains summary tables for background subtraction scheme.

1.2 Motivation

After discovering the atomic nucleus in 1911, Rutherford came to gradually realize that the positive charge inside nuclei is carried by a particle with about the same mass as a hydrogen atom. Around 1920 he named this particle proton, which means *first* in Greek. Among the static properties of a proton are its electrical charge of $+e$, where e is the negative charge of an electron, $1.6{\cdot}10^{-19}$ C, and spin of 1/2. The spin value makes the proton a fermion, and if the proton were to be structureless it should obey the Dirac equation. As predicted by the Dirac theory, a spin 1/2 structureless particle should have a magnetic moment $\mu_P = \frac{q\hbar}{2m_P}$, where q is the electrical charge of the particle and m_P is the mass of the particle. If a proton's mass and electrical charge are used, then μ_P is called the nuclear magneton (nm). The first measurement of the proton's magnetic moment was published by Stern and Frisch [1] in 1933. It came as a surprise that the measured value for μ_p was quoted as being between 2 and 3 nm. This was the first experimental evidence that the proton has internal structure, which is inconsistent with the predictions of Dirac's theory for pointlike spin 1/2 particles. Further evidence about the electromagnetic structure of the proton was provided in the 1950's by a SLAC group, coordinated by Hofstadter [2], who measured the proton charge and magnetic form factors.

In the SM the nucleon structure is described in terms of three constituent quarks, $|p\rangle = |uud\rangle, |n\rangle = |ddu\rangle$. A simple valence quark model has been successful in treating the nucleon in terms of only up and down quarks. In the valence model the sea quark degrees of freedom, associated with pairs of $\bar{q}q$, and the gluon degrees of freedom are considered inert. The constituent quarks of QCD have internal structure, though, associated with the sea quark degrees of freedom and gluons. There is no conservation law in the SM that prohibits the manifestation of quark sea degrees of freedom in the structure and subsequently in the properties of the nucleon. The lightest of the six quarks, different from the valence quarks of the nucleon, has the highest chances of being observed in the sea degrees of freedom of the nucleon. This quark is the strange quark.

The motivation for this experiment stems in part in experimental evidence for the presence of strange quarks in some properties of the nucleon (momentum, mass and spin) and in part in theoretical work that suggested that the strange quarks may be present in the electromagnetic structure of the nucleon. There are also three experiments that have reported results related to the strange-quark contribution to the electromagnetic structure of the nucleon, their results will be presented in section 1.5.

Direct detection of quarks in nucleons has been done through deep inelastic scattering (DIS) experiments. Strange quarks contribution to nucleon momentum can be inferred from deep inelastic neutrino scattering, while strange quarks contribution to nucleon spin can be obtained from polarized deep inelastic lepton scattering, employing electron and muon probes.

Individual quark structure functions can be measured through the DIS methods. If x is the Bjorken momentum fraction of the struck quark, $x = \frac{Q^2}{2M\nu}$ (where Q^2 is the 4-momentum transfer between the neutrino and the struck quark, M is the mass of the nucleon and ν is the energy of the virtual photon), then the unpolarized quark structure function for a quark q of flavor f is defined as

$$q_f(x) = q_f^+(x) + q_f^-(x) \tag{1.1}$$

where $q_f^+(x)$ and $q_f^-(x)$ are the probability of finding a quark of flavor f and Bjorken momentum fraction x with helicity parallel to the nucleon spin (+) or antiparallel (-).

If strange quarks are present in the nucleon then a reaction like: ν_μ + s $->$ μ^- + c, where the charm quark c subsequently decays semileptonically producing μ^+, yields

$\mu^-\mu^+$. In a similar manner the antineutrino is expected to produce pairs of $\mu^+\mu^-$ from an antistrange quark, $\bar{s}$. Measurements of $s(x)$ and $\bar{s}(x)$ have been performed [3] using this method and the results suggest that the strange and antistrange quarks each carry about 2% of the nucleon momentum in the range for Bjorken $x < 0.1$.

Measurements of the spin structure of the nucleon through polarized lepton DIS also provide evidence for the presence of strange quarks in the nucleon. In this kind of measurement longitudinally polarized leptons probe polarized targets with the spin either aligned with the incident lepton momentum or perpendicular to it. From these measurements the polarized structure function $g_1^N(x)$ can be mapped versus the Bjorken scaling variable x for both nucleons (N is the nucleon index, $N = p$ or n). The polarized structure function $g_1^N(x)$ is defined in terms of polarized quark structure functions, $\Delta q_{Nf}(x) \equiv q^+_{Nf}(x) - q^-_{Nf}(x)$, where the symbols are the same as in eq. (1.1), and N is the respective nucleon

$$g_1^N(x) = \frac{1}{2}\sum_f e_f^2 \Delta q_{Nf}(x) \tag{1.2}$$

where e_f represents the quark charge. If isospin symmetry is assumed, then $u_p(x) = d_n(x) \equiv u(x)$, $u_n(x) \equiv d_p(x) = d(x)$ and $s_p(x) = s_n(x) \equiv s(x)$. Using the notation

$$\Delta q \equiv \Delta q_p \equiv \int_0^1 [q_p^+(x) - q_p^-(x)]dx = \int_0^1 [q^+(x) - q^-(x)]dx \tag{1.3}$$

where q is one of the quarks (u, d or s), the first moment of the nucleons polarized structure function $g_1^N(x)$ can be determined with

$$\Gamma_1^p = \int_0^1 g_1^p(x)dx = \tfrac{1}{2}\left(\tfrac{4}{9}\Delta u + \tfrac{1}{9}\Delta d + \tfrac{1}{9}\Delta s\right) \tag{1.4}$$

$$\Gamma_1^n = \int_0^1 g_1^n(x)dx = \tfrac{1}{2}\left(\tfrac{4}{9}\Delta d + \tfrac{1}{9}\Delta u + \tfrac{1}{9}\Delta s\right) \tag{1.5}$$

The integrals from eqs. (1.4, 1.5) are called the Ellis-Jaffe sum rule [4] and can be expressed in terms of the SU(3) matrix elements of the axial vector currents: a_0, a_3 and a_8, which are defined as

$$\begin{aligned} a_0 &= \Delta u + \Delta d + \Delta s && (1.6) \\ a_3 &= \Delta u - \Delta d && (1.7) \\ a_8 &= \Delta u + \Delta d - 2\Delta s && (1.8) \end{aligned}$$

and the Ellis-Jaffe sum rule for proton becomes

$$\Gamma_1^p = \frac{1}{36}(3a_3 + a_8 + 4a_0) \tag{1.9}$$

Determining $\Gamma_1^{p,n}$ from experiment and combining them with the values for a_3, from neutron beta decay [5], and for a_8, from hyperon beta decay [6]

$$\begin{aligned} a_3 &= G_A(Q^2 = 0) = \Delta u - \Delta d = 1.2695 \pm 0.0029 && (1.10) \\ a_8 &= \Delta u + \Delta d - 2\Delta s = -0.6 \pm 0.12 && (1.11) \end{aligned}$$

a value for the strange quarks contribution to the nucleon spin can be extracted

$$\Delta s = -0.1 \pm 0.1 \tag{1.12}$$

Although there are uncertainties in this kind of extraction related to SU(3) breaking, the extrapolation of $g_1(x)$ to x = 0 and about its Q^2 evolution, it suggests a substantial contribution from the strange quarks to the nucleon spin in the context of the overall quark contribution to the nucleon spin, which is about 20%.

There is evidence of the strange-quark contribution to the mass of the nucleon from the studies of the $\pi - N$ sigma term, $\Sigma_{\pi N}$, [7]. Measurements of the isospin-even $\pi - N$

scattering amplitude can be extrapolated to the 4-momentum transfer $Q^2 = 2m_\pi^2$ (known as the Cheng-Dashen point), to obtain a value of $\Sigma_{\pi N}(2m_\pi^2)$ of about 60 MeV. The term can be corrected for Q^2 dependence and extrapolated from the Cheng-Dashen point to $Q^2 = 0$, yielding $\Sigma_{\pi N}(0) \sim 45$ MeV. On the other hand hyperon mass relations can be used to obtain a value for the quantity

$$\sigma = \frac{1}{2M_p} < p|\hat{m}(\bar{u}u + \bar{d}d)|p > \approx 25 MeV \tag{1.13}$$

where $\hat{m} \equiv \frac{m_u+m_d}{2}$. After SU(3) corrections are applied to σ its value gets to be $\sigma_0 \approx 35$ MeV. If there is no strangeness contribution to the nucleon mass, then $\Sigma_{\pi N}(0) = \sigma_0$. Gasser et al. concluded in a recent analysis [7] of this discrepancy that the solution may be in a contribution from the pair of $\bar{s}s$ to the nucleon mass of the order $m_s\langle p|\bar{s}s|p\rangle \sim 130$ MeV. Other analyses of this subject [8, 9] suggest that the uncertainty in the extracted value for the strange-quark contribution to the nucleon mass may be at a 100% level.

Kaplan and Manohar pointed out in 1988 [10] that while there seem to be experimental evidence for non-zero axial-vector and scalar strange-quark matrix elements in the nucleon $\langle p|\bar{s}\gamma_\mu\gamma_5 s|p\rangle$ and $\langle p|\bar{s}s|p\rangle$), there was no information at the time about the vector strange-quark matrix elements in the nucleon, $\langle p|\bar{s}\gamma_\mu s|p\rangle$. They suggested elastic neutral current experiments to extract such information. McKeown [11] and Beck [12] advanced the idea of using parity-violation in accessing the weak neutral current sector of the proton and extracting information about the vector strange-quark matrix element. This experiment is based on this method, of using parity-violation in elastic scattering of longitudinally polarized electrons from unpolarized targets.

1.3 Parity violating asymmetry

This section will tie together the measured observable in this experiment with the strange-quark contribution to the electromagnetic structure of the proton.

1.3.1 Parity intermezzo

Parity is a discrete symmetry of nature. The parity operator applied to a state represented in momentum space changes the sign of the momentum vector without affecting the spin of the state. Parity is also known as mirror reversal symmetry about the origin of the coordinate system. It is represented by a unitary operator whose square is unity, and so it has two eigenvalues (the unitary operator is hermitian and so its eigenvalues are real) ± 1.

Parity was considered an exact symmetry of all the known interactions until in 1956 Lee and Yang advanced the idea of parity nonconservation [13] in weak interactions to explain the so-called "theta-tau" puzzle (in which the same particle would decay to either two pions or three pions, and as pions are pseudoscalars with parity -1, parity would not be conserved). Experimental proof of parity nonconservation came about half a year latter with the published results of the now famous experiment of Wu et al. [14] on the beta decay of cobalt 60. Due to this finding Feynman lost a $50 bet, but the result in itself had far more reaching consequences in physics, one of them being that this experiment is possible.

It is interesting to note that at the time the idea of parity nonconservation was proposed in weak interactions there was an accepted theory of weak interactions, proposed by Fermi in 1933, and refined through the years. The Fermi theory had a vector-vector point interaction structure and so it predicted that parity is conserved in the weak interactions. It was not until the advent of the electroweak theory, which was formulated in the 60's that parity-violation will be contained in the theory through a V-A structure for the weak interaction.

1.3.2 The asymmetry

Elastic scattering of an electron, e, from a proton, p, is described to the first order by the Feynman diagrams in fig. (1-1). An incident electron of 4-momentum $k = (E, \vec{k})$ scatters from a proton at rest in the lab frame of 4-momentum $p = (M_N, \vec{0})$. The electron emerges from the interaction with 4-momentum $k' = (E', \vec{k'})$, and the proton with 4-momentum $p' = (E_N, \vec{p'})$. The scattering angles in the lab frame are θ_e for the electron and θ_N for the recoiled proton. In the interaction the electron and the proton exchange a boson that carries 4-momentum $q = (\nu, \vec{q})$. The invariant 4-momentum transfer in the reaction is defined as $Q^2 \equiv -q^2 = -q_\mu^2$. The exchange is described by the interference between two concurring interactions, electromagnetic, mediated by a photon, γ, and neutral weak, mediated by the a neutral weak boson, Z^0.

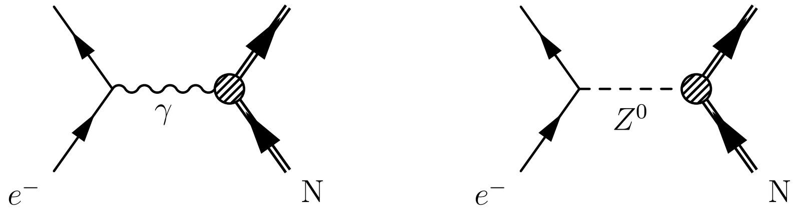

Figure 1-1: An electron e scatters from nucleon N exchanging virtual photon γ, left, and neutral weak boson Z^0, right.

The invariant amplitude associated with the diagrams in fig. (1-1) is given by the quantum interference between the invariant amplitudes associated with each individual diagram

$$\mathcal{M} = \mathcal{M}_\gamma + \mathcal{M}_\mathcal{Z} \tag{1.14}$$

Far from the Z^0 pole, in the range of low 4-momentum transfer, $Q^2 \sim 1(GeV)^2$, the electromagnetic interaction dominates by several orders of magnitude over the neutral weak interaction. A direct cross section measurement of the reaction in fig. (1-1) will completely obscure the effects of the neutral weak interaction in the measured observable. However, since the weak interaction violates parity, an observable can be formed that offers a direct glimpse into the neutral weak sector

$$A \equiv \frac{d\sigma_+ - d\sigma_-}{d\sigma_+ + d\sigma_-} \tag{1.15}$$

where $d\sigma_{+,-}$ are the helicity-dependent cross sections in elastic scattering of longitudinally polarized electrons from an unpolarized proton target. As the cross section is given by $d\sigma \propto |\mathcal{M}_\gamma + \mathcal{M}_\mathcal{Z}|^2$, the scale of the parity-violating asymmetry, defined in eq. (1.15), is given by $\frac{|\mathcal{M}_\mathcal{Z}|}{|\mathcal{M}_\gamma|} \sim \frac{Q^2}{M_\mathcal{Z}^2}$. The pseudoscalar observable defined by eq. (1.15) is called the parity-violating asymmetry and is measured in the G^0 experiment. In the conditions of this experiment, Q^2 less than 1 $(GeV)^2$, the asymmetry scale is 10^{-6} or parts per million (ppm).

Form factors formalism

The invariant amplitude associated with the photon exchange in fig. (1-1) is given by [15]

$$\begin{aligned} \mathcal{M}_\gamma &= e^2 \langle k' | \hat{j}^\mu_{l,\gamma} | k \rangle \frac{g_{\mu\nu}}{q^2} \langle p' | \hat{J}^\nu_{p,\gamma} | p \rangle & (1.16) \\ &= \frac{e^2}{q^2} g_{\mu\nu} j^\mu_{l,\gamma} J^\nu_{p,\gamma} & (1.17) \end{aligned}$$

where e ($e^2 = 4\pi\alpha$, α is the fine structure constant) is the coupling strength of the electromagnetic interaction, $g_{\mu\nu}$ is the metric tensor, $j^\mu_{l,\gamma} = \langle k' | \hat{j}^\mu_{l,\gamma} | k \rangle$ is the lepton electromagnetic vector current matrix element between lepton's initial $|k\rangle$ and final state $|k'\rangle$, and $J^\nu_{p,\gamma} = \langle p' | \hat{J}^\nu_{p,\gamma} | p \rangle$ is the hadronic electromagnetic current matrix element between proton's initial $|p\rangle$ and final state $|p'\rangle$. The electron is structureless and its electromagnetic current is given by the Dirac form [16]

$$j^{\mu}_{l,\gamma} = \bar{u}\gamma^{\mu}u \tag{1.18}$$

where u is a Dirac spinor for electron. The proton has internal structure and its electromagnetic current can be written in a general form that obeys current conservation, $\partial_{\mu}J^{\mu} = 0$, as [16]

$$J^{\mu}_{p,\gamma} = \bar{U}[F^{\gamma}_{1,p}\gamma^{\mu} + F^{\gamma}_{2,p}\frac{i\sigma^{\mu\nu}q_{\nu}}{2M_p}]U \tag{1.19}$$

where the functions $F^{\gamma}_{1,p}$ and $F^{\gamma}_{2,p}$ are called the proton Dirac and Pauli electromagnetic form factors respectively, and U is a Dirac spinor for proton. The form factors are functions of the invariant 4-momentum transfer, Q^2. The Dirac form factor is normalized to unity at $Q^2 = 0$, and the Pauli form factor is normalized to the proton's anomalous magnetic moment, $\kappa = \mu_p - \mu_P$ [17] (μ_P is the nuclear magneton defined earlier).

The invariant amplitude associated with the neutral weak boson exchange in fig. (1-1) is given by [18]

$$\begin{aligned} \mathcal{M}_{\mathcal{Z}} &= \frac{g^2}{16cos^2\theta_W}\langle k'|\hat{j}^{\mu}_{l,Z}|k\rangle\frac{g_{\mu\nu} - q_{\mu}q_{\nu}/M^2_Z}{q^2 - M^2_Z}\langle p'|\hat{J}^{\nu}_{p,Z}|p\rangle & (1.20)\\ &\approx -\frac{g^2}{16M^2_Z cos^2\theta_W}g_{\mu\nu}j^{\mu}_{l,Z}J^{\nu}_{p,Z}, \text{ in the limit } |q^2| \ll M^2_Z & (1.21)\end{aligned}$$

where g is the weak coupling strength, θ_W is the weak mixing angle, $j^{\mu}_{l,Z} = \langle k'|\hat{j}^{\mu}_{l,Z}|k\rangle$ is the lepton weak vector current matrix element, associated with the electron vertex in this case, and $J^{\nu}_{p,Z} = \langle p'|\hat{J}^{\nu}_{p,Z}|p\rangle$ is the hadronic weak vector current matrix element associated with the proton vertex. The weak coupling strength is given by [16] $\frac{g^2}{16M^2_Z cos^2\theta_W} = \frac{G_F}{2\sqrt{2}}$, where G_F is the Fermi constant. The invariant amplitude, $\mathcal{M}_{\mathcal{Z}}$, relevant for the G^0 experiment is the limit of low 4-momentum transfer for the propagator, $|q^2| = Q^2 \ll M^2_Z$, eq. (1.21) (the 4-momentum transfer in G^0 is less than 1 (GeV)^2 and M_Z is about 91 GeV). In electroweak theory the lepton neutral weak current if given by a V-A form [15]

$$j^{\mu}_{l,Z} = \bar{u}(q^l_V \gamma^{\mu} + q^l_A \gamma^{\mu}\gamma^5)u \tag{1.22}$$

where q^l_V, q^l_A are the vector and axial vector charges of the lepton (the electroweak charges are summarized in Table 1.1), and the hadronic neutral weak current is given by

$$J^{\nu}_{p,Z} = \bar{U}[F^Z_{1,p}\gamma^{\nu} + F^Z_{2,p}\frac{i\sigma^{\nu\mu}q_{\mu}}{2M_p} + G^{e,p}_A \gamma^{\nu}\gamma^5]U \tag{1.23}$$

where $F^Z_{1,p}, F^Z_{2,p}$ are the corresponding proton Dirac and Pauli weak form factors, which, like their electromagnetic counterparts, are functions of the 4-momentum transfer, Q^2, and $G^{e,p}_A$ is the proton neutral weak axial form factor as determined in electron scattering, also a function of Q^2.

Table 1.1: Electroweak couplings of charged fundamental fermions [15].

Fermion	q^{γ}	q^Z_V	q^Z_A
e^-, μ^-, τ^-	-1	-1+4$sin^2\theta_W$	+1
u, c, t	$\frac{2}{3}$	1$-\frac{8}{3}sin^2\theta_W$	-1
d, s, b	$-\frac{1}{3}$	-1+$\frac{4}{3}sin^2\theta_W$	+1

The electroweak elastic vector form factors of the proton, Dirac $F^{\gamma}_{1,p}, F^Z_{1,p}$, and Pauli $F^{\gamma}_{2,p}, F^Z_{2,p}$, contain the information about the electric and magnetic structure of the proton. Sachs et al. showed [19, 20] that the following linear combinations of the Dirac and Pauli form factors separates the electric from the magnetic structure

$$\begin{aligned} G_{E,p}^{\gamma,Z}(Q^2) &= F_{1,p}^{\gamma.Z}(Q^2) - \tau(Q^2)F_{2,p}^{\gamma,Z}(Q^2) && (1.24) \\ G_{M,p}^{\gamma,Z}(Q^2) &= F_{1,p}^{\gamma,Z}(Q^2) + F_{2,p}^{\gamma,Z}(Q^2) && (1.25) \end{aligned}$$

where $\tau_p(Q^2) = \frac{Q^2}{4M_p}$. The Sachs form factors, defined in eqs. (1.24, 1.25), represented in the Breit frame (in which $q^2 = -\vec{q}^2$, [21]) in the low 4-momentum transfer, Q^2, are the Fourier transforms of charge and magnetization distributions respectively of the proton. In the limit of $Q^2 \to 0$ the Sachs and axial form factors represent static electric, magnetic and axial properties of the proton (considering no-strangeness in the proton)

$$\begin{aligned} G_{E,p}^{\gamma,Z}(Q^2 \equiv 0) &= q_p^{\gamma,Z} && (1.26) \\ G_{M,p}^{\gamma,Z}(Q^2 \equiv 0) &= \mu_p^{\gamma,Z} && (1.27) \\ G_A^{e,p}(Q^2 \equiv 0) &= q_A^Z && (1.28) \end{aligned}$$

where $q_p^{\gamma,Z}$, $\mu_p^{\gamma,Z}$ and q_A^Z are the electromagnetic, weak and axial charges and magnetic moments of the proton, summarized in Table 1.2. The first derivative of the Sachs form factors with respect to the 4-momentum transfer represents the root-mean-square (rms) radius of the corresponding charge and magnetic distributions [21]

$$\begin{aligned} < r_{E,p}^2 > &= -6\frac{dG_{E,p}(Q^2)}{dQ^2}|_{Q^2=0} && (1.29) \\ < r_{M,p}^2 > &= -6\frac{1}{\mu_p}\frac{dG_{M,p}(Q^2)}{dQ^2}|_{Q^2=0} && (1.30) \end{aligned}$$

To connect the parity-violating asymmetry, defined by eq. (1.15), with the quark structure, the vector electromagnetic and neutral weak hadronic current operators of eqs. (1.16, 1.23), $\hat{J}^{\mu}_{p,\gamma}$ and $\hat{J}^{\mu}_{p,Z}$, are decomposed into quark flavor operators [15]

$$\begin{aligned} \hat{J}^{\mu}_{p,\gamma} &= \sum_f q^{\gamma}_f \bar{u}_f \gamma^{\mu} u_f & (1.31) \\ \hat{J}^{\mu}_{p,Z} &= \sum_f q^f_V \bar{u}_f \gamma^{\mu} u_f + \sum_f q^f_A \bar{u}_f \gamma^{\mu} \gamma^5 u_f & (1.32) \end{aligned}$$

where f is the quark flavor, and q^{γ}_f, q^f_V and q^f_A are the electroweak charges of quark flavor f, showed in Table 1.1. Similarly, Dirac and Pauli electromagnetic and neutral weak quark form factors can be defined, as well as axial quark form factors associated with the axial part of the neutral weak hadronic current of eq. (1.23). The Dirac and Pauli quark form factors can be combined into Sachs form factors using eqs. (1.24, 1.25), which are given by

$$\begin{aligned} G^{\gamma}_{E,M;p}(Q^2) &= \sum_f q^{\gamma}_f G^f_{E,M;p}(Q^2) & (1.33) \\ G^{Z}_{E,M;p}(Q^2) &= \sum_f q^f_V G^f_{E,M;p}(Q^2) & (1.34) \\ G^{e,p}_{A}(Q^2) &= \sum_f q^f_A G^f_{A,p}(Q^2) & (1.35) \end{aligned}$$

where $G^f_{E,M,A;p}$ are the quark form factors for proton, which are the same for the electromagnetic and the weak proton Sachs form factors. The quark-flavor sums in eqs. (1.33, 1.34) run over the three lightest quarks, up, down and strange (see the section on electroweak radiative corrections for the uncertainty associated with this approximation), and the antiquarks are implicitly included in the flavor form factors (quarks and antiquarks contribute with opposite signs to the flavor form factors, $G^f_{E,M,A;p}$).

The invariant amplitude for the elastic reaction in fig. (1-1), eq. (1.14), can be expressed in terms of the proton Sachs form factors. With the proton electromagnetic form factors determined from experiments, $G^{\gamma}_{E,p}(Q^2), G^{\gamma}_{M,p}(Q^2)$, to get to the quark contributions to the proton structure, six quark form factors, $G^f_{E,M;p}(Q^2), f = u, d, s$, and an axial form factor, $G^{ep}_A(Q^2) = G^e_A(Q^2)$, a total of five independent measurements have to be performed to completely separate the strange-quark form factors. This task can be greatly reduced if isospin symmetry is assumed (the distribution of a u-quark in a proton is the same as the distribution of a d-quark in a neutron and a sea quark has the same distribution in both the proton and the neutron), and the electromagnetic neutron form factors are also factored in from experiments, $G^\gamma_{E,n}(Q^2), G^\gamma_{M,n}(Q^2)$. Isospin breaking effects were determined to contribute less than 1% [22] to the electromagnetic form factors in parity-violating electron-proton scattering in the 4-momentum range relevant for this experiment. The neutron structure can be expressed similarly to the proton structure in terms of Sachs neutron form factors by changing the proton label p with the neutron label n in eqs. (1.24, 1.25). Also the neutron static electroweak properties are similarly given by eqs. (1.26, 1.27, 1.29, 1.30) by replacing the proton label p with the neutron label n.

Assuming isospin symmetry to be exact in what follows, then: $G^u_{E,M,A;p} = G^d_{E,M,A;n} = G^u_{E,M,A}$, $G^d_{E,M,A;p} = G^u_{E,M,A;n} = G^d_{E,M,A}$, and $G^s_{E,M,A;p} = G^s_{E,M,A;n} = G^s_{E,M,A}$, and the number of independent variables is reduced to three. In principle three different measurements are needed to separate the remaining independent variables, which, for the purpose of the G^0 experimental program are chosen to be G^s_E, G^s_M, and G^e_A.

Writing explicitly the proton and neutron Sachs form factors and the proton axial form factor, using eqs. (1.33, 1.34, 1.35) and isospin symmetry

$$G^{\gamma,p}_{E,M} = \frac{2}{3}G^u_{E,M} - \frac{1}{3}(G^d_{E,M} + G^s_{E,M}) \tag{1.36}$$

$$G^{\gamma,n}_{E,M} = \frac{2}{3}G^d_{E,M} - \frac{1}{3}(G^u_{E,M} + G^s_{E,M}) \tag{1.37}$$

$$G^{Z,p}_{E,M} = (1 - \frac{8}{3}\sin^2\theta_W)G^u_{E,M} - (1 - \frac{4}{3}\sin^2\theta_W)(G^d_{E,M} + G^s_{E,M}) \tag{1.38}$$

$$G^e_A = -(G^u_A - G^d_A) + G^s_A \tag{1.39}$$

In the limit of "no-strangeness", the axial proton form factor has an explicit isovector structure: $G_A^e = G_A^{e,T=1} = -(G_A^u - G_A^d) = -G_A\tau_3$, where T represents the total isospin quantum number and $\tau_3 = +1$ for p and -1 for n). From eqs. (1.36, 1.37, 1.38), the neutral weak proton form factors can be expressed as (eliminating the up and down quark form factors)

$$G_{E,M}^{Z,p} = (1 - 4\sin^2\theta_W)G_{E,M}^{\gamma,p} - G_{E,M}^{\gamma,n} - G_{E,M}^{s} \tag{1.40}$$

Analogous to the proton static limit of the Sachs form factors, eqs. (1.27, 1.29), the static limit of the strange-quark form factors are

$$\begin{aligned} G_E^s(Q^2 \equiv 0) &= 0 && (1.41)\\ -6\Big[\frac{G_{E,M}^s}{dQ^2}\Big]_{Q^2=0} &= < r_s^2 >_{E,M} && (1.42)\\ G_M^s(Q^2 \equiv 0) &= \mu_s && (1.43)\\ G_A^s(Q^2 \equiv 0) &= \Delta s && (1.44) \end{aligned}$$

where $< r_s^2 >_{E,M}$ is the nucleon rms strangeness charge/magnetization distribution radius, μ_s is the nucleon anomalous magnetic moment (explicitly carried in Table 1.2), and Δs is the strange-quark contribution to the nucleon axial form factor, the same quantity that appears in eqs. (1.6, 1.8) (also explicitly carried in Table 1.2). The proton and neutron electroweak static properties are summarized in Table 1.2. The value of $\sin^2\theta_W$

Table 1.2: Electroweak couplings of electron and nucleons [15].

	q^γ	μ^γ	q_V^Z	μ^Z	q_A^Z
e^-	-1	-1	-0.075	-0.075	+1
p	+1	2.79	0.075	2.08 - μ_s	-1.26 + Δs
n	0	-1.91	-1	-2.92 - μ_s	+1.26 + Δs

was taken from [5] for determining the electroweak couplings in Table 1.2.

Parity-violating asymmetry

At the tree level a form for the parity-violating asymmetry in elastic scattering of longitudinally polarized electrons from protons, eq. (1.15), can be obtained [15], taking into account the forms of the invariant amplitudes, eqs. (1.17, 1.21), and their explicit dependence on the proton form factors in the Sachs notation

$$\begin{aligned} A_p &= -\frac{G_F Q^2}{4\pi\alpha\sqrt{2}} \frac{\epsilon(\theta_e) G_E^{\gamma,p} G_E^{Z,p} + \tau_p G_M^{\gamma,p} G_M^{Z,p} - (1 - 4\sin^2\theta_W)\epsilon'(\theta_e) G_M^{\gamma,p} G_A^e}{\epsilon(\theta_e)(G_E^{\gamma,p})^2 + \tau(G_M^{\gamma,p})^2} && (1.45) \\ &= A_0 \frac{A_E + A_M + A_A}{\mathcal{D}_p} = A_0 \frac{\mathcal{N}_p}{\mathcal{D}_p} && (1.46) \end{aligned}$$

where $\epsilon(\theta_e) = [1+2(1+\tau_p)\tan^2(\theta_e/2)]^{-1}$, $\tau_p = Q^2/(4M_p^2)$, and $\epsilon'(\theta_e) = \sqrt{\tau_p(1+\tau_p)(1-\epsilon^2(\theta_e))}$ are kinematic quantities. The notations in eq. (1.46) are

$$\begin{aligned} A_0 &= -\frac{G_F Q^2}{4\pi\alpha\sqrt{2}} && (1.47) \\ A_E &= \epsilon(\theta_e) G_E^{\gamma,p} G_E^{Z,p} && (1.48) \\ A_M &= \tau G_M^{\gamma,p} G_M^{Z,p} && (1.49) \\ A_A &= -\epsilon'(\theta_e)(1 - 4\sin^2\theta_W) G_M^{\gamma,p} G_A^e && (1.50) \end{aligned}$$

where A_0 is a term that gives the scale of the asymmetry ($\sim 10^{-4}$ at a Q^2 of 1 GeV^2), A_E, A_M, and A_A are terms that contain cross products of electromagnetic and weak form factors of the proton, and $\mathcal{D}_p$, the denominator of eq. (1.46), is proportional with the electromagnetic invariant amplitude, eq. (1.17), squared.

The parity-violating asymmetry from eq. (1.45) depends of the 4-momentum transfer in the elastic reaction, Q^2, and the scattered electron angle in the lab frame, θ_e. The 4-momentum transfer in the elastic reaction $e-p$ is given in the electron coordinates and in the ultrarelativistic limit (the electron is massless compared to Q^2, $m_e \ll Q^2$) by

$$Q^2 = 4EE' \sin^2 \frac{\theta_e}{2}, \text{ where } E' = \frac{E}{1 + \frac{2E}{M_p} \sin^2 \frac{\theta_e}{2}} \tag{1.51}$$

Regardless of the experimental conditions the axial term A_A is naturally suppressed due to the multiplication with the electron weak charge $-(1 - 4\sin^2\theta_W)$. If the 4-momentum transfer is kept constant (manipulating the incident electron energy) and the scattered electron angle varies between 0 and π rad, the kinematic coefficients in eq. (1.45) make the parity-violating asymmetry sensitive to different cross terms of form factors. In very forward scattering ($\theta_e \to 0$), $\epsilon \to 1$ and $\epsilon' \to 0$, and the asymmetry is sensitive to the combination $A_E + A_M$, but no axial contribution. In very backward scattering ($\theta_e \to \pi$), $\epsilon \to 0$ and $\epsilon' \to \sqrt{\tau_p(1 + \tau_p)}$, and the asymmetry is sensitive to the combination $A_M + A_A$, and no electric contribution. This aspect of the parity-violating asymmetry dependence on kinematics is used experimentally to separate the electric and magnetic weak form factors (which are sensitive to the strangeness form factors, see eq. (1.40)) and the axial form factor, G_A^e, at the same Q^2.

The asymmetry in eq. (1.45) can be expressed in terms of vector strange electric and magnetic form factors using eq. (1.40)

$$A_p = A_0 \frac{A_E^0 + A_M^0 - \epsilon G_E^{\gamma,p} G_E^s - \tau_p G_M^{\gamma,p} G_M^s - (1 - 4\sin^2\theta_W)\epsilon' G_M^{\gamma,p} G_A^e}{\mathcal{D}} \tag{1.52}$$

where $A_E^0 = \epsilon G_E^{\gamma,p}[(1 - 4\sin^2\theta_W) G_E^{\gamma,p} - G_E^{\gamma,n}]$ and $A_M^0 = \tau_p G_M^{\gamma,p}[(1 - 4\sin^2\theta_W) G_M^{\gamma,p} - G_M^{\gamma,n}]$ are the “zero strangeness” terms of the parity-violating asymmetry defined by eqs. (1.48, 1.49).

The nucleon form factors are measured experimentally and their Q^2 dependence is found to be well approximated by dipole forms [23]

$$G_E^{\gamma,p}(Q^2) = G_D^V(Q^2),\ G_E^{\gamma,n}(Q^2) = -\frac{\mu_n \tau_n G_D^V(Q^2)}{1+\lambda_n \tau_n} \tag{1.53}$$

$$G_M^{\gamma,p}(Q^2) = \mu_p G_D^V(Q^2),\ G_M^{\gamma,n}(Q^2) = \mu_n G_D^V(Q^2) \tag{1.54}$$

$$G_A^e(Q^2) = q_A^Z G_D^A(Q^2),\ \text{where } G_D^{V,A}(Q^2) \equiv \Big(1+\frac{Q^2}{M_{V,A}^2}\Big)^{-2} \tag{1.55}$$

where the parameters are determined from fits to the data and have the values: $\lambda_n = 5.6$, the vector dipole mass $M_V^2 = 0.71\ (GeV)^2$ [23], and the axial vector dipole mass $M_A = 1.077 \pm 0.039$ GeV [24]. The Q^2 dependence of the nucleon form factors considered here was taken from [25], which employs phenomenological fits to the world data for $G_{E,M}^{\gamma,p,n}$, and from [26] for $G_M^{\gamma,p}$. For the purpose of this measurement the Q^2 dependence of the axial form factor was considered to be given by the dipole form of eq. (1.55). A conservative 3% uncertainty was assumed for each nucleon form factor over the Q^2 range covered in this measurement.

Electroweak corrections

At the tree level the parity-violating asymmetry of eq. (1.15) is given by eq. (1.52). The leading order in the invariant amplitude, eq. (1.14), can be corrected for higher-order effects such as electroweak radiative corrections and renormalization effects. Examples of representative diagrams for electroweak radiative effects are shown in fig. (1-2). Electroweak radiative corrections involving one quark in the hadronic state (as the examples in fig. (1-2)) can be calculated in the SM. Corrections involving many quarks in the hadronic state, where strong interactions are involved, are determined using hadronic models, as perturbative QCD does not apply in this energy range (at the scale of 1 GeV). In the decomposition of hadronic form factors into quark form factors, eqs. (1.33, 1.34, 1.35), the heavier quarks, c, b, t, were neglected. Heavy-quark renormalization of the light-quark current operators give rise to a class of hadronic corrections to the hadronic

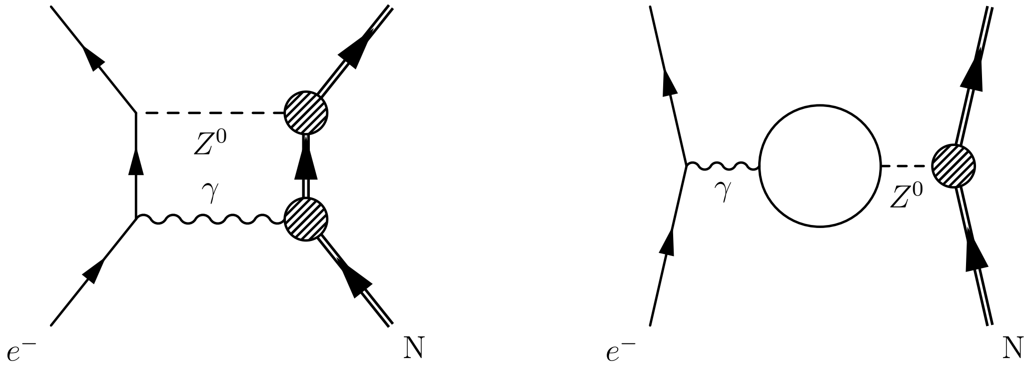

Figure 1-2: Examples of diagrams contributing to the electroweak radiative corrections, on the left "$\gamma - Z$ box", and on the right "$\gamma - Z$ mixing".

neutral current couplings. These corrections were computed in [10] and were found to be small: to the vector coupling $\Delta_V \leq 10^{-4}$, and to the axial-vector coupling $\Delta_A \approx -10^{-2}$.

Higher order effects have been integrated into corrective terms for the proton and neutron vector form factors, R_V^p and R_V^n

$$G_{E,M}^{Z,p} = (1 - 4\sin^2\theta_W)(1 + R_V^p)G_{E,M}^{\gamma,p} - (1 + R_V^n)G_{E,M}^{\gamma,n} - G_{E,M}^s \tag{1.56}$$

where the values for the corrective terms were taken from [15]: $R_V^p = -0.054 \pm 0.033$ and $R_V^n = -0.0143 \pm 0.0004$, the uncertainties represent estimated uncertainties in hadronic contributions.

The proton axial form factor, given at the tree level by eq. (1.39), will be noted: $G_A^Z = G_A^e = -G_A\tau_3 + \Delta s$. Beyond the tree level the axial form factor is corrected for electroweak radiative effects and its expression can be put in the form [29]

$$G_A^e = G_A^Z + \eta F_A + R_e \tag{1.57}$$

where $\eta = \frac{8\pi\sqrt{2}\alpha}{1-4\sin^2\theta_W}$, F_A is the nucleon anapole form factor [27] and R_e are radiative corrections. In parity-violating electron scattering the axial term, eq. (1.50), is suppressed in the leading order as mentioned earlier. The suppression of the leading order may yield a relative enhancement of the axial higher order effects compared to the leading order axial term in this kind of experiments. The anapole moment is defined as an effective parity-violating electromagnetic interaction in which along with a photon exchange between the electron and the nucleon a weak parity-violating hadronic interaction also occurs. The anapole operator is given by [29]

$$J_{p,\gamma}^{\mu,AM} \equiv \bar{U} F_A [G_F (q^2 \gamma^\mu - q^\nu \gamma_\nu q^\mu) \gamma^5] U \tag{1.58}$$

and adds to the hadronic electromagnetic operator of eq. (1.19). This definition of the anapole moment, F_A, differs from the one used in atomic parity-violation by a factor of $M_p^2 G_F$. The anapole effects are poorly constrained by theory and it is desirable that they get constrained by measurements, this being an integral part of the G^0 physics program, to be discussed in the section 1.6.

The measurement analyzed here was done with the G^0 apparatus in the forward angle mode, in which the axial contribution to the proton parity-violating asymmetry is kinematically suppressed. For this reason in this measurement the axial form factor was considered to be constrained by the relation

$$G_A^e = -(1 + R_A^p) G_A \tau_3 + (1 + R_A^{(0)}) G_A^s \tag{1.59}$$

where R_A^p represents the proton axial radiative corrections, and $R_A^{(0)}$ is the SU(3) singlet axial radiative corrections. R_A^p was found to be [28] dominated by its isovector part $R_A^{T=1} = -0.41 \pm 0.24$, where the uncertainty represents theoretical uncertainty in constraining the anapole moment corrections into R_A^p. The corrective term $R_A^{(0)}$ was absorbed in the strange axial form factor as there are no computations of it at the present.

1.4 Theoretical computations

This section touches on the theoretical approaches to quantitatively determine the strange-quark content of the nucleon. While considerable effort has been put into this, at present there is no compelling reason to take any particular calculation as definitive [30]. Theoretical approaches to the subject of presence of strangeness in the nucleon can be divided into two classes: methods that use first principles and methods that use hadronic models. The former class of methods encompasses lattice QCD, dispersion relations and chiral symmetry, the latter class encompasses a plethora of hadronic models. The scope of these methods is to connect theoretical ideas about how strangeness might be generated in the nucleon with quantities that can be inferred from measurement, like the static nucleon properties, the rms strange electric and magnetic radii and the strange magnetic moment of the nucleon, eqs. (1.42, 1.43), and, some methods also aim at describing the Q^2 dependence of the strange vector form factors. First principles methods and two classes of hadronic models will be presented in this section.

First principles methods

It has been pointed out that the direct application of perturbative methods may not apply in this context [31]. The strange quark is not heavy enough to use heavy quark effective theory, and, also, the strange quark may not be light enough to use SU(3) chiral perturbation theory (ChPT). The strangeness current can be expressed as [30]

$$\bar{s}\gamma_\mu s = J_\mu^B - 2J_\mu^{I=0} \tag{1.60}$$

where $J_\mu^B = \frac{1}{3}\bar{q}\gamma_\mu q$ is the baryon number, and $J_\mu^{I=0} = \bar{q}\frac{\lambda_8}{2\sqrt{3}}\gamma_\mu q$ is the isoscalar electromagnetic current. As the isoscalar electromagnetic current is known, there is no information about the baryon number or the SU(3) singlet current. Even if the chiral expansion can be carried out, experimental or theoretical input is needed in ChPT to make predictions about the static strangeness properties of the nucleon. The input can be obtained from experiments or from a different theoretical method, like lattice QCD. Though static nucleon strangeness properties cannot be directly predicted by ChPT, this theory can be used to predict the relative Q^2 dependence of the nucleon strange magnetic moment [33]

$$G_M^s(Q^2) = G_M^s(0) + \frac{M_N m_K}{24\pi F_\pi^2}(5D^2 - 6DF + 9F^2)f(Q^2)$$
$$\text{where } f(Q^2) = -\frac{1}{2} + \frac{1 + \frac{Q^2}{4m_K^2}}{2\sqrt{\frac{Q^2}{4m_K^2}}}\arctan\left(\sqrt{\frac{Q^2}{4m_K^2}}\right) \quad (1.61)$$

and where $G_M^s(0) = \mu_s$, eq. (1.43), m_K is the kaon mass, F_π is the pion decay constant, and F, D are the SU(3) axial coupling constants. If experimental input is available at non-zero Q^2, then a value for μ_s can be extracted using eq. (1.61).

Lattice QCD (LQCD) is a non-perturbative computational method in QCD based on Feynman path integral approach to quantum field theory. In this approach computations are performed on a lattice of spacetime through intensive use of numerical integrations. The present development in this field causes the LQCD computations of strangeness in the nucleon to be expensive and the extraction of meaningful results to be difficult. As an example: two recent LQCD computations of the Q^2 dependence of the strange vector form factors based on the quenched approximation have produced contrasting results [34, 35]. Until agreement is found among different LQCD computations it is not yet feasible to draw conclusions about the strangeness content of the nucleon based on LQCD. Although this is the situation at present, LQCD is the strongest candidate for sorting out among phenomenological models and for accurately determining the strangeness content of the nucleon.

The dispersion relation approach to form factors is based on causality, analyticity and unitarity. In the case of strangeness, the static properties are obtained by integrating the appropriate spectral function, which for rms radii is given by

$$< r_s^2 >_{E,M} = \frac{6}{\pi} \int_{t_0}^{\infty} \frac{ImG^s_{E,M}(t)}{t^2} dt \tag{1.62}$$

where $ImG^s_{E,M}$ is a spectral function, and t_0 is the lowest mass state that connects with $\bar{s}\gamma_\mu s$ (a 3π state in this case). The spectral function can be determined with experimental input from scattering amplitudes. Unfortunately with the present experimental data only the low mass end of the spectrum can be included in the spectral function [31], up to the state K^+K^-.

Hadronic models

In general all the models touching on strangeness content of the nucleon stem from one of the first principles methods and make successive approximations or assumptions to cover presently unknown domains in the original methods in order to reach quantitative results about nucleon strangeness. In what follows two general classes of models will be presented: hadronic models that use poles and hadronic models that use loops.

From a phenomenological point of view fig. (1-3) shows two physical processes that may contribute to the nucleon strangeness, generically called “loop” (the diagram on the left) and “pole” (the diagram on the right) effects. Nucleon strangeness is generated in a loop process by the physical separation between s and $\bar{s}$ quarks as the nucleon fluctuates into a kaon-hyperon pair. In a pole process it is the intermediate boson that fluctuates into a vector meson that generates strangeness in the nucleon. The poles method is based on an ansatz introduced in a dispersion relations approach. The ansatz, used [36] for analyzing the electromagnetic nucleon form factors, assumes that the spectral function for the isoscalar form factors in the Dirac and Pauli notation, eq(1.19), is dominated by vector mesons (VDM). In this approximation the spectral function is given by a sum of three Dirac delta distributions. Integrating the spectral function yields a sum of three

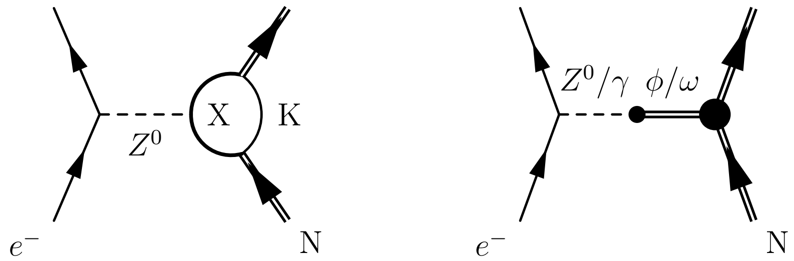

Figure 1-3: Examples of diagrams used to compute strangeness in the nucleon, from "loops" on the left, and from "poles" on the right, where X is a hyperon.

poles for the isoscalar form factors, $F_i^{T=0} \equiv (F_i^p - F_i^n)/2, i = 1, 2$

$$F_1^{T=0}(q^2) = F_1^{T=0} + \sum_V \frac{q^2 a_V^{T=0}}{m_V^2 - q^2} \tag{1.63}$$

$$F_2^{T=0}(q^2) = \sum_V \frac{m_V^2 b_V^{T=0}}{m_V^2 - q^2} \tag{1.64}$$

where the sums are made for the vector mesons ω, ϕ and a higher mass vector meson V'. At least two poles are needed to produce the Q^2 ($q^2 = -Q^2$) dependence of the form factors, eqs. (1.53 - 1.55), and an additional pole is introduced for improving the χ^2 for the fit. Evaluating the strange residues [37] at the ω, ϕ and V' poles yielded

$$\mu_s \approx -0.3, \quad < r_s^2 >_E \approx 0.2 fm^2 \tag{1.65}$$

While this computation of the strange magnetic moment of the nucleon hints for a sizable strangeness magnetism in the nucleon, the sign of the magnetic moment is different from the one extracted from experiment (see section 1.5.1).

Loop models basically stem from the ChPT. The ansatz here is to abandon the requirement for a consistent chiral expansion and assume that the strangeness contribution is given by a kaon loop. These models introduce a dipole regulator [38] in the chiral loop integrals involving baryons

$$F(q^2) = \Big(\frac{\Lambda^2}{\Lambda^2 - q^2}\Big)^2 \tag{1.66}$$

where Λ is a cutoff term, which is not predicted by the theory. Determination of the cutoff term introduces additional uncertainty in the results, and to the extent that the results are strongly dependent on the size of the cutoff they are generally viewed as uncertain. Various nucleon models have been used to determine the strangeness nucleon content in this approach. Among them: a model [39] that puts forth a $K\Lambda$ loop computation using phenomenological meson-baryon form factors (the same form factors used by the Bonn-J*ü*lich potential [41]), a model that employs a variant of the MIT bag model, the cloudy bag model (CBM) [42], and a hybrid model [43] that mixes VDM ideas with the $K\Lambda$ loop model. Loop models favor a negative rms strange charge radius, in contrast with a positive value from VDM, eq. (1.65). A summary of theoretical computational efforts is shown in Table 1.3, where NJL stands for Nambu-Jona-Lasinio, a variant of a constituent quark model that incorporates a NJL method [44], and, χQSM stands for chiral quark soliton model [46], which is an effective quark theory based on the instanton vacuum of QCD.

While there is a significant number of hadronic models that have yielded results for the static nucleon strangeness properties, there is no general agreement about the size or even the sign of such quantities. It may be that direct experimental input is needed to sort out among the models. In this respect G^0 offers a unique experimental perspective of separating out the strange vector form factors of the nucleon. With the constant progress being made in refining theoretical methods for computing strangeness content of the nucleon it is expected that in the near future fully model independent calculations will be available to compare with experimental values. Achieving this will yield a better understanding of the impact of the sea degrees of freedom into nucleon structure.

Table 1.3: Theoretical calculations of nucleon strange magnetic moment and strange charge radius.

Model	$< r_{E,s}^2 >$	μ_s
VDM [37]	0.2	-0.3
$K\Lambda$ [39]	-0.007	-0.35
CBM [42]	-0.011	-0.1
Hydrid [43]	-0.025	-0.3
χ quark [30]	-0.035	-0.09
Disp. Rel. [40]	0.42	-0.28
NJL-soliton [45]	-0.25 → -0.25	-0.05 → +0.25
χQSM [46]	-0.22 → -0.095	0.074 → +0.115
LQCD [34]	-0.36 ± 0.2	-0.16 → -0.06

1.5 Related experiments

The first experiment to measure a parity-violating asymmetry similar to the one defined by eq. (1.15) was carried out at SLAC in the 1970's [47]. The experimenters used a longitudinally polarized electron beam on liquid deuterium and liquid hydrogen targets. The measured asymmetry from deuterium at a 4-momentum transfer of $Q^2 = 1.6$ (GeV)^2 was in agreement with the value predicted by the electroweak theory, confirming the theory at the time.

Parity-violating experiments aimed at measuring the strange-quark electric and magnetic vector form factors of the nucleon through longitudinally polarized electron scattering have been performed at MIT-Bates, the SAMPLE experiment, at MAMI, the PVA4 experiment, and at Jefferson Lab, the HAPPEX experiment. These experiments are complementary to the G^0 experiment and will be briefly described in the reminder of this section.

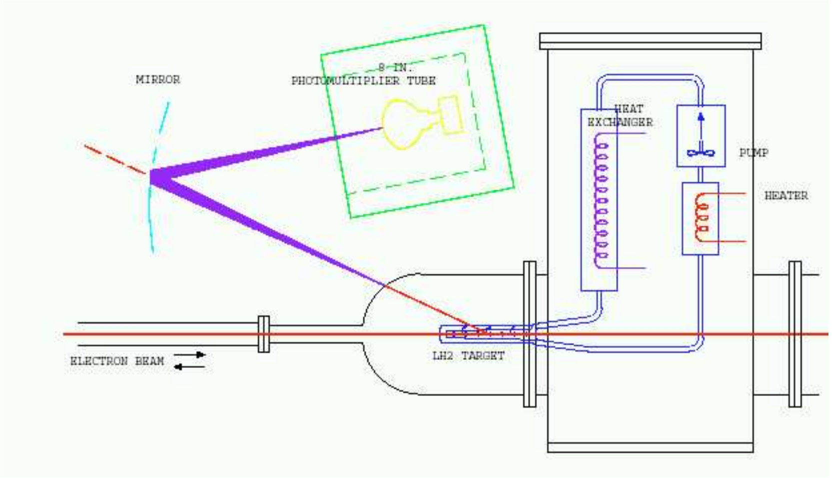

Figure 1-4: SAMPLE apparatus: 40 cm long recirculating cryogenic target and air Cerenkov detector with solid angle acceptance of 1.5 sr and mean scattering angle $< \theta_e >\sim 147^o$. The detector is made of ten ellipsoidal shaped mirrors facing ten 8 in PMTs. The detection is based on integrating the PMT signals.

1.5.1 SAMPLE

The first experiment to measure and extract results about a strange-quark vector form factor of the nucleon was SAMPLE experiment [48, 49] at MIT-Bates facility. A schematic of the experiment can be seen in fig. (1-4). SAMPLE used a 40 μA longitudinally polarized electron beam and made three measurements of the parity-violating asymmetry, eq. (1.15). The first measurement, in the summer of 1998, was on a liquid hydrogen target, eq. (1.45), with a beam energy of 200 MeV. The second measurement, in the summer of 1999, was on liquid deuterium, eq. (1.73), at the same beam energy. The third measurement, in the winter of 2001-2002, was on liquid deuterium, at a beam energy of 125 MeV. As SAMPLE apparatus is set for backward angle detection mode, the measured asymmetry is sensitive mostly to a linear combination of strange magnetic and axial form factors, eq. (1.46). The first two measurements were done at a $Q^2 = 0.091$ (GeV)^2 and the their results for G_M^s vs. $G_A^{e(T=1)}$ are superposed in fig. (1-5), along with the theory calculation for $G_A^{e(T=1)}$ from [28]. From the combined results between the hydrogen data

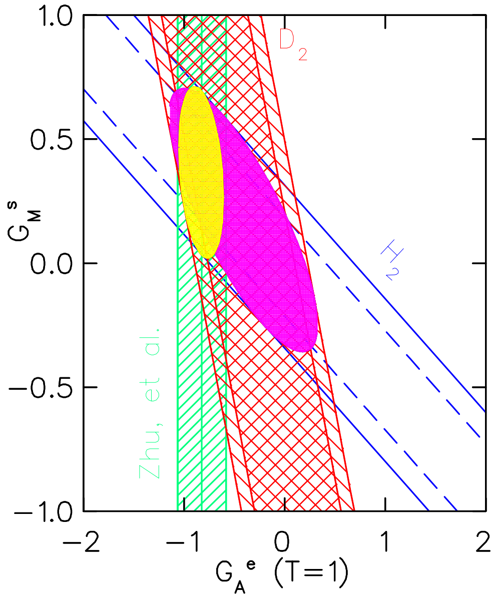

Figure 1-5: Combined SAMPLE results at $Q^2 = 0.091$ (GeV)^2. Displayed are the uncertainty bands. The small ellipse corresponds to 1σ overlap of the hydrogen data and the theoretical prediction, the larger ellipse corresponds to the overlap between the two data sets. The vertical bands correspond to the theoretical calculations of $G_A^{e(T=1)}$ from [28].

at $Q^2 = 0.091$ (GeV)^2 and the theoretical computation for $G_A^{e(T=1)} = -0.83 \pm 0.26$ from [28], SAMPLE extracted a value for the vector strange magnetic form factor of

$$G_M^s(Q^2 = 0.091) = 0.37 \pm 0.20 \pm 0.26 \pm 0.07 \tag{1.67}$$

where the uncertainties are statistical, experimental systematic, and, the last one, due to the uncertainty in the electroweak radiative corrections. This result can be extrapolated to a $Q^2 = 0$ (GeV)^2 with theoretical input [32] to obtain a value for the strange-quark magnetic moment of the nucleon

$$\mu_s = 0.37 \pm 0.20 \pm 0.26 \pm 0.15 \tag{1.68}$$

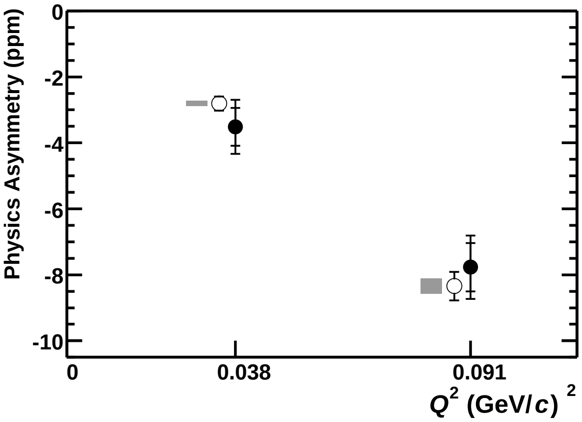

Figure 1-6: SAMPLE physics asymmetry results for the deuterium measurements versus Q^2 (solid circles). On the same plot are the theoretical predictions for these asymmetries with the $G_A^{e(T=1)}$ taken from [28], and assuming a $G_M^s = 0.15$ (open circles and offset Q^2 for clarity). The height of the shaded rectangles represents the change in the asymmetry corresponding to a change of 0.6 in G_M^s.

where the theoretical uncertainties have been combined into the last uncertainty in eq. (1.68). The SAMPLE extracted value for μ_s is in disagreement about the sign with most of the models quoted in Table 1.3, except maybe the solitonic models. The third SAMPLE measurement [49], at a $Q^2 = 0.038$ (GeV)^2, is in agreement with the theoretical estimate for the $G_A^{e(T=1)} = -0.91 \pm 0.28$ from [28], fig. (1-6). SAMPLE completed its physics program and while it found agreement with theory about the axial form factor extraction, the extracted nucleon strange magnetic moment has a different sign from most model calculations of this quantity.

1.5.2 HAPPEX

HAPPEX experiment completed a measurement of the parity-violating asymmetry in elastic electron scattering from liquid hydrogen in 1999. The experiment took data in experimental Hall A at Jefferson Lab. A schematic of the setup is shown in fig. (1-

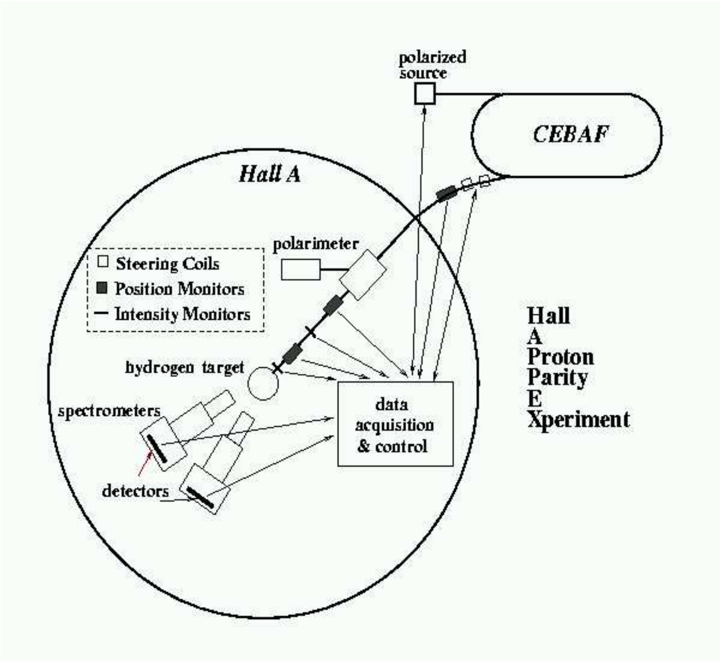

Figure 1-7: HAPPEX schematic in Hall A at Jefferson Lab.

7). The detection in HAPPEX is in forward angle mode, at a mean electron scattering angle of $<\theta_e>= 12.3^o$. The physics asymmetry at the average $Q^2 = 0.477$ (GeV)^2 was determined to be [50]

$$A_p = -14.92 \pm 0.98 \pm 0.56 \text{ ppm} \tag{1.69}$$

where the first uncertainty is due to statistic and the second one to systematic effects. From this value, eq. (1.69), a linear combination of the electric and magnetic strange form factors can be extracted, with the axial form factor determined from a corrected dipole form, eq. (1.55)

$$(G_E^s + 0.392 G_M^s)(Q^2 = 0.477) = 0.014 \pm 0.020 \pm 0.010 \tag{1.70}$$

where the first uncertainty is experimental and the second one is due to the electromagnetic form factors Q^2 dependence. As this result ties together the strange electric and

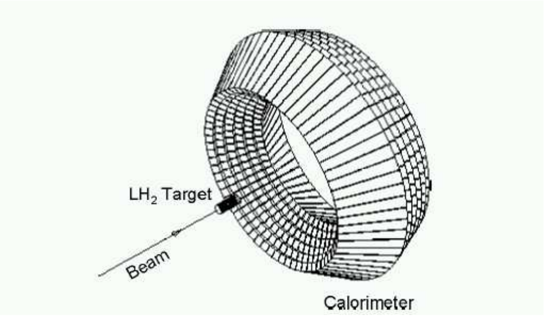

Figure 1-8: PVA4 detector.

magnetic nucleon form factors, it is difficult to draw conclusions about individual form factors based solely on it.

The HAPPEX collaboration plans to take data in 2004 in very forward angle mode, at a $Q^2 = 0.11$ (GeV)^2, on both hydrogen and ^{4}He targets. The data that will be taken on hydrogen will complement both SAMPLE and the lowest Q^2 point in the G^0 experiments. The data on ^{4}He is sensitive only to G_E^s and will help separate the strange form factors at this Q^2 point.

1.5.3 PVA4

PVA4 experiment completed a measurement of the asymmetry in forward angle mode at the Mainzer Mikrotron (MAMI). A schematic of the apparatus is shown in fig. (1-8). Using a detection technique based on counting individual scattering events, the physics asymmetry measured at an average $Q^2 = 0.23$ (GeV)^2 is [51]

$$A_p = -5.44 \pm 0.54 \pm 0.26 \text{ ppm} \tag{1.71}$$

where the first uncertainty is statistical and the second one is given by the experimental systematic effects. Similar to the HAPPEX result, a linear combination of vector strange electric and magnetic form factors can be extracted

$$(G_E^s + 0.225 G_M^s)(Q^2 = 0.230) = 0.039 \pm 0.034 \tag{1.72}$$

The PVA4 collaboration took data at a $Q^2 = 0.11$ (GeV)^2 and analysis is underway. There are also firm plans for taking data in forward angle mode on deuterium targets at both Q^2 values of 0.23 and 0.11 (GeV)^2. In principle it is possible to turn the PVA4 apparatus, fig. (1-8), in backward angle mode, but there are no firm plans for this at present.

Table 1.4 shows a summary of experimental conditions for the SAMPLE, HAPPEX and PVA4 experiments.

Table 1.4: Experimental conditions for SAMPLE, HAPPEX and PVA4 setups.

	SAMPLE			HAPPEX		PVA4		
	I	II	III	I	II	I	II	III
Complete	√	√	√	√	No	√	√	No
Q^2 (GeV)^2	0.091	0.091	0.038	0.477	0.11	0.23	0.11	0.23, 0.11
E (GeV)	0.2	0.2	0.125	3.3		0.855	0.57	0.855, 0.57
I (μA)	40	40	40	100, 35		20		
Pol.	0.36	0.38	0.38	0.38, 0.7		0.8		
θ_e (deg)	147	147	147	12.3	6	30-40		
Target	H_2	D_2	D_2	H_2	H_2, ^4He	H_2	H_2	D_2

SAMPLE experiment is the only experiment to date which made an experimental separation of the form factors measured. With the future measurements in HAPPEX and PVA4 it will be possible to also separate the strange electric and magnetic, and the axial form factors of the nucleon at a Q^2 of about 0.1 (GeV)^2. The next section will describe how the G^0 physics program stands in the context of these experiments and the unique characteristics of this experiment of being able to completely separate the three form factors in a range of 4-momentum transfer 0.1−1 (GeV)^2, if the physics program is completed.

1.6 The G^0 physics program

The goal of the physics program in this experiment is to determine the Q^2 dependence of the vector strange electric and magnetic form factors of the nucleon and of the axial form factor. To accomplish this program three different measurements are needed to obtain three independent linear combinations of the form factors similar to eq. (1.52). As essentially free proton targets are available (liquid hydrogen is one possibility) the parity-violating asymmetry in elastic *ep* scattering, given by eq. (1.52), can be measured in two different kinematic settings, obtaining two linear combinations. In section 1.3.2 it was pointed out that through the interplay of kinematics A_p is selectively sensitive to the form factors of interest. At the same Q^2 a forward angle mode and a backward angle mode measurements can be performed. Assuming isospin symmetry, the parity-violating asymmetry on the neutron is obtained by changing the proton label, p, in eq. (1.52) with the neutron label n. Although there are no free neutron targets, to get a third measurement a nuclear target can be used. The parity-violating asymmetry on a nuclear target is given in the static approximation (non-interacting nucleons) by

$$A_{nucl} = A_0 \frac{N\mathcal{N}_n + Z\mathcal{N}_p}{N\mathcal{D}_n + Z\mathcal{D}_p} \tag{1.73}$$

where N, Z are the number of neutrons and protons in the target and $\mathcal{N}_p, \mathcal{D}_p, \mathcal{N}_n, \mathcal{D}_n$ are the quantities defined in eq. (1.46) for proton and neutron respectively. The nuclear target of choice in this experiment is liquid deuterium. The measurement on deuterium will be made in backward angle mode.

The G0 apparatus was designed in such a way that in the forward angle mode in a single run the parity-violating proton asymmetry can be measured over a range of Q^2

from 0.1 to 1 $(GeV)^2$. The details of this will be described in the next chapter. For the backward angle measurements a single value of Q^2 is sampled in a single run for both targets. In this way in the backward angle mode three values of Q^2 will be sampled, 0.3, 0.5 and 0.8 $(GeV)^2$ in a total of six runs (three on hydrogen and three on deuterium).

The matrical eq. (1.74) summarizes the three linear combinations of nucleon form factors as given by eq. (1.52) for forward, F, and backward, B, angle modes on hydrogen, and eq. (1.73) for backward angle mode on deuterium for a Q^2 point

$$\begin{pmatrix} A_F \\ A_B \\ A_d \end{pmatrix} = \begin{pmatrix} \xi_F & \chi_F & \psi_f \\ \xi_B & \chi_B & \psi_B \\ \xi_d & \chi_d & \psi \end{pmatrix} \begin{pmatrix} G_E^s \\ G_M^s \\ G_A^e \end{pmatrix} + \begin{pmatrix} A_F^0 \\ A_B^0 \\ A_d^0 \end{pmatrix} \tag{1.74}$$

where A_F, A_B, A_d represent measured asymmetries on the respective angle mode and target, the 3x3 matrix with coefficients ξ, χ, ψ represent the individual form factor weights, and A^0's are the free terms in the linear combinations. An example of eq. (1.74) is given in Table 1.5 for a $Q^2 = 0.44(GeV)^2$ in the middle of the range of 4-momentum transfer considered for this experiment. The interplay of kinematics can be seen in Table 1.5. In the proton forward angle run the coefficient for the axial term is negligible compared with the coefficients of the electric and magnetic terms, but becomes sizable in the backangle mode. The magnetic term contributes in both scattering modes, and the electric term

Table 1.5: Example of eq. (1.74) coefficients at $Q^2 = 0.44(GeV)^2$.

	A^0	ξ	χ	ψ
A_F	-13.79	51.77	18.61	1.01
A_B	-25.01	16.10	31.41	6.96
A_d	-34.00	13.13	7.07	8.41

has a sizable contribution in the backangle mode, as the scattered electron angle is 110° (the electric term goes to zero when $\theta_e \to 180°$).

The measurement analyzed here was done with the G^0 apparatus in forward angle mode on a liquid hydrogen target. The results will be presented as linear combinations of electric and magnetic strange-quark form factors.

Table 1.6 summarizes some parameters for the G^0 experiment physics program.

Table 1.6: Experimental conditions in G^0. Electron beam energy is E, electron beam current is I, scattering angles are θ_e for electron and θ_p for proton (detected particle is in boldface).

Parameter	Forward	Backward		
Q^2 $(\text{GeV})^2$	0.1 – 1	0.3	0.5	0.8
E (GeV)	3	0.424	0.585	0.799
I (μA)	40	40	40	40
θ_e (deg)	7 – 20	**110**	**110**	**110**
θ_p (deg)	**76 – 52**	26	23	21

Fig. (1-9) shows the projected uncertainties for the separated electric and magnetic strange vector form factors of the nucleon at the completion of the G^0 physics program. On the G_M^s plot there are also displayed the SAMPLE point, the filled square, eq. (1.68), the projected uncertainty for the HAPPEX II point, the triangle, (see Table 1.4), two LQCD calculations in the quenched approximation, Dong et al. from [34], four green stars on color plots, and Lewis et al from [35], one blue star on color plots. On the G_E^s plot there are also displayed the projected HAPPEX II point, and the LQCD calculations of Dong et al. from [34]. On both plots the dash-dotted line represents the χPT calculation of the slope at the origin for the two form factors, which is related to the rms strange electric and magnetic radii, by Hemmert et al. from [33].

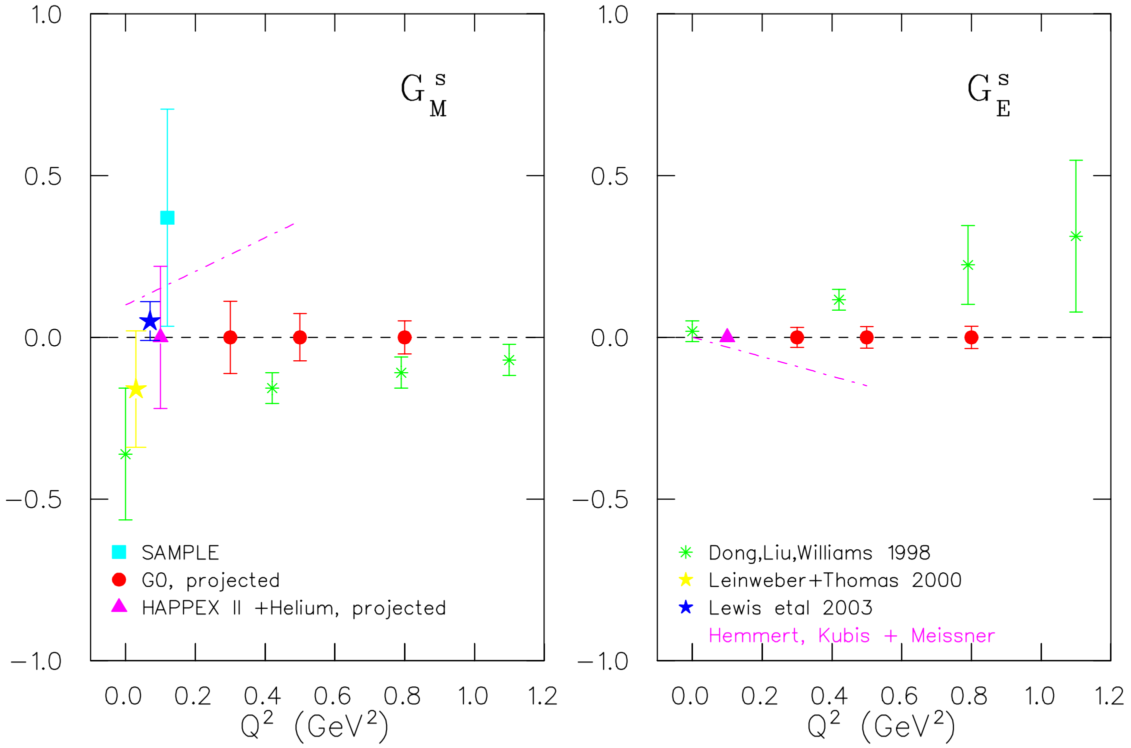

Figure 1-9: G_E^s and G_M^s projected uncertainties for the G^0 experiment, along with some theoretical calculations from LQCD and projected uncertainties for HAPPEX II.

Chapter 2

The G^0 Apparatus and Beam

2.1 Overview

The G^0 experiment is running in Hall C at Jefferson Lab in Newport News, VA. The G^0 physics program, described in section 1.6, calls for two running modes, forward angle and backward angle. The major subsystems of the apparatus are: the superconducting magnet system (SMS), the target system and the detection system (detector and electronics package). The G^0 apparatus was installed in Hall C in the summer and fall of 2002. Upon installation in Hall C the experiment had a first engineering run in fall-winter of 2002-2003, and a second engineering run in winter of 2003-2004, both in the forward angle mode. The physics run in the forward angle mode acquired data in the spring on 2004.

In the forward angle mode a 40 μA longitudinally polarized electron beam of 3 GeV energy hits a 20 cm long liquid hydrogen target. Elastically recoiled protons are focused from the whole length of the target by the SMS into a Q^2 segmented focal plane detector (FPD) in the Q^2 range from 0.1 to 1 $(GeV)^2$. The magnet and detector have azimuthal symmetry about the beam axis. The detection system uses a time of flight

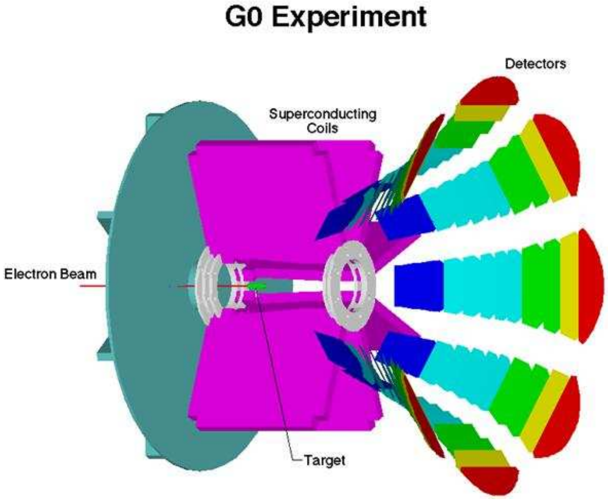

Figure 2-1: The G^0 apparatus. The superconducting magnet is shown with two of the eight coils removed for clarity.

(ToF) technique to separate elastic events from background. The apparatus used in the forward angle mode will be described in this chapter along with the G^0 beam and data acquisition.

2.2 The magnet system

The SMS is made of eight coils [52] in an azimuthally symmetric distribution about the beam axis to form a toroidal winding. Fig. (2-1) shows a drawing of the G^0 apparatus used in the forward angle mode. Two of the superconducting coils and two detector octants are removed from the drawing for clarity. The magnet system shares the vacuum with the cryogenic target system. The total volume under vacuum in the SMS and target systems is about 19.3 m^3. This volume is defined by two gate valves that separate it from beam line vacuum, one gate situated upstream and one gate situated downstream on the beam line. The SMS housing has a mean diameter of about 4 m and an axial length of 2 m. The beamline in Hall C sits 4 m above the hall floor and the SMS cold axis is centered on it.

The running point for the magnet in the forward angle mode is at a coil temperature of 4.5 K and a current of 5000 A. At this current the magnetic field integral is $\int Bdl = 1.6$ T·m and the magnetic field at the target location is null. The angular deflection in the magnetic field ranges from $35^o - 87^0$ and the azimuthal acceptance is about $0.44{\cdot}2\pi$. The coils are wound with Rutherford cable (20 strand, Nb-Ti alloy). There are 144 cable turns displaced in 4 layers in a coil. The coil cable becomes superconducting at about 8 K. A single wire in the strand has a diameter of 0.65 mm and can carry 450 A current when superconductive. The inductance of a coil is 0.33 H. The energy stored in the magnet when energized at nominal current is 4.3 MJ. The SMS is kept cold by a combination of coolant liquid helium and liquid nitrogen. The liquid helium is delivered by the end station refrigerator (ESR) at Jefferson Lab from the 4 K nominal supply. The acceptance for particles is defined through a combination of Al and Pb collimators displaced in the space between the coils that can be viewed in fig. (2-11). The collimators block direct view from the target to the FPDs, shielding against neutrals. Controls and monitoring of the SMS is assured though a programmable logic controller (PLC) that runs on a dedicated computer under the Windows operating system. Thermal cycling (300 K - 4 K - 300 K or 4 K - 300 K - 4 K) of the SMS takes about 6 weeks. On the SMS vessel there are 8 thin (0.5 mm or 20 mils) Ti windows that the particles go through on their way to the FPDs.

The SMS has been successfully commissioned at 5000 A in late December of 2002. The SMS consumes about 4-6 g/s liquid helium to stay superconductive at the nominal current. The data analyzed here has been taken at the nominal current in the SMS. The same magnet system will be used for the backward angle runs.

2.3 The target system

The major components of the target system are: the cryogenic loop, the service system and the controls.

2.3.1 Cryogenic loop

The cryogenic loop is shown in fig. (2-2). The loop can be divided into several units: the cryogenic pump housing, the heat exchanger housing, the target manifold and the bellows. The target manifold is the only unit made of Al. The shell of the rest of the loop is made of stainless steel 304.

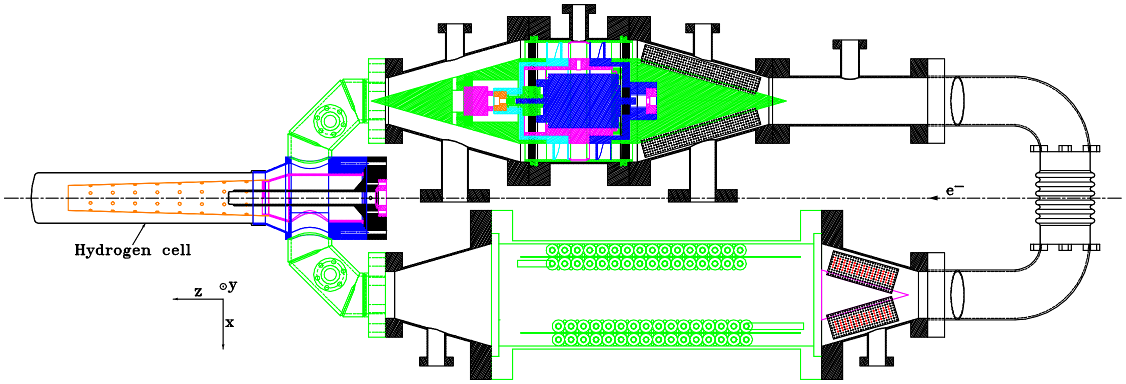

Figure 2-2: The cryogenic loop. The ports along the loop are not in the mounted position.

During normal running the loop is placed horizontally inside the superconducting magnet, in the same plane as the beam line. The orientation of the loop with respect to the direction of the beam line is with the target cell placed downstream. To ensure safe beam operation on target, the upstream part of the loop goes below the horizontal plane and contains a bellows that connects the two sides of the loop below the beam plane (see fig. (2-6)). Except for the upstream bellows all loop parts are rigidly interconnected. The bellows reduces the mechanical stress due to the rigid connections along the loop. Once the loop is put together, the bellows is clamped in place and the whole cryogenic loop becomes a rigid structure.

The target manifold

The target manifold (see fig. (2-3)) is completely made of Al-6061 T6 and connects with the loop through transition stainless-Al conflat flanges. All loop units are connected through conflat flanges with Cu gaskets, rated for high vacuum (10^{-11} Torr) well beyond what's needed in the experiment (the vacuum nominally sits around 10^{-6} Torr during normal running).

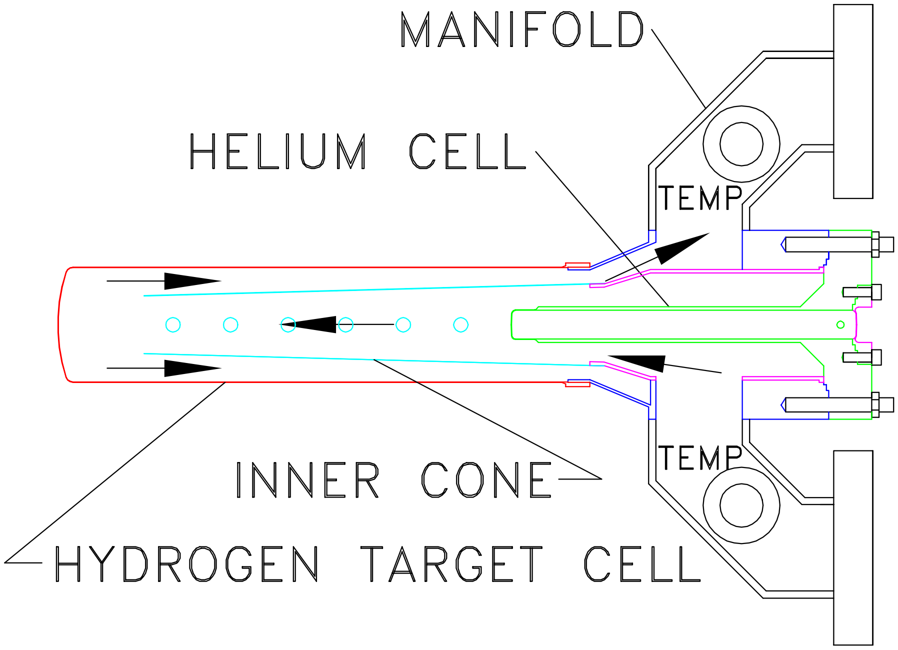

Figure 2-3: The target manifold.

The target manifold houses two cells, a primary hydrogen cell and a secondary helium cell. The primary cell is a thin shell cylinder, about 23 cm long, soldered on an Al joint on the downstream of the manifold. The cell used for the first engineering run was Al-6061 T6 with an outer shell thickness of 0.007" and an exit window of 0.011". The diameter of the cell is 5 cm. Although it performed flawlessly this cell has been replaced for the second engineering run with an almost identical cell except for the exit window. The new cell has a uniform thickness of 0.007" all over and a thinned down nipple on the exit window, centered on the cell's axis, with a diameter of 8 mm and thickness of 0.003″. The thinner exit window reduced the inelastic photoproduction background contamination under the elastic peak, and improved on the signal to background ratio in the elastic region. This new cell has been used for the second engineering run and for the forward angle production run with about 40 % background reduction. The helium cell is 16 cm long and is placed upstream of the primary hydrogen cell. The helium cell is a cylindrical tube machined in one piece on a flange that connects to the manifold through an indium seal. The inner diameter of the helium cell is 0.5″ and defines the clearance volume for beam. The tube of the helium cell has a nipple soldered at the downstream end. The nipple is machined in one piece and has a thin window of 0.009″ thickness. At the upstream end, the helium cell is protected against vacuum by an Al thin window, 0.007″ thick, machined on an Al flange that connects to the helium cell flange through an indium seal. The helium cell is operated at the same pressure as the hydrogen cell. There are three thin Al windows in beam. The distance between the exit window of the helium cell and the exit window of the hydrogen cell is 20 cm and defines the liquid hydrogen target in beam. Nominal running conditions with liquid hydrogen are 1.7 atm and 19 K. Since, at a pressure of 1.7 atm, hydrogen liquefies at 22.21 K, the nominal running point is a 3 K subcooled liquid. In these conditions the target thickness in beam is 1.44 g/cm^2, yielding luminosities in excess of $2{\cdot}10^{38}$ cm^{-2}s^{-1}, and the target is a 2% radiator.

There are two particular reasons for having the helium cell. The exit window of the helium cell has the same shape and radius of curvature as the exit window of the hydrogen cell. The thin exit window of the hydrogen cell has a spherically convex shape with a radius of curvature of 7.6 cm. Hence, systematic effects caused by parallel beam drifts on target are reduced to first order. Another feature of the helium cell design is that it provides azimuthal symmetry for scattered particles, originating in the hydrogen target, in the range of the angular acceptance of the SMS.

The hydrogen cell has been machined in one piece from Al-6061 T6. There are several spare hydrogen cells available made of Al-6061 and Al-7075.

The heat exchanger

One of the cryogenic loop's legs houses a double coil counterflow high power heat exchanger. The coils are made of finned Cu tubing on the hydrogen side to increase the area for heat exchange. The coolant agent used is cold helium gas from the End Station Refrigerator (ESR) 15 K / 12 atm supply at Jefferson Lab. The inner space of the heat exchanger's coils is filled with an Al flow diverter (not shown in fig. (2-2)) that forces the loop's fluid to go through the fins. The heat exchanger unit also houses a single coil low power heater (LPH) at the upstream end. The low power heater has an electrical resistance of about 21.1 Ω. The area for heat exchange on the hydrogen side is 9500.73 cm^2, and on the coolant helium side is 1110 cm^2. The effective diameter for flow in the hydrogen circuit is 30.4 cm^2 and 0.338 cm^2 on the coolant helium side.

Cryogenic pump

The other leg of the cryogenic loop houses the cryogenic pump and the high power heater (HPH). The pump is a vane-axial design with two impellers in series. The impellers have three blades each and are rigidly attached on a motor shaft that is immersed into the cryogenic fluid. The volume dislodged by the pump in one revolution, corrected for the volume of the blades, is 0.198 l. The cryogenic motor that is presently in use is a Barber-Nichols Inc. custom made DC brushless sensorless motor, driven by a sensorless controller. The motor is rated for liquid hydrogen and has a $0.5''$ diameter shaft. Downstream from the pump there is a conical Al-made flow diverter inside which there is a tachometer. The tachometer is completely separate from the pump system. It is made of a Cu coil rigidly attached to the Al flow diverter. The downstream pump impeller has a permanent small field magnet dipole rigidly attached to it. When the impeller rotates the varying magnetic flux through the coil, caused by the magnet, induces a varying electric field with the same frequency as the rotational frequency of the impeller and offers a measure of the motor's rotation that is independent of the motor's controller. The tachometer signal is read back by a digital multimeter enabled in frequency mode (Agilent model 34401A).

Upstream of the pump there is a second conical flow diverter made of Al that houses the HPH. The purpose of the HPH is to regulate the heat load on the target in a feedback loop during normal operations. The HPH is made of three independent coils wrapped on a G10 form, connected in parallel at the back of the power supply. In this configuration, in case one of the coils becomes inoperable, it doesn't incapacitate the whole heater. A reconfiguration of the remaining coils at the back of the power supply will enable its continual operation. The coils are made of Ni-Cr alloy ribbon and each has a resistance of about 3.5 Ω, giving a total resistance of 1.15 Ω. The HPH power supply, PowerTen 3300P/4025, is operated remotely with two low-voltage dc control signals (0-10 V = 0-100 %) that are set by analog output channels from a VME board.

Flow diverters and miscellanea

There are flow diverters inside the cryogenic loop, all made of Al-6061. The purpose of the flow diverters is to guide the fluid smoothly around the loop and assure high Reynolds numbers in the target cell and heat exchanger, where turbulence facilitates heat transfer or heat removal and mixing. Besides the flow diverters along the loop, already mentioned, inside the target cell there is a conical tube, made of Al-1100, of 0.00762 cm (0.003″) thickness (see fig. (2-3)). The tube acts as a flow diverter and guides the liquid down the center of the target cell serving two purposes. The conical geometry increases the flow speed as it traverses the cell parallel to the beam direction, increasing the turbulence and mixing of the fluid. The conical tube has holes on the side that run along the surface. The holes allow the fluid to leave the interaction region before reaching the end of the cell, helping in removing heated fluid from the beam path sooner and reducing the intrinsic interaction time between the beam and the fluid. The holes also serve a mechanical purpose, they prevent the conical tube tearing by relieving the static pressure on the inside of the conical tube. The holes sit in the shadows of the superconducting magnet coils, thus do not influence the scattered particles within the experimental acceptance. When the hydrogen cell was changed between the two engineering runs a visual inspection of the flow diverter used during the first engineering run found no traces of tearing or mechanical deformations.

For the first engineering run the target had implemented an Al frame with dummy targets that were used for background, detector and beam studies. A picture of the dummy targets frame is given in fig. (2-4). On a horizontal frame mounted across the target cell manifold upstream of the target cell and sitting at the edge of the SMS

Figure 2-4: The dummy-targets Al frame.

acceptance were three targets: two halo and one ^{12}C targets. The halo targets were meant for beam quality studies. They were straight through holes in the Al frame of 5.46 mm and and 11.05 mm diameter (known as the small and the big halo targets respectively). The big halo target has a Cu collar mounted on the Al frame with the same inner diameter and matched the radiation length of the Al flange that supports the vacuum window on the target upstream helium cell. The halo targets were beam quality diagnostics tools. Two diameter holes were implemented to differentiate between beam halo at about the helium cell inner diameter (12.5 mm), the big halo target, and at about half of that diameter, the small halo target. The ^{12}C target was a solid target of 4.9 mm thickness that matched the liquid hydrogen target radiation thickness. This target was used extensively in the commissioning of the FPDs.

For the second engineering run the ^{12}C target has been taken out and the remaining hole used for passage of a photon flux produced by the electron beam on a newly implemented W target. The W target matches the radiation thickness of the liquid hydrogen target but sits completely outside the detector acceptance, being mounted on an ear off the upstream flange of the cryogenic pump housing. The W target was used in conjunction with a so-called flyswatter target. The flyswatter is an Al foil target mounted on a handle to downstream of the liquid hydrogen target. The flyswatter target can be put in beam or out of beam independently from the liquid hydrogen target. These newly implemented targets were used for studies of the background produced by the Al windows in the hydrogen target.

Except for the cryogenic motor rotor all materials used in the fabrication and assembly of the target cryogenic loop are either low magnetic susceptibility or non-magnetic materials. The rotor of the cryogenic motor is made of strong permanent rare-earth magnets with fields at the surface in excess of 1 kGauss, which decay quickly with radial distance. The rotor sits about 10 cm off the central beam axis in the horizontal plane. The center of the motor sits about 46 cm from the center of the target cell. Measurements of motor's magnetic field done with Hall probes found that: the magnetic field half way between the bearings and 5 cm from the rotor's axis of revolution is less than 7 Gauss. At 7.5 cm the field is less than 1 Gauss and at 10 cm is undetectable. The field along the rotor's axis of revolution is 1.5 Gauss at one bearing and less than 1 Gauss at the other bearing. At both ends of the rotor the field is undetectable at a distance of more than 2.5 cm away from the bearing. The magnetic field integral along a particle's trajectory changes the nominal field integral of the SMS by about 0.01 ppm, a negligible change, since the magnetic field is required to be known to better than 0.2 % in order to extract the Q^2 at the level of 1 %. In conclusion this type of motor does not pose any problems for the systematics of the experiment in terms of magnetic field distortions at a level well below 1 ppm and does not pose any distorting influence on the electron beam as it passes by on its way to the target cell. The coils of the HPH can act as an electromagnet when the heater is powered by the dc signal from its power supply. The maximum field achieved when the heater is operated at maximum power is about 1 Gauss on the heater's axis, thus posing no problems for experiment.

Instrumentation

Along the cryogenic loop there are eight electrical feedthroughs with mini-conflat flanges used for instrumenting six temperature sensors directly into the fluid, the tachometer, the heaters and the cryogenic motor. All wiring used in instrumenting the electrical signals are Kapton insulated Cu leads. All feedthrough connectors have been covered with heat-shrink tubing to prevent possible discharges or electrical shorts among connectors in a feedthrough. The connectors are push-pin; no feedthrough connections were made permanent. The six temperature sensors used on the loop are LakeShore Cernox CX-1070-AA. The sensing element is incased in a gold-plated copper case 3 mm in diameter and 8.5 mm long. The temperature range for these sensors is from 4.2 K up to 325

K, more than sufficient to monitor target temperatures from room temperature down to the lowest temperature in the system (the temperature of the helium coolant supply of 15 K). The absolute precision of these sensors is 0.025 K. An additional set of three temperature sensors of the same kind were instrumented in the helium coolant lines. One sensor was placed just before the Joule-Thompson valve and two right across the heat exchanger to monitor the coolant temperature to and from the target. The temperature sensors are read by Oxford ITC-502 temperature controllers, which can accommodate as many as three sensors in one controller. The precision of the readout is four digits total. Five sensors in the loop and the three on the coolant lines are read with 0.01 K precision (restricting the temperature range for these ones from 4.2 K to 99.99 K), and one sensor on the loop is read with 0.1 K precision (having a full temperature range, 4.2 K to 325 K). The lower precision sensor is used to monitor target warm-ups and cool-downs from room temperature to below 20 K. Five sensors on the loop sit below the horizontal plane and one sensor sits above the plane. The one above the plane is used in assessing the level of the cryogenic liquid in the loop. The temperature sensors are distributed along the loop in pairs, two across the pump and HPH, two across the target manifold and two across the heat exchanger. The HPH and the pump have their own electrical feedthroughs, the tachometer and the LPH share feedthroughs with the temperature sensor located closest to their location. The electrical lines from the loop go through a second set of feedthroughs on the service module to the G^0 electronics racks in the hall. The cables are about $140'$ long and made of Kapton insulated Cu. As an extra precaution the wires under vacuum have been shielded with 4-channels ceramic beads. The beads are radiation and fire resistant.

2.3.2 The service system

The service system for the target is split in two major components, the mechanical service module, that supports and moves the target, and the gas handling system.

The gas handling system

The gas handling part of the target system incorporates gas service lines, a gas panel and a ballast tank. Fig. (2-5) shows a schematic of the gas handling system (the dashed line is the gas panel boundary). The external coolant supply lines are vacuum insulated U-tubes. The coolant comes from the 15 K / 12 atm cold helium supply at the ESR. The flow needed to extract heat loads of up to 500 W on the target is less than 14 g/s. The coolant is transferred from the U-tubes to uninsulated lines that sit inside the target service module (under vacuum) through meter-long bayonets. The coolant flow to the target's heat exchanger is controlled by a Joule-Thompson (JT) valve. The JT valve is the only active control on the coolant flow. It is not controlled by any feedback system, but only by manual control. The gas panel sits in experimental Hall C and its primary purpose is to supply the cryogenic loop with gases. It has a wide functionality. It supplies both cells in the cryogenic loop with gases from dual supplies (the hydrogen cell can be supplied with gas from a bottle in the hall or from a ballast tank outside the hall; the helium cell can be supplied with helium from bottles in the hall or from a 4 atm source of high purity helium). In addition to supplying gases to the two cells in the cryogenic loop, the gas panel connects the hydrogen cell to adequate relief paths for excessive pressure, either to the ballast tank or to the hall's standard dry nitrogen vent. The panel's functions are possible through a combination of manual, pneumatic, solenoid, check and relief valves. All manual valves on the panel are instrumented with 2 LEDs and 2 micro-switches. One LED is red (for valve fully closed state), and the other one is green (for valve fully open state), which when lighted indicate the state of the valve (the state is

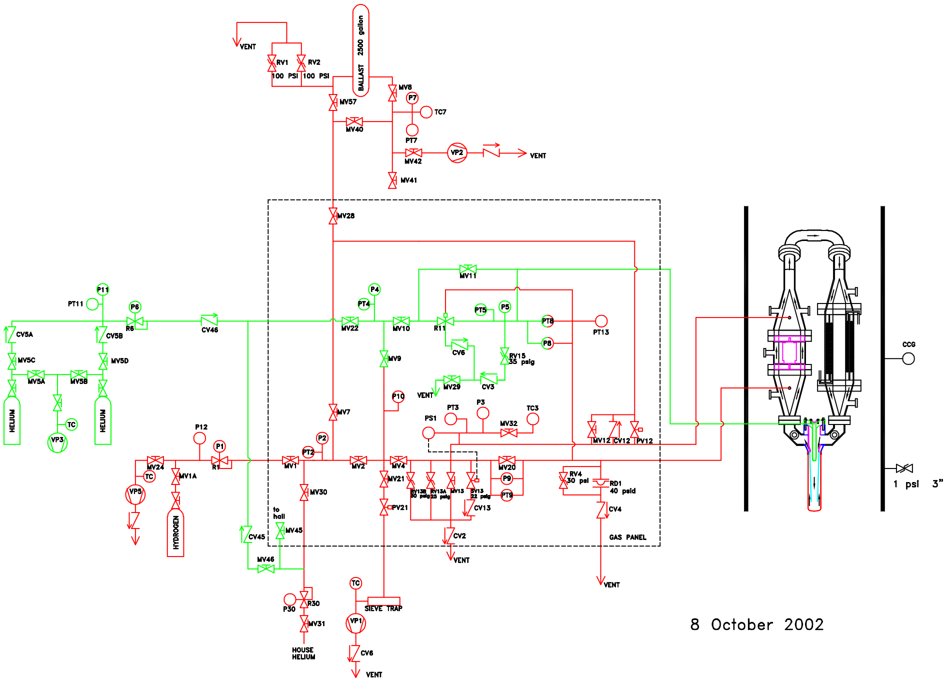

8 October 2002

Figure 2-5: The gas handling system.

also read back on the target control computer through micro-switches). On the gas panel there are 2 pneumatic valves controlled by a vacuum interlock box. The interlock box prevents the operation of these valves unless there is sufficient vacuum in the magnet's vessel. One pneumatic valve connects the gas panel with a pumping station, the other one connects the gas panel with the ballast tank during normal running. The interlock box prevents pumping on the cryogenic loop unless adequate vacuum is established in the magnet's vessel, hence protecting the thin hydrogen cell against implosion. In case of a vacuum breach in the magnet vessel, the interlock box also closes the connection between the ballast tank and the cryogenic loop, reducing the inventory of hydrogen (deuterium) that might come in contact with air. There is one solenoid valve on the gas panel whose function is to control the venting of the target system to the dry nitrogen vent line. It is controlled by a pressure switch which opens the valve at 22 psig and closes it at 26 psig. The pressure switch has mechanical set points and cannot be controlled remotely. There are three paths in parallel with the solenoid valve: two instrumented with relief valves that open at 25 and 30 psig, respectively, and one with a rupture disk that breaks at 41.1 psig.

A special regulator, R11 in fig. (2-5), controls the pressure across the thin exit window of the helium cell. The regulator operates on a master-slave principle, it uses the pressure from the hydrogen circuit to regulate a higher supply pressure of helium to keep the pressures in the two cells in balance. The nominal running pressure in the hydrogen circuit is 10 psig, and R11 regulates a helium supply from 37 psig down to the pressure in the hydrogen circuit.

The gas panel is also instrumented with pressure gauges for direct reading of pressures in the system and with pressure transducers for remote monitoring of pressures. The transducers, made by Omega, are of three varieties, one absolute with range from 0 to 100 psi, another one absolute with a range from 0 to 3000 psi, and one differential with a range from -15 to 15 psid. The differential transducers are used to read the pressure across the exit window of the helium cell and the pump head.

All the components on the gas panel are either explosion proof or rated for hydrogen. The JT valve can be operated either from a computer or manually from its control box. The JT valve control box was located in an electronics rack inside Hall C during the experiment's running. To prevent accidental remote operation all the other components of the gas handling system can only be monitored.

In the normal mode of operation, before a run starts, the cryogenic loop and the helium cell are pumped and purged several times (following [57]) with helium before the running fluids are made available to the target. Before cool-down starts, the cryogenic loop is put in connection with the ballast tank and will stay connected to it at all times during a run, unless a vacuum incident triggers the vacuum interlock box to close the connection. The ballast tank acts as a big pressure reservoir and mitigates pressure excursions in the target during normal running. The ballast tank is also a storage reservoir for target fluid (hydrogen or deuterium), it has a volume of 2500 gallons. As a safety precaution, some critical valves in the gas delivery system for the target are locked and only target experts have access to them.

The service module

The target's service module (SM) has been manufactured by Thermionics NW. The basic functions of the SM are to support the cryogenic loop, to provide motion control along two axes perpendicular to the beam axis and to provide an interface for gas lines and

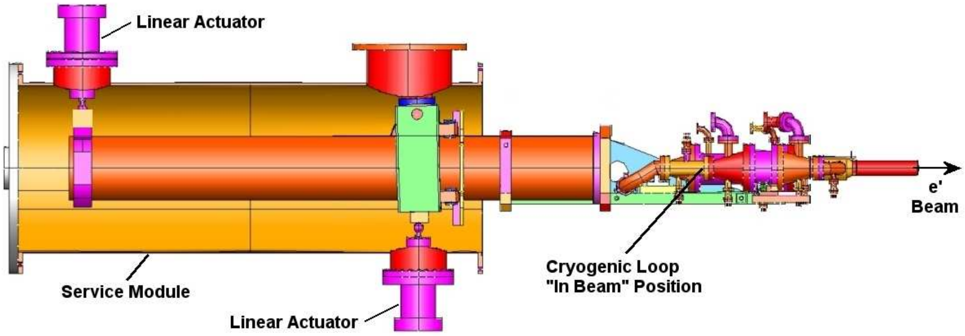

Figure 2-6: The service module. The target is shown in the $''in - beam''$ position.

electrical lines from vacuum to the outside world. A technical drawing of the SM can be viewed in fig. (2-6), along with the functionality of the associated motion system. The cryogenic loop is rigidly supported inside the SMS on a cantilevered platform from the SM. The cantilever is moved by four linear actuators through ball joints. The actuators are placed in pairs in two vertical planes at different locations along the beam axis. With these degrees of freedom the target can be placed in position, aligned to the magnet-beam axis to better than 1 mm in both x and y directions (the nominal reference system has the z axis along the beam line with positive sense down the line, the y axis is vertical with positive sense up, and the x axis is horizontal in-plane with positive sense to beam right). The actual location precision of the motion system along a single axis is 0.05 mm, and for two axes combined it should position the target to better than 0.1 mm.

The SM is located on the beamline upstream of the SMS. It interfaces with the SMS through a $2'$ diameter flange and with the beamline through a $6''$ gate valve. The SM cannot be separated from the SMS without breaking the vacuum, but it can be separated from the beamline with the gate valve. The target cell can be moved about $3''$ vertically and about $\pm\ 1''$ horizontally. In the vertical direction the target has an out of beam position with $1''$ clearance for beam. To protect the target from hitting the inner bore of the SMS, under any circumstances, the motion system is instrumented with limit switches arranged on a ring around the beam axis. Once a switch hits a wall the motion in that direction is blocked and only retraction is possible.

2.3.3 Target controls

The target controls system is a set of electronics, computers and software used to monitor, operate and control the target. The main functions of the controls system are: monitoring target parameters, sound an alarm in case warning or critical conditions have been met, log target data at regular intervals, provide selected target data to the online data acquisition system, control the target heaters to ensure target stability and move the target along two axes perpendicular to the beam axis (the target system has no degree of freedom along the beam line). The controls for this target have been described in detail in [56]. Most of the monitoring and controlling electronics sits in two electronics racks in the hall, shielded from direct radiation from the target. The signals are centralized in the hall into an Input-Output Controller (IOC) that is located in a VME crate in a rack in the hall. The VME processor is a mv2700 power PC. The analog input and output to the IOC is done through Greenspring ADIO modules. The IOC is also able to process data from serial ports. Information from the IOC is shipped through the local Ethernet to a monitoring computer located in the Hall C Counting House. This computer is the monitoring and control station for target parameters during normal running and is operated by a trained target operator. All the target monitoring and controlling electronics are on Uninterruptible Power Supplies (UPS) to ensure safe monitoring and controlling of the target system in case of a power failure. The target data are part of the larger EPICS database at Jefferson Lab. Operation (monitoring and controlling) of the target is done through a combination of software, Graphical User Interfaces (GUIs), and hardware. The cryogenic pump speed is controlled only through a linear potentiometer. There is no IOC or computer control on the pump speed in order to avoid perturbations on the pump's rotation due to IOC and/or computer crashes.

The HPH is primarily controlled through a Proportional-Integral-Differential (PID) feedback loop with a temperature sensor in the cryogenic loop. In our implementation of the PID loop the feedback tracks the beam loading into the target and subtracts the beam power from the total power on the target, setting the rest on the heater and keeping a temperature sensor constant. This helps stabilize the target faster and with smaller temperature excursions especially in beam trip situations. There is a software limit to the power load on the target as a safety measure implemented to protect both the target and the heater. A parallel complete manual control of the HPH is used for situations when the IOC feedback loop is nonoperational (due to network failures or IOC crashes). As mentioned before the gas panel is completely outside of computer control. All other target parameters, besides pump speed, gas panel and sometimes the HPH, are controlled through the IOC. All target parameters are monitored through the IOC on the target computer screen.

The target computer, operated by Linux, contains all the GUIs used in operating the target. The GUIs are a combination of MEDM (Motif Editor and Display Manager, developed by Argonne National Lab.) and StripTool charts (software developed by Jefferson Lab). Besides the HPH control, from the target computer the operator also has control of the JT valve, IOC reboot and target motion. During normal running the JT valve is operated remotely from the target control computer. The JT valve is the only control over coolant flow. There is no direct control over the delivered coolant temperature. In principle this is not a problem for hydrogen and helium as the coolant supply comes at 15 K and hydrogen freezes at 13.8 K (regardless of pressure). In case the IOC crashes the target operator has the possibility to reboot it either from the target computer or from a hardware switch. Target motion can be controlled either from the target computer or from the remote readback box for the linear actuators. The primary operation is from the target computer, which is completely automated. A number of positions for the target have been implemented in software through buttons.

In case of a power failure all target controls should remain up and running for at least 30 min, some for hours. This gives sufficient time to a target expert to park the target in a safe state until the power comes back, in case it is not just a glitch.

2.4 Target tests and performance

There are two principles at the base of our testing program, safety and performance. The target had been very throughly tested in order to be certified as safe, since it operates explosive gases (hydrogen and deuterium). The target design performance needed to be demonstrated before installing it in the experimental hall.

The preliminary target checks and tests included mechanical integrity tests (pressure tests, leak checks, etc.) and performance tests with cold helium gas in the cryogenic loop. Subsequently the target system has passed several safety reviews at Jefferson Lab, including a final one that gave a green light for physics for the whole G^0 apparatus.

2.4.1 Pre-beam tests

The purpose of the pre-beam tests were to assess the target overall dynamical performance, safe operation and reliability. These tests were split in three different sets: cold helium tests, liquid neon safety test and liquid hydrogen tests.

Cold helium performance

In the Test Lab the target was tested for the first time in cryogenic conditions by using helium coolant (4 K / 3 atm at maximum 5 g/s) delivered by the Cryogenic Test Facility (CTF) refrigerator and helium gas as target fluid in the cryogenic loop. The cold helium tests were meant primarily to assess the cryogenic pump performance and the operation of the target's instrumentation. During the period of these cold helium tests the target has been filled with the coldest cryogen to date, 7 K / 20 psig helium gas (about a quarter of the pump load expected with liquid hydrogen). The pump efficiency, eq. (2.2), and mass flow, eq. (2.1), can be determined by measuring the fluid temperature increase as it goes across a known heat source [55], which in this case is the HPH. In this approach helium is better than hydrogen as it yields larger temperature differences for the same heat load than hydrogen and the pump efficiency is measured with better precision. However, the cold helium is in gas state and is compressible as opposed to hydrogen which would be liquid and incompressible (see fig. (2-7)) for a comparison of the measured pump efficiency between helium and hydrogen). The heat exchanger was also tested for heat transfer performance. The coolant used in the Test Lab differs significantly from the one in the Hall (CTF delivers cold helium at 4 K / 3 atm, while the ESR delivers cold helium at 15 K / 12 atm). In these conditions the heat exchanger removed in excess of 500 W of heat loads from the target's fluid.

The cryogenic pump geometry has been designed to insure high speed fluid flow at a nominal rotational frequency of 30 Hz. Ample fluid flow is necessary in order to reduce target density related effects and mitigate systematic errors in the asymmetry measurements. To sustain the fluid flow needed it was determined, after a set of initial tests, that a high torque custom made motor was necessary for powering the cryogenic pump. The Barber & Nichols motor proved to have the desired performance and is the motor presently powering our cryogenic pump. Although it runs with no problems at 30 Hz in liquid hydrogen, it saturates in current at about 42.7 Hz and it may be just marginal for reaching 30 Hz in liquid deuterium.

The neon test

The target cells have been statically pressure tested to 85 psid. The estimate for maximum cell pressure in case of a liquid hydrogen catastrophic boil-off (the most serious scenario was considered to be the sudden loss of vacuum in the magnet vessel to room temperature air) was 29 psia with the designed venting lines. To test the design of the relief system for the cryogenic target a simulated loss of vacuum was performed using neon as target fluid and dry room temperature nitrogen as *"air"*. Neon has several qualities which make it suitable for such a test. It is inert, it has a liquefaction point close to hydrogen (28.98 K for neon and 22.21 K for hydrogen at 1.7 atm - the pressure for normal running conditions in the target), and is much denser than liquid hydrogen. The fact that the liquefaction points are close for the two fluids makes temperature differences from liquid state to room temperature to be similar for the two fluids, an important consideration when simulating loss of vacuum to room temperature air. Because liquid neon is 17 times denser than liquid hydrogen, the expected pressure peak in a vacuum loss was 38 psia, a 30 % increase compared with hydrogen. The length in time expected for the neon peak pressure to last is more than double the peak pressure time length expected for a catastrophic boiling of liquid hydrogen. For this test the target was mounted on the SMS and it successfully passed the safety neon test, *in situ*, on May 29, 2002. The cryogenic motor was able to push liquid neon in the cryogenic loop saturating in frequency at 12.2 Hz, the saturation in torque, eq. (2.3), was determined to be about 23 oz-in (the same torque limit reached with liquid hydrogen at 42.7 Hz).

Liquid hydrogen performance

For a week in early June 2002, the target underwent basically the same set of tests it did with cold helium, this time with liquid hydrogen.

As outlined in section 2.4.1, the pump flow can be determined by measuring the temperature difference of the fluid as it passes across a known heat source

$$\eta \cdot \dot{Q}_H = \dot{m}_{LH_2} \cdot c_P \cdot (T_{PO} - T_{PI}) \tag{2.1}$$

where $\dot{Q}_H$, in our case, is the power delivered by the high power heater power supply and $\eta \cdot \dot{Q}_H$ is the power deposited by the high power heater into the loop. The η factor accounts for the power loss in the electrical supply cables. The logged parameter was the power delivered by the power supply. To get the power deposited into the loop, the η factor was determined to be 0.75 (the distance between the power supply and HPH coils is about $140'$). Data have been taken at four different cryogenic pump rotational frequencies: 10, 20, 30 and 40 Hz, and at six different heater power values: 550, 450, 350, 250, 150 and 50 W for each frequency. The specific isobaric heat and density for liquid hydrogen were corrected for temperature dependence. Since the pressure stayed the same during these studies, there were no pressure related corrections to the input hydrogen parameters. At each power value the data included in the computation of the mass rate were the closest to the thermodynamic equilibrium. The pump efficiency can be estimated with the formula

$$\epsilon_P = \frac{\eta}{c_P(T) \cdot \rho(T) \cdot V_s \cdot f} \cdot \frac{\dot{Q}_H}{T_{PO} - T_{PI}} \tag{2.2}$$

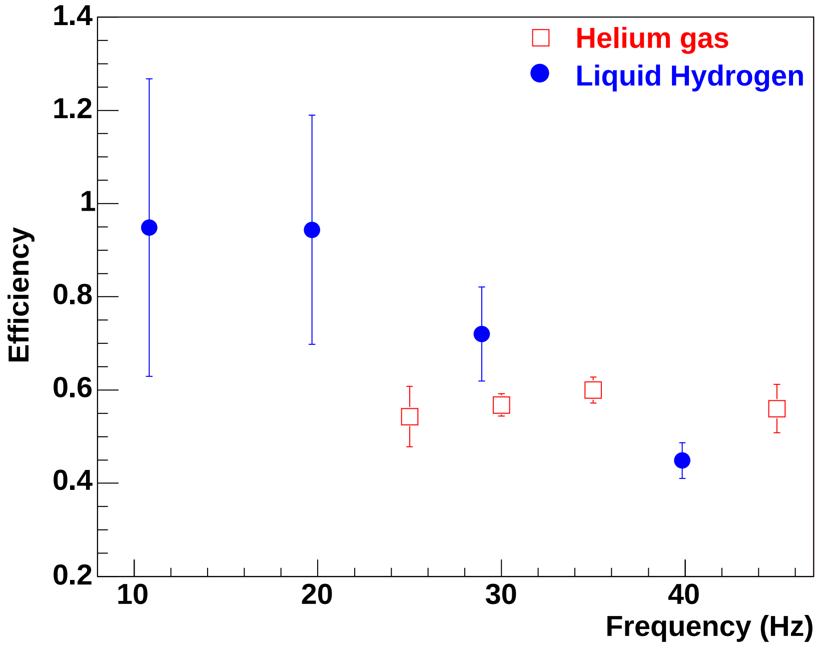

Figure 2-7: Cryogenic pump efficiency. Comparison between liquid hydrogen and cold helium gas.

where V_s is the theoretical volume displacement of the cryogenic pump in one revolution. The cryogenic pump has a vane-axial design with two identical impellers. Each impeller is equipped with three blades. The estimate for V_s, taking into account the volume of the blades, is 0.198 liters. The rotational frequency of the cryogenic motor shaft is denoted by f. The motor frequency was measured with the tachometer. The temperature was measured with the temperature sensors instrumented along the loop. The temperature across the HPH is denoted by $T_{PO} - T_{PI}$, where indexes mean pump-out and pump-in, respectively.

With the differential pressure across the cryogenic pump one can determine the torque of the cryogenic motor at different frequencies. The relation between torque and pressure is

$$\tau = \frac{V_s{\cdot}\Delta p}{2\pi} \tag{2.3}$$

The mechanical power delivered by the cryogenic pump can be determined from the data with

$$P = \epsilon_P \cdot V_s \cdot f \cdot \Delta p \tag{2.4}$$

The heat exchanger used in the G^0 target is a counterflow heat exchanger with finned tubing and was described in detail in sec. 2.3.1. For a counter flow heat exchanger, like the one in the G^0 target, the mean temperature difference [58] is given by

$$\Delta T_{LM} = \frac{T_{ho} - T_{ci} - (T_{hi} - T_{co})}{ln(\frac{T_{ho} - T_{ci}}{T_{hi} - T_{co}})} \tag{2.5}$$

and the heat exchanger coefficient is given by

$$U = \frac{\dot{q}_{He}}{\Delta T_{LM}} = \frac{\dot{m}_{He} \cdot c_p^{He} \cdot (T_{co} - T_{ci})}{\Delta T_{LM}} \tag{2.6}$$

where T_{hi} is the temperature of the liquid hydrogen going into the heat exchanger and T_{co} is the temperature of the helium coolant coming out of the heat exchanger, for example. During the heat exchanger studies the coolant mass flow as read from the ESR flow-meter for the 15 K supply for Hall C never exceeded $\dot{m}_{He}$ =10.5 g/s. As in the pump studies ΔT_{LM} was determined for four cryogenic pump frequencies and six setpoints for the high power heater.

To characterize the heat exchanger further its effectiveness has been determined, which for a counter flow heat exchanger is defined theoretically [58] as

$$\epsilon_{HX}^{th} = \frac{1 - e^{-N \cdot (1-R)}}{1 - R \cdot e^{-N \cdot (1-R)}} \tag{2.7}$$

where R is the heat capacity rate ratio, and N is the number of heat transfer units, defined as

$$R = \frac{(\dot{m} \cdot c_P)_{min}}{(\dot{m} \cdot c_P)_{max}}, \quad N = \frac{U}{(\dot{m} \cdot c_P)_{min}}$$

where min/max refer to the helium coolant or hydrogen liquid, $(\dot{m}{\cdot}c_P)_{min} = min(\dot{m}_H{\cdot}c_P^H$, $\dot{m}_{He}{\cdot}c_P^{He})$.

Physically it represents the ratio between the actual rate of heat transfer in the heat exchanger and the maximum allowable rate by the second law of thermodynamics. Experimentally the value of the effectiveness is given by

$$\epsilon_{HX}^{exp} = \frac{T_{co} - T_{ci}}{T_{hi} - T_{ci}} \tag{2.8}$$

Results and comments

The cryogenic pump efficiency, fig. (2-8a), and flow measurements, fig. (2-8c), in the loop have large uncertainties due to the small temperature differences in hydrogen that can be induced across the high power heater (on average about only four times bigger than the systematic calibration error of 25 mK). Data from the two lowest heater setpoints (50 and 150 W) have been excluded in averaging the pump efficiency and mass rate. With the present controller the cryogenic pump saturated at 42.7 Hz shaft frequency. The saturation is not achieved on a differentiable curve, which means that it is not caused by the motor torque reaching its highest physical limit, but by the controller reaching its current limit. At the saturation torque, of 23 oz·in, with the present controller, the cryogenic pump head was 1 psid, and the mechanical power delivered to the liquid was about 43 W. The manufacturer's rating from the motor torque is 50 oz·in at a nominal frequency of 30 Hz. It can be inferred from the data on the saturation frequency in liquid neon and liquid hydrogen that the saturation frequency is inversely proportional with the square root of the density of the fluid. Based on this inference the predicted saturation frequency in liquid deuterium is about 29 Hz at the nominal running point in this liquid. The power delivered by the pump is fitted well by a polynomial of third degree in frequency, fig. (2-8d). The pump head fig. (2-8b) is fitted well by a second degree polynomial in frequency, although the pump efficiency is frequency dependent in liquid hydrogen. The mass flow seems to be maximum at the nominal frequency of 30 Hz, with a pump efficiency of 0.7. The average flow speed in liquid hydrogen cell was determined to be about 8 m/s. The Reynolds number for the liquid hydrogen flow determined in these conditions is in excess of 10^6. Since the transition between laminar flow an turbulent flow happens for flows with Reynolds numbers between 2000 and 10000, the liquid hydrogen flow in our target at 30 Hz is well in the turbulence region.

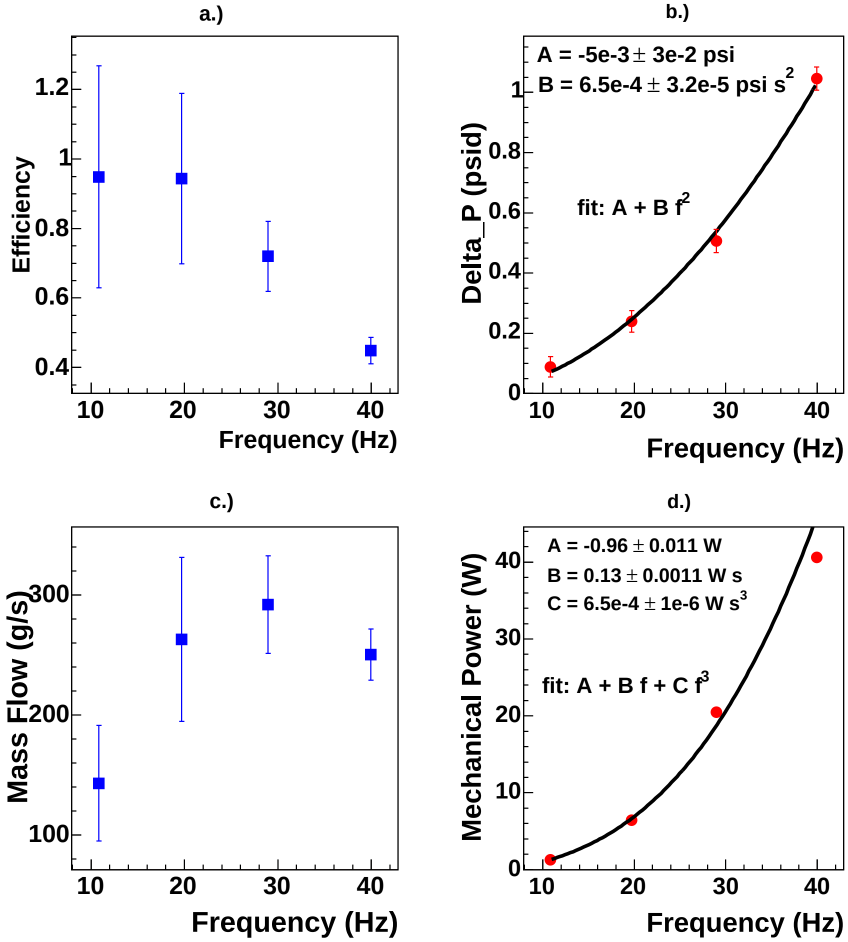

Figure 2-8: Cryogenic pump performance in liquid hydrogen.

The heat exchanger removed 450 W of heat from the loop with a coolant flow of 10.5 g/s from the 15 K helium coolant supply at the ESR. The flow of the coolant, as read

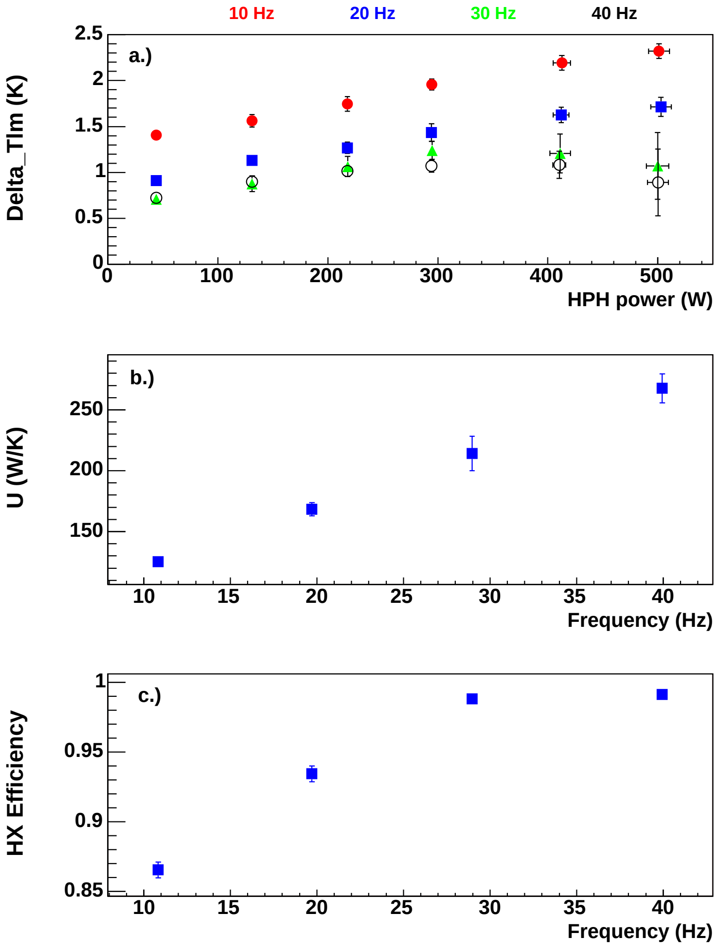

Figure 2-9: Heat exchanger performance in liquid hydrogen.

from the ESR cryogenic flow-meter, has 30% uncertainty.

The heat transfer coefficient, U was computed with the semi-empirical formula

$$\frac{1}{U} = \frac{1}{(h_{He} \cdot A_{He})} + \frac{1}{(h_{LH_2} \cdot A_{LH_2})} \tag{2.9}$$

where A is the area for heat transfer on helium/liquid hydrogen side respectively, and

$$h = 0.023 \cdot \frac{C_P \cdot G^{0.8} \cdot \eta^{0.2}}{D_e^{0.2} \cdot Pr^{0.6}} \tag{2.10}$$

where G is the mass flow per unit area of the flow, η (g/cm s) is the fluid's dynamic viscosity, D_e is the wetted perimeter and Pr is the Prandtl number (dimensionless) for the fluid (Pr = $\eta \cdot C_P$/k, where k (W/cm K) is the thermal conductivity). For nominal running conditions at a cryogenic pump speed of 30 Hz the heat transfer coefficient was estimated to be U = 285 W/K for a heat exchanger with no leakage. At the same pump speed the data yielded a value for the heat transfer coefficient of U = 214 W/K, fig. (2-9b). The discrepancy comes from the model computed value for U, which assumes that the temperature is constant across the fins, while in reality it is a gradient from the helium side to the tip of the fins, and the gradient varies along the heat exchanger. Also, originally the heat exchanger had nylon rope wrapped around the fin tubing to force the liquid hydrogen flow to go around the fins, but the rope was removed because of concerns that it may block the flow on the hydrogen side, and due to this the heat exchanger has some leakage that depends on the flow speed. The leakage has the effect of reducing the value of the heat transfer coefficient from what you'd get by using eqs. (2.9-2.10).

The mean temperature difference across the heat exchanger, ΔT_{LM} has the expected behavior in frequency, it decreases with the increase in pump frequency, see fig. (2-9a), but it is not straight at high rotational frequencies of the cryogenic pump and high heat loads which is also related to the heat exchanger's leakage. The effectiveness, see fig. (2-9c), is very close to the theoretical estimate for a counter flow heat exchanger, for N$>$ 3 it should be above 0.95. In our heat exchanger the number of heat transfer units is at least 3.55, and the measured effectiveness is above 0.98 for pump frequencies higher than 30 Hz. The heat exchanger was tested for maximum heat transfer in Dec 2003 and up to the maximum power on the HPH (1000 W) was able to remove the heat load from the liquid hydrogen, while keeping the target at the nominal running point (19 K, 1.7 atm). The helium coolant flow was about 80% of the maximum deliverable by the ESR on the 15 K supply, so in principle this type of heat exchanger is able to remove more than 1000 W of heat load from liquid hydrogen.

At the end of the testing period in liquid hydrogen, after boiling the liquid, when the temperature in the cryogenic loop was about 50 K, a cryogenic pump speed scan was performed and the pump run to 73 Hz. From this running frequency when the controller was powered off the shaft stopped turning in 23 seconds, as read on the tachometer readback, meaning that there is no significant friction impeding the rotation in cryogenic conditions.

2.4.2 In-beam tests

A set of tests were done with beam on target, scanning the target in beam to check the alignment, calibrating the HPH and checking the PID feedback loop with beam. The target has been scanned by stopping the beam, moving the target a known amount on x(y), restoring the beam and recording the current from a background scintillator detector on a photomultiplier tube, located close to the target. For a beam spot of 2 by 2 mm on the target, it was found that the target was centered on the beam axis to better than 1 mm in both x and y, within the alignment specs for the experiment (by doing the same scan, the same precision in target alignment was found at the beginning of the second engineering run, in December 2003). From the HPH calibration it was determined that at full beam on target, 40 μA, the target consumes about 320 W of cooling power. Theoretical estimates of target heating from a 40 μA, 3 GeV electron beam are around 300 W (Al windows included). The difference of 20 W is cryogenic pump heating and losses to the environment. This number is so small due to the fact that the target sits inside the SMS, surrounded by a liquid nitrogen shield, the cryogenic loop is wrapped in at least ten layers of superinsulation (except the Al target cell, which is bare), and the fact that the cryogenic motor produces small heat load in cryogenic conditions.

Liquid hydrogen operation

The target was operated with liquid hydrogen at 19 K, or 3 K subcooled liquid at 1.7 atm. The cryogenic pump rotated at 31 Hz with speed fluctuations of less than 0.1 Hz over months long continuous running. Since the helicity signal used to compute the PV asymmetry in this experiment, changes on a 30 Hz basis, the pump was run at a slightly different frequency from 30 Hz to avoid possible sources of systematics in the asymmetry measurements, due to our pump rotation. The amplitude of the hydrogen cell vibrations due to the pump's rotation at full speed (75 Hz) was measured and found to be below 0.01 mm. Since these vibrations do not happen at 30 Hz it is not expected that they correlate with the helicity signal. The electron beam's natural motion on target is about ten times bigger than the cell's vibrations. The contribution from the cell's vibrations to the beam position on target is then expected to be negligible. The stability of the cryogenic pump rotation over time is a strong indication that the pump induced hydrogen cell vibrations are also stable in time. Target instabilities with beam trips are well mitigated by the HPH on PID. The temperature excursions seen when the beam trips or comes on target are less than 0.2 K and last about 20 s. The liquid hydrogen relative density change due to beam trips is 0.3 %. The relative normalized yield change in our detectors is about 1 %, the difference is due to the fact that the beam, when ramped up to nominal current, it also drifts in space by as much as a few mm. To avoid this problem a beam trip cut was implemented in the data acquisition that excludes about 25 s of data after the beam comes on target. With relatively stable beam on target (40 ± 0.5 μA) the PID maintains the temperature constant to within 0.02 K (relative target density change expected from PID stabilization is 0.03%, completely negligible for this experiment).

Target density variations studies have been done during both G^0 engineering runs. The effects of target density variations and the results of the studies done on them are presented and described in the appendix B.1. The following summary on the target system includes the results of the target density variations studies.

2.4.3 Target summary

In ten months of operation experience the G^0 target system has performed flawlessly, without a single major incident. At the nominal beam of 40 μA and spot size of 2 mm, with the pump running at 31 Hz, target density fluctuations increase the asymmetry width by at most 2%. In the same nominal conditions the global relative yield reduction of the G^0 detector due to the target density reduction, has an upper limit of 1.5%. The part of the asymmetry width due to target density fluctuations vary nonlinearly with inverse pump speed (constant beam conditions). The target density fluctuations mechanism is not dominated by micro-bubble formation and by heating at the exit window. The target has a capacity of at least 1000 W power load while staying 3 K subcooled liquid. The effects produced by the target satisfy the requirement of negligible systematic effects in a parity-violation experiment.

2.5 The FPD and electronics package

The 3 GeV longitudinally polarized electron beam delivered by the CEBAF machine in bunches of 32 ns is rastered on a square area of nominal 2 mm side at the target with 95% uniform energy density. The electron beam reaching the target travels through three thin Al windows, a cold gas helium cell and a liquid hydrogen cell before it reaches the beam dump. Positively charged particles originating in the target with the right kinematics get focused by the superconducting magnet's field onto the FPD. The helicity of the electron beam changes every 33 ms and on this time scale time of flight spectra are accumulated for individual detector hits. The FPDs and electronics for the forward angle mode in G^0 will be described in what follows.

2.5.1 The G^0 FPD

In the forward angle mode particles are detected in a scintillator array of segmented detectors placed in the focal surface of the SMS (FPDs). The detectors [62] are shaped to follow iso-Q^2 bins about the beam axis in the Q^2 range 0.1 to 1 (GeV)^2. The FPDs are placed in 8 octants in an Al ferris wheel shaped frame that supports the octants. The octants are clocked in between SMS coils with octant 1 situated up along the vertical axis to the beam line. The G^0 FPD was built in two separate halves, four octants being built by the North American collaborators (referred to as the NA FPD) and four octants by the French collaborators (referred to as the FR FPD). Pictures of FR and NA octants can be seen in fig. (2-10). In the ferris wheel the octants have been mounted staggered, one FR and one NA with the NA octants mounted along the axes of the G^0 coordinate system perpendicular to the beam line (y axis is to beam up, x axis is to beam right in the horizontal beam bending plane, and z axis is along the electron beam direction), and the FR octants at 45^o with respect to the y and x G^0 axes. For analysis purposes the octants are numbered from one to eight, with one being the NA octant situated to beam

Figure 2-10: Left NA, right FR octants with the 16 pairs of arc shaped iso-Q^2 FPD segments each.

up and continuing clockwise. The NA octants have odd numbers and the FR octants have even numbers. The 16 FPD segments in an octant can be viewed in figs.(2-1, 2-11).

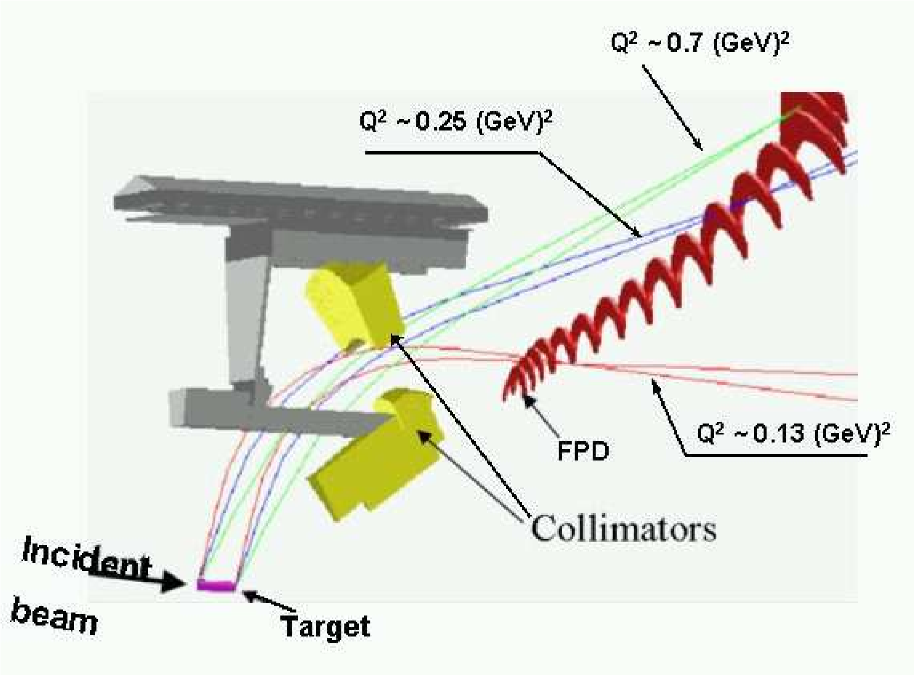

Figure 2-11: Detection scheme in forward angle mode. The collimators inside the SMS define the detector acceptance for particles. Scattered charged particles trajectories are shown for three Q^2 bins.

The FPD numbers increase from the beam line out, with the first FPD the closest to the electron beam line and 16 the farthest one out. This is also the direction of increase for the Q^2 bins, with the first 14 FPDs containing individual Q^2 bins with values from 0.12 to 0.41 $(\text{GeV})^2$, FPD 15 alone spans a Q^2 range from 0.4 to 0.9 $(\text{GeV})^2$ and FPD 16 does not have a Q^2 bin, and it is used for background studies. An FPD segment is made of a pair of Bicron BC408 scintillator paddles separated by a 3 mm thick sheet of polycarbonate (NA) or Al (FR). The two scintillator paddles are called the front and back FPD and are used in a coincidence method for particle detection to improve the background rejection. After an arc of about 45^o the scintillators are continued with light guides to the back of the octant where the light guides connect to PMTs. This setup keeps the PMTs in a region of low magnetic field. The individual PMTs are also shielded by a sheet of μ-metal to reduce the fringe magnetic field at their location. The NA FPDs use Philips XP2262B 12 stage PMTs with custom built-in Zener bases while the FR FPDs use Photonis XP2282B 8 stage PMTs with custom made bases, different from the NA ones. An octant has 16 FPD pairs, each pair has 4 attached light guides, which makes for a total of 64 PMTs for one octant, and a total of 512 PMTs for the whole FPD. The 512 PMTs produce the FPD analog signal that goes to the time encoding electronics for digitization and histogramming of individual FPD hits in the ToF spectra.

The solid angle acceptance of the whole FPD is about 1 sr. The angular acceptance for protons, given in table 1.6, has a range between about 52^o and 76^o. The elastic recoil proton scattering angle decreases from low number detectors to high number detectors as can be seen in fig. (2-11), with large scattering angle protons being focused by the SMS on the low number FPDs and small scattering angle protons being focused by the SMS in the high number FPDs.

To achieve a good temporal resolution in an FPD a detected particle has to produce at least 40 photoelectrons while passing through the FPD. Measurements done using a ^{106}Ru β source yielded a minimum detected number of photoelectrons extrapolated for proton detection (forward angle mode) of several hundred for all the FPDs while for electron detection (backward angle mode) of at least 70 photoelectrons for all the FPDs. The measurements were done on FPDs with the light guides and PMTs installed as in the actual experiment.

2.5.2 The G^0 electronics

There are two electronics packages that serve the G^0 FPD, time encoding electronics and Fastbus electronics. The time encoding electronics package is the main electronics in the G^0 detection scheme, while Fastbus electronics plays an auxiliary role. Similar to the FPD package, the time encoding electronics has been built separately for the NA and FR parts of the G^0 FPD. The detection technique is based on a time of flight (ToF) method and is common to both FR and NA electronics packages, but the specific implementation is different between the two. An overview of both detection implementations can be viewed schematically in fig. (2-12). From the time the electron beam hits the G^0 target it takes between 7 and 24 ns for charged particles originating in the target region to reach an FPD. Particle identification is done in the ToF spectrum through differences in arrival time. It takes on average about 8 ns for positive mesons, mostly π^+, to reach an FPD and about 20 ns for the elastically recoiled protons to get to the same FPD. The G^0 beam repetition rate is about 31 MHz, which gives a ToF spectrum of 32 ns. The electron beam helicity changes with a frequency of 30 Hz. For a helicity state the electronics histograms FPD ToF counts. The data gets transferred to the acquisition system during the helicity flip period of 200 μs at the end of each 33 ms (30 Hz) of a helicity state. As seen in the fig. (2-12) a PMT signal from an FPD, for both FR and NA, is split and part

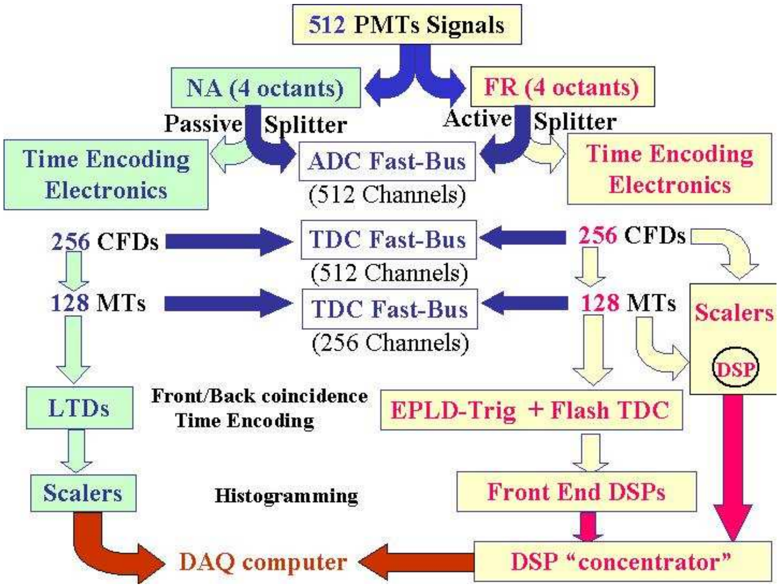

Figure 2-12: Detection scheme for the G^0 forward angle mode, both FR and NA time encoding electronics are shown, along with the Fastbus electronics.

of the signal is directed to the time encoding electronics, part of the signal is directed to a set of monitoring electronics packages that work under Fastbus. A hit is recorded in an FPD segment if there is a coincidence among the four PMTs instrumented for it (two for the front scintillator and two for the back scintillator). This scheme, called the 4-fold coincidence, rejects singles events, which are defined as the firing of at most 3 PMTs attached to the same FPD segment in the same coincidence window.

In the NA time encoding electronics [63] the PMT signal goes to a constant fraction discriminator (CFD) first, fig. (2-13). The CFD selects incoming signals that have the pulse height above a certain user set threshold, eliminating low level signals that are produced by thermal noise in the FPD or the PMT. The CFDs output signals from the two PMTs at the end of an FPD scintillator paddle then go to a meantimer module that finds the mean time of the two PMT signals. In this way the timing of an event is made independent of the hit location along the scintillator paddle. For each scintillator paddle there is a meantimer, and for each FPD segment there are two meantimers, one for the front and one for the back scintillators. The signals from the two meantimers for the same FPD segment go to a latching time digitizer (LTD) module, which analyzes them in a coincidence window of a few ns. Time digitization is done inside the LTD with two 16-bit shift registers, each with a time resolution of 2 ns. The two shift registers are 180^o out of phase with each other, in the end producing a time resolution of 1 ns for the ToF spectra for the NA FPD. The shift registers are timed by the 499 MHz (2 ns) CEBAF master clock signal synched to the G^0 beam pulse arrival, fig. (2-14). The NA FPD signal is time encoded using a gated clock signal, which every 32 ns turns off the master clock for 4 pulses (8 ns) and turns it on for the remaining 12 pulses, for a period of 24 ns. This is the effective range of the NA ToF spectrum, 24 ns out of 32 ns G^0 beam repetition period, with an absolute time resolution of 1 ns. In the end the output of the LTD is sent to scalers, which accumulate the ToF histogram for 33 ms. The scalers are read by the data acquisition computer at the rate of helicity reversal signal of 30 Hz.

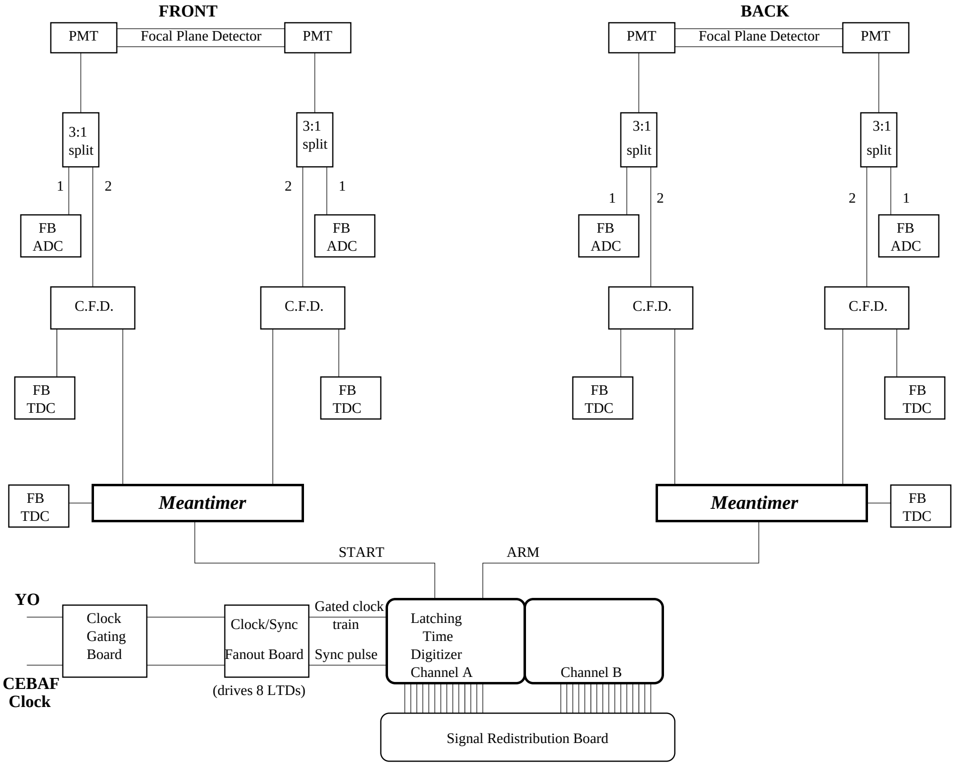

Figure 2-13: NA FPD-electronics detection scheme. Front and back refer to the respective FPD scintillators that belong to the same NA FPD segment.

The FR electronics is custom designed and fully integrated in a DMCH-16X module, fig. (2-15). The DMCH stands for Discriminator, Meantimer, time to digit Converter and Histogramming, while 16X stands for 16 channels, meaning that one module can serve 16 scintillators or 8 FPD segments, and X for using the VXI standard. In principle the FR electronics is similar to the NA electronics with the addition of a more compact integration, a time resolution for the ToF spectra of 0.25 ns, four times the NA ToF time resolution, and an effective ToF range of 32 ns, or the full G^0 beam repetition period (a FR ToF spectrum has 128 timebins, each with a nominal 0.25 ns width).

The Fastbus electronics, fig. (2-12) is auxiliary to the time encoding electronics and is used for monitoring. The modules used are Fastbus ADCs for monitoring the amplitude of the FPD signal and TDCs for ToF studies. The acquisition rate is less than 1 kHz to

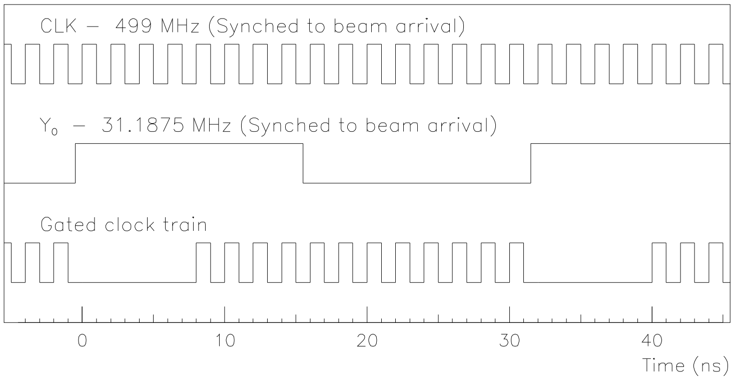

Figure 2-14: The clock train. YO signal is the G^0 beam pick-off signal. The horizontal scale is ns. The gated clock signal period is the same as the YO signal period of 32 ns.

reduce the acquisition deadtime, and the trigger is given by a prescaled YO signal. The time resolution of the Fastbus TDC is 50 ps, which makes them suitable for monitoring both the FR and NA ToF spectra.

The measured counting rate in a single FPD segment is of the order 1-2 MHz at an electron beam current of 40 μA on the liquid hydrogen target. The detection deadtime affects the measured counting rate and subsequently has an effect on the measured parity-violating asymmetry (section 3.2.4). The deadtime fraction, f, is defined as the fraction of the detection time that the detection package is blind to incoming events due to the processing of an event. The deadtime is the period of time, τ, it takes for the detection package, or segments of it, to recover after starting to process an event.

Deadtime effects in the time encoding electronics have been addressed [64, 65] and the deadtime fraction for the FR and NA FPDs has been determined to be between 10-15% depending on the FPD number. The detection in both FR and NA electronics has been implemented such that the pulse after an event happens is neutralized. In this scheme, called the next pulse neutralization (NPN), an artificial deadtime period of known length is introduced in the data and analytically corrected for at replay time. Although this scheme has been refined during the two engineering runs for the forward angle mode, a

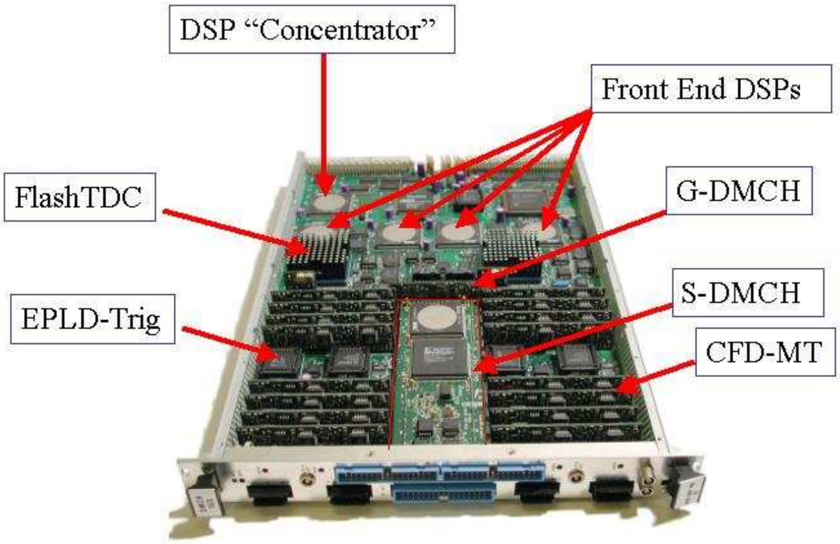

Figure 2-15: FR DMCH module. DSP is a digital signal processor, EPLD is a programmable logic device, Flash-TDC is a custom ASIC (application specific integrated circuit) designed by IPN Orsay. S-DMCH is a DMCH with scalers, and G-DMCH contains an internal generator for testing CFDs thresholds and meantimer outputs.

residual deadtime fraction of about 4% remains for a FPD after the deadtime correction procedure is applied to the measured rate. As it will be seen in section 3.2.4 the residual deadtime amounts for a negligible effect on the measured asymmetry and on the event statistics in the experiment.

2.6 The G^0 beam

In the G^0 forward angle mode the detection scheme counts FPD hits using a ToF method with a periodicity of 32 ns. The G^0 period of 32 ns is determined by the time of flight of particles between the target and the FPDs. The G^0 detection scheme in the forward angle mode cannot be accommodated by the nominal structure of the CEBAF electron beam, which pulses at 499 MHz or with a periodicity of 2 ns. For this reason the G^0 experiment needs an electron beam with a period of 32 ns. As the G^0 experiment measures parity-violating asymmetries of the order of ppm, in addition to the 32 ns time structure, the G^0 beam has to be longitudinally polarized and be suitable for a parity violation measurement, which means that it has to have small helicity correlated properties. The schematic of the CEBAF machine can be viewed in fig. (2-16). As many as three electron beams can be accelerated simultaneously by the superconducting Nb linac cavities of CEBAF, which are located on the South and North Linacs. The electron beams are delivered to the three experimental halls. The maximum electron energy achievable by the present configuration of CEBAF is 6 GeV with a maximum

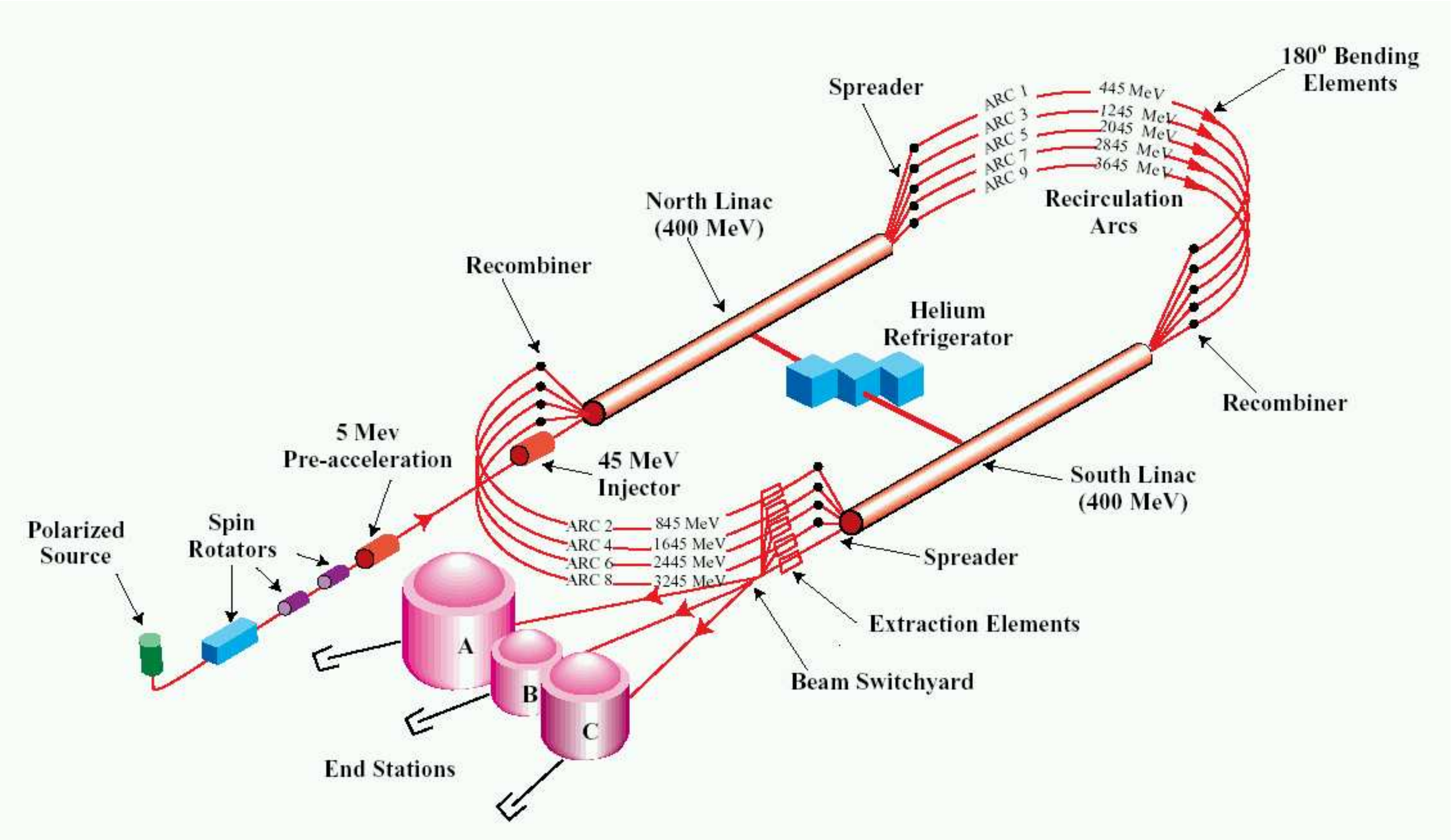

Figure 2-16: CEBAF machine [68]. The G^0 experiment is located in Hall C.

electron current of 200 μA. The G^0 experiment runs in the forward angle mode with a longitudinally polarized electron beam with a nominal current of 40 μA and an energy of 3 GeV.

2.6.1 Polarized source for G^0

The polarized electron beam is produced by the polarized source. The longitudinally polarized G^0 electron beam is produced by a laser at 31.1875 MHz from a strained GaAs crystal [69, 70]. The production of polarized electrons by incident laser light on a GaAs crystal is shown in fig. (2-17). A GaAs crystal is a direct band semiconductor crystal with an energy gap of $\sim$ 1.4 eV. Photons of appropriate energy ($\lambda \sim$ 850 nm) that are shined at the crystal are absorbed by electrons in the valence band, which are excited into the conduction band of the crystal. To completely escape the crystal lattice the conduction band electrons have to overcome a 4 eV energy gap between the conduction band and the vacuum level. This energy gap can be reduced to almost zero by coating

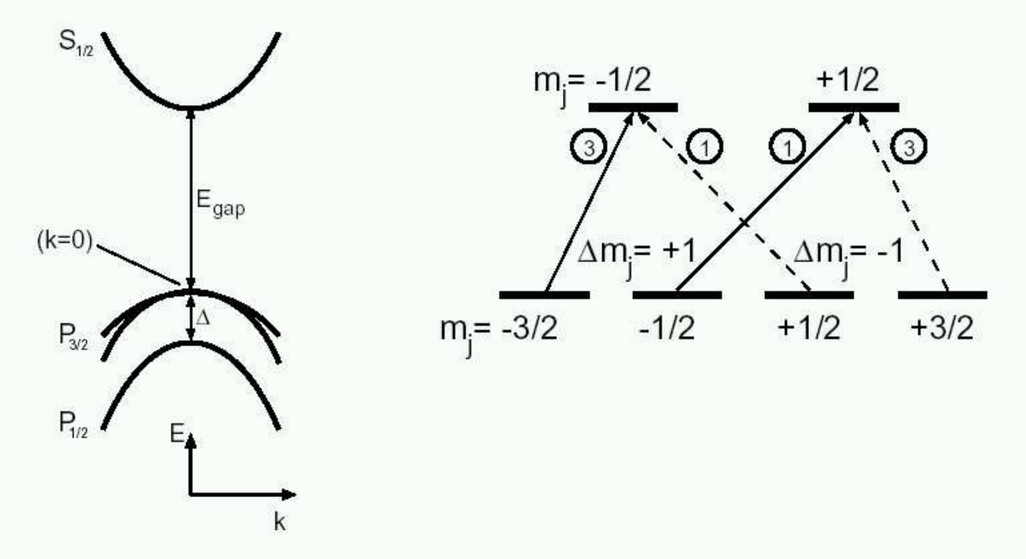

Figure 2-17: Energy dispersion curves for the valence and conduction bands of GaAs are shown on the left, while the electron photoexcitation selection rules are on the right.

the crystal surface with Cs, and if the substrate is also oxidized the vacuum energy level drops below the conduction band level and the surface is said to have negative electron affinity. If the incident light is polarized then the outgoing electrons from the crystal surface will be polarized. Maximum theoretical electron polarization achieved this way is 50% and is limited by the degeneracy of the energy levels in the conduction bands.

Higher polarizations are achieved with a three layers GaAs crystal [71]. On a substrate of GaAs a layer of GaAsP is grown and on top of it another layer of GaAs. The GaAsP layer exerts mechanical strain on the GaAs layer due to the lattice constant mismatch between them and acts as a perturbation to the lattice potential. This has the effect of lifting the degeneracy of the electron energy levels in the valence band of GaAs. Polarizations for outgoing electrons as high as 80% are attainable at Jefferson Lab using this kind of strained GaAs crystal. If the crystal is made into a cathode then the outgoing electrons can be collected and formed into an electron beam that can be accelerated to some desired energy and used to probe a target, which is essentially what happens in the G^0 experiment.

The G^0 laser is a commercially available unit. It consists of a tunable Ti:Sapphire crystal laser produced by a pumping solid state laser, which has a 532 nm wavelength and 5 W. The Ti:Sapphire laser is mode locked in a 4.84 m long cavity, shown schematically in fig. (2-18), and can be tuned for wavelengths between 770-860 nm at 31.1875 MHz. Output laser power in excess of 300 mW at a wavelength of 840 nm with pulse width of 70 ns have been achieved with the G^0 laser. The strained GaAs crystal has a typical quantum efficiency of 0.2% for an incident laser of wavelength 840 nm, and can deliver 1 μA of 70-80% polarized electron beams for 1 mW of incident laser power on its surface.

As the G^0 beam is produced as a subharmonic ($31.1875 = 499/16$) of the CEBAF master repetition rate, the space charge associated with it is 16 times higher than it is for a typical CEBAF electron beam, which causes complicated beam transport problems through the CEBAF machine. Nevertheless, 40 μA G^0 beam intensities have been achieved during the first engineering run, in January 2003, and stable nominal current G^0 beam with parity quality (see section 2.6.2) has been achieved during the second engineering run, in winter 2003-2004. The electron beam position and charge along the Hall C beamline is measured in several places. For G^0 the position of the beam on target (two positions, along x and y axes, and two angles, θ_x and θ_y) was extracted using two stripline [67] beam position monitors (BPMs) situated upstream of the target location. For the first engineering run the distance between the center of the most downstream BPM and the entrance window to the target cell was 3.4 m, and the distance between the centers of the two BPMs was 2.55 m. The beam monitors for charge measurements are similar to the ones for beam position measurements. The energy was measured with a BPM mounted in the Hall C arc in a dispersive region for the beam. The position of the beam in the in-bend plane in this monitor is calibrated for relative energy determination.

A schematic of the polarized source table is shown in fig. (2-18), where the lasers for all three halls are represented. There are several optical elements that the G^0 laser beam goes through, from the output of its box until it reaches the photocathode and produces the electron beam there. The important elements on the laser table, fig. (2-18), for a parity experiment are: the IA cell, the PZT mirrors (Hall C and common), the helicity Pockels cell and the insertable half wave-plate. These elements will be presented in the next section 2.6.2.

2.6.2 Parity quality G^0 beam

The G^0 experiment measures parity-violating asymmetries, which have been described in chapter 1.

The helicity state of the electron beam changes with a frequency of 30 Hz and the measured FPD asymmetries are formed among four consecutive helicity states, two with positive helicity and two with negative helicity (see chapter 3 about how the measured

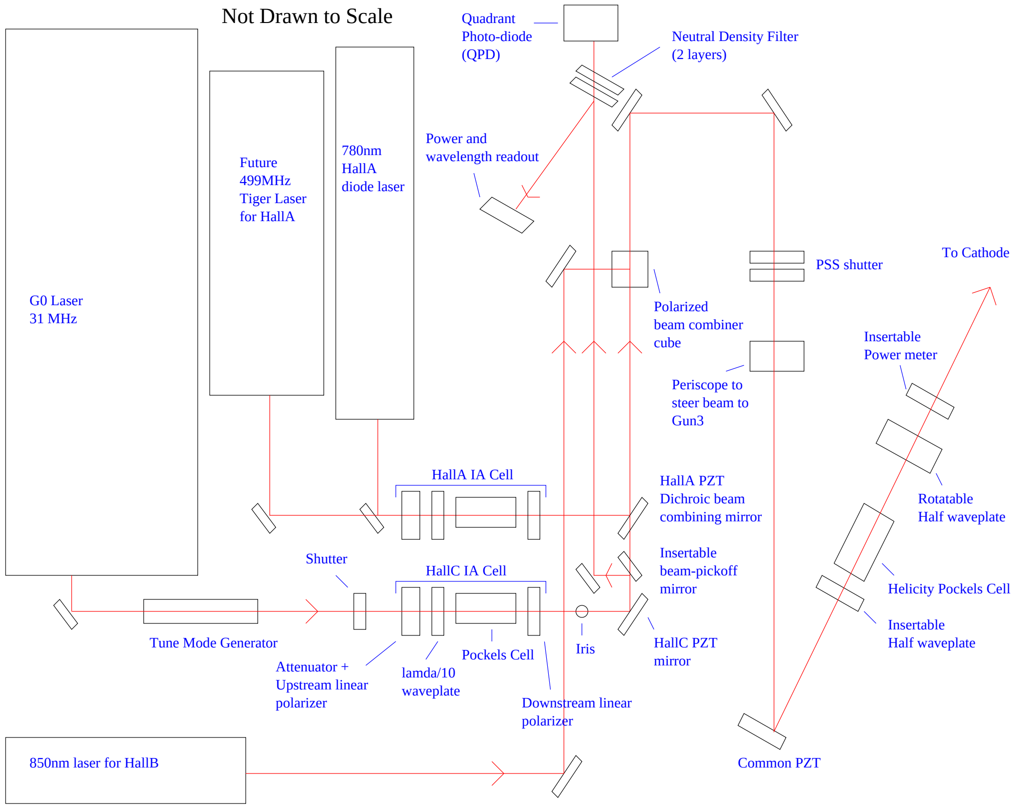

Figure 2-18: Polarized source laser table at CEBAF.

FPD asymmetries are defined, all other asymmetries or differences for a certain observable are formed in this way). The FPD asymmetries are of the order of a few ppm.The G^0 experiment aims to measure the parity-violating asymmetries with about 5% uncertainty or about 0.1 ppm. To accomplish this goal it is necessary that the false asymmetries that affect the measured asymmetries are of the order of 0.1 ppm or less. Variations in helicity correlated beam parameters such as: beam position, intensity and energy (see section 3.2.5), are a source of false asymmetries for the measured FPD asymmetries. The polarized electron beam has parity quality if the helicity correlated electron beam parameters meet certain requirements. When averaged over the data taking period the beam charge asymmetry should be less than 1 ppm, the beam position differences at the target should be less than 20 nm, the beam angle differences at the target should be less

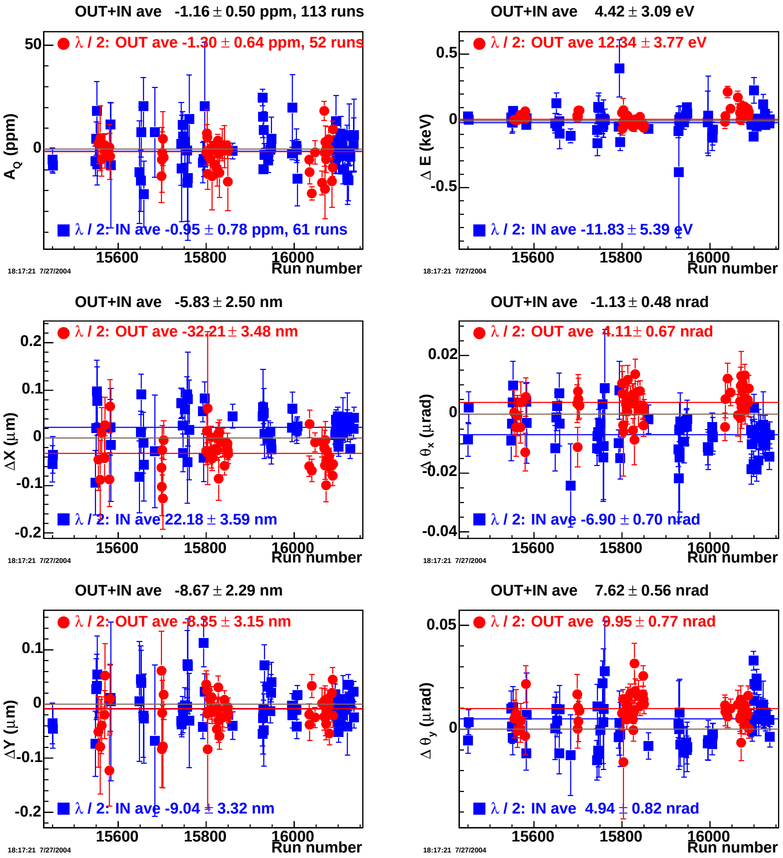

Figure 2-19: Parity quality properties of the G^0 beam. IHWP states are shown separately, IHWP = IN with squares, IWHP = OUT with full circles. Data on a run by run basis.

than 2 nrad, and the energy difference should be less than 75 eV.

The electron beam helicity correlated charge asymmetry is controlled over time with a feedback system that uses the IA (intensity attenuator) cell, which is situated on the laser table, fig. (2-18). The cell [69] is a low voltage Pockels cell that is coupled to a $\lambda/10$ wave-plate and a polarizer, and modulates the intensity of the light at 30 Hz. The feedback uses a BCM in the Hall C beamline to determine the beam charge for a helicity state. The control of the feedback is from a computer. Typically the cell has a gain of 200-300 ppm/V and a dynamical range of ± 5 V around the neutral position, which is 5 V. The cell slope (charge ppm/V) is measured regularly doing so-called IA scans. An

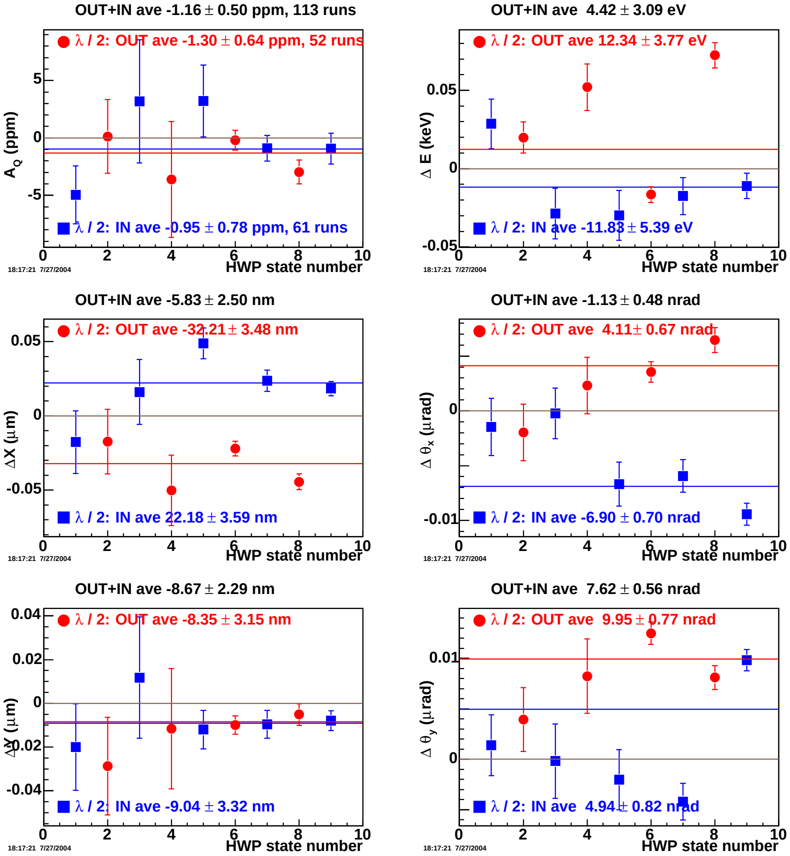

Figure 2-20: Parity quality summary of the G^0 beam. IHWP = OUT full circles, IHWP = IN squares, data points are averages over the runs in a IHWP state.

IA scan consists of a set of short data runs, when the electron beam charge asymmetry is measured at three voltage settings for the IA cell, usually 1, 5 and 9 V. The new slope is fed to the feedback system.

The electron beam helicity correlated position differences at the target are controlled in a feedback with a different element on the laser table, the PZT mirror, fig(2-18). The PZT is a piezo-electric transducer (Plumbum Zirconate Titanate) that stirs a mirror attached to it at 30 Hz. The mirror sits in the laser path and corrects for both vertical and horizontal electron beam positions differences at the target.

During the first engineering run the PZT slopes changed over time. Correlations have been observed between the IA and the beam position differences at the target, and also rather large charge asymmetris were induced by the PZT mirror. Due to these cross-talk effects the PZT feedback was not used during the first engineering run, but the IA feedback was used and it worked well.

The polarization of the laser light is established by the helicity Pockels cell, fig. (2-18). The helicity signal is a pseudorandom sequence that changes the voltage applied to this cell at 30 Hz and picks between the two states of circular polarization for the light that passes through the crystal on its way to the photocathode, where it produces the polarized electrons that are fed to the accelerator.

Parity experiments use routinely a so-called insertable half wave-plate (IHWP), fig. (2-18). This $\lambda/2$ can be manually inserted in the laser path or taken out. When inserted, it reverses the laser polarization and subsequently the electron beam helicity with no electronics involvement. As a consequence all parity-violating observables measured in the experiment have to reverse sign. The IHWP offers a simple and powerful check for systematics in parity-violating experiments. The IHWP is periodically inserted in the laser path and subsequently taken out. The aquired data is labeled IN or OUT according to the state of the IHWP. Helicity correlated beam parameters measured over all the states of the IHWP during the asymmetry data acquisition for the data analyzed in chapter 3 are represented in the plots in figs.(2-19,2-20).

For the first engineering run, the parity quality G^0 beam has been mostly achieved. The charge asymmetry is within specs (¡ 1ppm) for the average over $IHWP = IN$ and within the error bars for $IHWP = OUT$, with the total average $A_Q = -1.16 \pm 0.5$ ppm (over about 10% of the asymmetry data required for the forward angle G^0 run). The helicity correlated beam position differences are within specs for both IHWP states for y and somewhat off for x, but when combined together the average is within specs. Helicity correlated beam angle differences at the target are off for both x and y axes and for both states of the IHWP, but overall all are less than 10 nrad. The average over the two IHWP states for θ_x is within specs and is still off for θ_y. The helicity correlated beam energy differences are well within the specs for both states of te IHWP. The size of the false asymmetries caused by these helicity correlated electron beam parameters will be determined in section 3.2.5.

2.7 Beam polarization measurements

During the asymmetry data taking, at regular intervals, the polarization of the electron beam was measured with the standard Hall C Møller polarimeter [73]. Typically Møller polarimeters use a thin iron foil as target for the incoming electron beam. In the Hall C Møller polarimeter the iron foil has its outer shell electrons polarized along the electron beam direction by using a magnetic field of 4 T. The polarization of the electron beam is determined by measuring the asymmetry in the Møller scattering rates at 90^o in the center of mass (CoM) between the polarized electron beam and the polarized electrons in the thin iron foil [72]:

$$\frac{d\sigma}{d\Omega} = \frac{d\sigma_0}{d\Omega}[1 + P_Z^T P_Z^B A_{ZZ}(\theta)] \tag{2.11}$$

$$A = \frac{d\sigma^{\uparrow\uparrow} - d\sigma^{\uparrow\downarrow}}{d\sigma^{\uparrow\uparrow} + d\sigma^{\uparrow\downarrow}} = A_{ZZ}(\theta) P_Z^T P_Z^B \tag{2.12}$$

where $\frac{d\sigma_o}{d\Omega}$ is the unpolarized cross section, $A_{ZZ}(\theta)$ is the analyzing power, and P_Z^T, P_Z^B are the longitudinal polarization of the target and beam respectively. At 90^o CoM, the analyzing power is $A_{ZZ} = -\frac{7}{9}$ and with the target polarization known (0.08043 ± 0.00015 at 4 T) the longitudinal polarization of the electron beam can be determined in this way. The Hall C Møller polarimeter typically runs at low beam currents (~ 1 μA) and can achieve polarization measurement accuracies of better than 0.5%.

The results for the beam polarization measurements [74] during the first G^0 engineering run are summarized in fig. (2-21). In fig. (2-21) the runs are chronologically ordered.

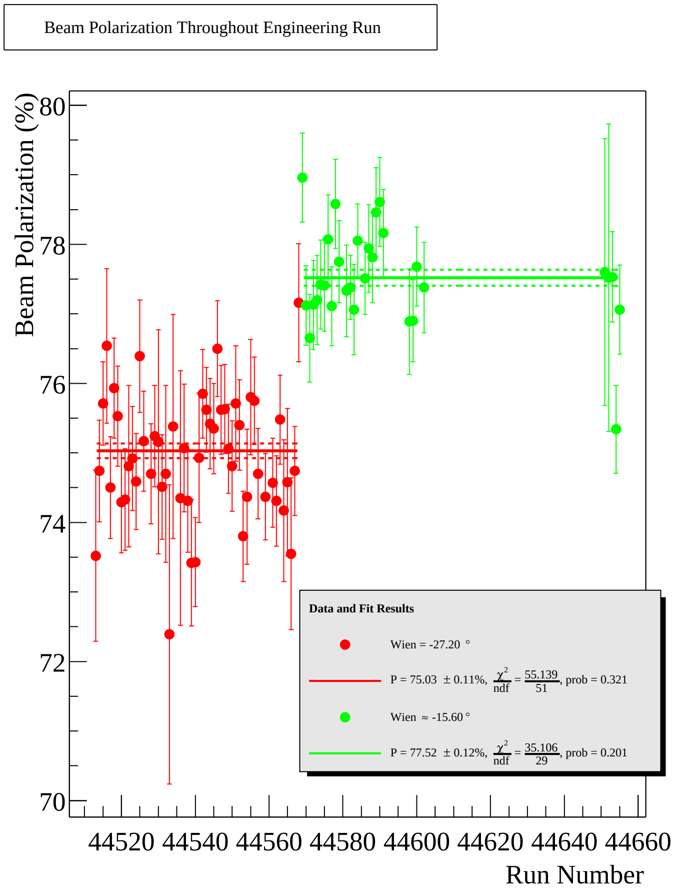

Figure 2-21: Electron beam polarization measurements with the Hall C Møller polarimeter during the first G^0 engineering run.

The runs on the left hand side of the plot average to about 75.03 ± 0.11% and were taken with the Wien filter set for about 5% transverse beam polarization (a Wien filter is a cross fields cavity, $E \times B$, which exactly cancel each other in the cavity, so a passing through electron beam doesn't sustain any net force, but its polarization precesses about the magnetic field). The runs on the right hand side were taken with the Wien filter set for longitudinal polarization at the target (normal running). The average longitudinal electron beam polarization for this data taking was 77.52 ± 0.12%. This number has been used in the next chapter to correct the measured asymmetries for subunity beam polarization.

2.8 The G^0 data acquisition

The data acquisition for the G^0 experiment is managed under Cebaf Online Data Acquisition or CODA [75] that runs on a Sun workstation under a Solaris operating system in the Hall C Counting House. A schematic of the G^0 data acquisition system can be viewed in fig. (2-22). Slow controls are managed under Experimental Physics and Industrial Control System, EPICS [76]. These include control and monitoring of the G^0 subsystems and various other interface systems like beam parameters, beam parity quality feedbacks,

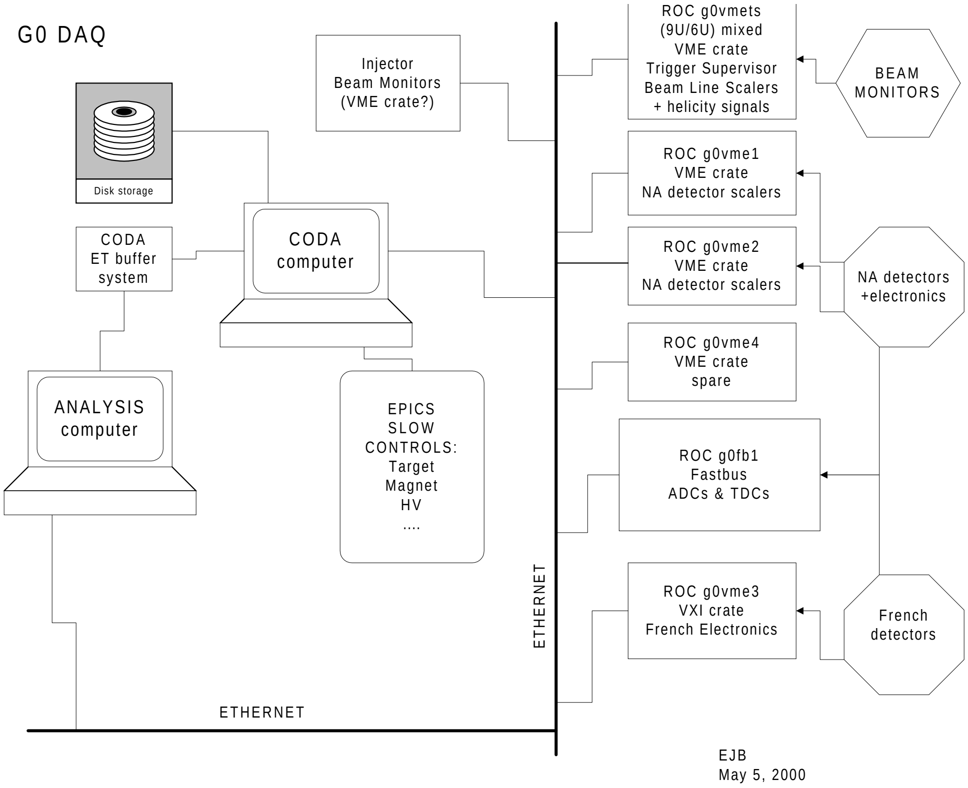

Figure 2-22: Schematic of the data acquisition system used in the G^0 experiment. ROC stands for Read-Out Controller. VME stands for Versa Module Europa, which is a flexible bus system with a data transfer rate of about 20 Mbytes/s.

etc. which are all part of the greater CEBAF EPICS database. Slow controls data are archived by data loggers that have integrated plotting capabilities available over the internet.

The FPD asymmetry data along with the beam parameters data are managed by the coda computer. Part of the data is made available to the online analysis computer for histogramming. This real-time analysis is essential for monitoring the quality of the data, the functionality of the beam feedback systems and of various electronics packages in the chain of asymmetry data acquisition. The online analysis package was written in C++/ROOT [77]. The accumulated data is stored on disks. The accumulation rate for these data was about 2 MBytes/s (it will take about 7 TBytes to store the data for the whole forward angle run, about 1000 h).

The data stored on disks is replayed using the offline replay engine. The replay engine was written in C++/ROOT. The results of the offline replay along with useful information about the slow controls are stored into a database. The G^0 database is based on a Structured Query Language (SQL) and was setup using the open source database server MySQL [78]. The replaying of this data set will be described in the next chapter.

Chapter 3

Data analysis

3.1 Introduction

The G^0 apparatus was operated for the first time during the first G^0 engineering run, from October, 2002 to January, 2003. The commissioning of the apparatus has been mostly completed by the end of year 2002 with work left to be done on the stability of the parity quality of the G^0 beam. At the end of this engineering run, through January, 2003, data has been accumulated on asymmetry running.

This chapter contains the analysis for the G^0 FPD (focal plane detector) physics data taken during the first G^0 engineering run. The physics data were about 9.7 C of beam charge on target, of which 4.57 C with the IHWP = IN and 5.13 C with the IHWP = OUT. The individual steps in correcting the measured parity-violating asymmetries in the G^0 forward angle mode elastic $\vec{e}p$ scattering are described in what follows. Linear combinations of vector strange form factors, electric and magnetic, as a function of 4-momentum transfer Q^2, are extracted from the corrected FPD asymmetries.

3.2 Analysis program

The beam charge accumulated on target for asymmetry running during the first G^0 engineering run represents about 10% of the 100 C of beam data proposed for the G^0 forward angle mode run. This data sample yields a 3σ measurement of the parity-violating asymmetries in the G^0 forward angle running mode.

3.2.1 Measured asymmetry

The parity-violating asymmetry measured in this experiment was defined theoretically in section 1.3.2, eq. (1.15). The time unit for measuring the asymmetry is a quartet (also noted QRT). A quartet is formed of 4 macro-pulses (MPS). One MPS lasts 33 ms (30 Hz) and has about 10^6 beam pulses, each 32 ns long. All the electron beam bunches in one MPS have the same helicity. The electron beam helicity is flipped by the helicity Pockels cell with a frequency of 30 Hz. The quartets have either a structure like $+--+$ or complemented $-++-$. The signs $+, -$ signify MPSs during which the electron beam helicity was either positive or negative. For each FPD segment particle counting data is histogrammed in ToF spectra. The ToF spectra are binned in the electronics in 24 timebins of 1 ns nominal width for the NA FPD and in 128 timebins of nominal width of 0.25 ns for the FR FPD. The number of particles, N_p, detected in one MPS in one of the timebins of a FPD ToF spectrum is normalized to the beam charge measured for the same MPS, Q, and is called normalized yield, Y [1/nC]

$$Y_{ij} = \frac{N_{p,ij}}{Q_j} \tag{3.1}$$

where i is the timebin index in the ToF spectrum and j is the MPS index. The ToF spectrum for FR FPD 7 is shown in fig. (3-1). The normalized elastic yield*, Y, is

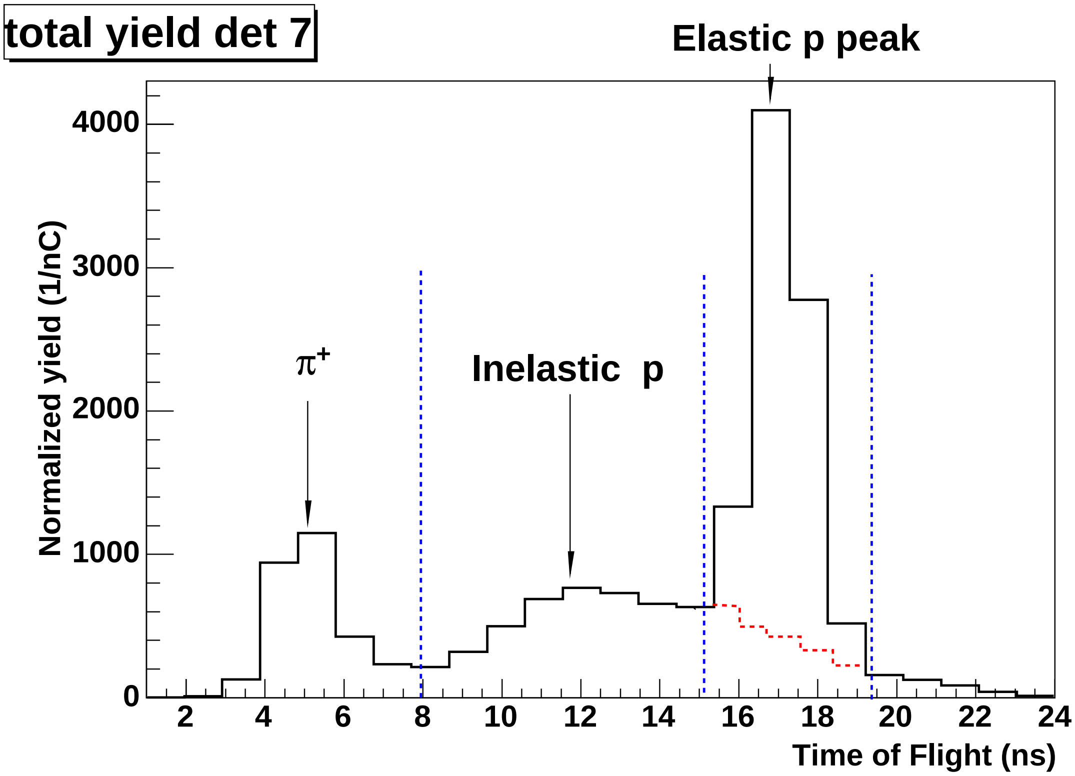

Figure 3-1: FPD 7 FR time of flight spectrum. The horizontal axis has been rebinned in 1 ns bins and restricted to 24 bins. The histogram displays the normalized yield data summed over the whole data sample. The dashed line that extends under the elastic peak is an impression on how the background might extend under the elastic peak, it does not come from measurement or from simulation.

proportional to the differential elastic cross-section, $d\sigma_{ep}$, and so eq. (1.15) becomes the definition of the measured parity-violating asymmetry in one quartet, which is given by

$$A = \frac{Y^+ - Y^-}{Y^+ + Y^-} = \frac{Y_1^+ + Y_2^+ - Y_1^- - Y_2^-}{Y_1^+ + Y_2^+ + Y_1^- - Y_2^-} \tag{3.2}$$

as there are two states of positive helicity and two states of negative helicity in a quartet, and $+, -$ superscripts are indexing positive and negative helicity states respectively, and

---

[*] In what follows the MPS index will not be carried explicitly – a detailed treatment of the asymmetry definition and summation is found in addendum A – and unless otherwise specified normalized yield will refer to normalized yield over the elastic peak.

$Y_{1,2}^{+,-}$ are the normalized yields summed over the bins in the elastic peak for the respective MPS. The raw data are accumulated for about one hour and forms a run. For each quartet in a run asymmetries are formed for individual timebins and for various predefined cuts of the ToF of an FPD segment (the elastic peak is one of them) using eq. (3.2). In general, as observed in the experiment, the elastic peak spreads over about 4 ns. The quartet asymmetries over a run are histogrammed weightless and for each FPD segment a mean elastic asymmetry with its uncertainty is computed, A, σ_A (where the FPD index is omitted for clarity).

The asymmetry in the number of detected particles and the electron beam charge asymmetry over a quartet is defined as

$$A_p = \frac{N_p^+ - N_p^-}{N_p^+ + N_p^-} = \frac{\Delta N_p}{N_p}, \text{ and } A_Q = \frac{Q^+ - Q^-}{Q^+ + Q^-} = \frac{\Delta Q}{Q} \tag{3.3}$$

where $N_p^{+(-)} = N_{1p}^{+(-)} + N_{2p}^{+(-)}$ ($Q^{+(-)} = Q_1^{+(-)} + Q_2^{+(-)}$) is the sum of detected number of particles (charge) with the same helicity in the same quartet, and N_p (Q) is the total number of detected particles (total charge) in a quartet (the sum of all four helicity states). Using eq. (3.3) and the fact that the expected FPD asymmetries are small, of the order of a few ppm, eq. (3.2) becomes (note that $N_p^+ = N_p^- + \Delta N_p$ and $Q^+ = Q^- + \Delta Q$)

$$A = \frac{\frac{N_p^- + \Delta N_p}{Q^- + \Delta Q} - \frac{N_p^-}{Q^-}}{\frac{N_p^- + \Delta N_p}{Q^- + \Delta Q} + \frac{N_p^-}{Q^-}} = \frac{A_p - A_Q}{1 + A_p + A_Q} \approx A_p - A_Q \tag{3.4}$$

In the absence of charge asymmetry and electronics deadtime effects the measured asymmetry in cross sections, eq. (3.2), becomes the asymmetry in detected number of particles. In these conditions, the width of the distribution of a measured FPD asymmetry is given by the counting statistics width [79], and the experiment is said to obey counting statistics (N_p is the number of counts in a quartet, and N_q is the number of quartets in a run)

$$\Sigma_A = \Sigma_{A_p} \approx 1/\sqrt{N_p} = 1/\sqrt{Y \cdot Q} \tag{3.5}$$

where $\Sigma_A = \frac{\sigma_A}{\sqrt{N_q}}$. In reality the width of the measured asymmetry distribution is always bigger than counting statistics width, Σ_{A_p}, and so it is useful to define a quantity called counting statistics fraction, given by the ratio

$$csf = \frac{\Sigma_{A_p}}{\Sigma_A} = \frac{1}{\Sigma_A \sqrt{N_p}} \tag{3.6}$$

which varies around unity if the counting measurement is dominated by statistics (see sections 3.2.3 and A for discussions about systematic effects that make csf deviate from 1). A detailed treatment of the FPD asymmetry summation over timebins and over quartets is given in addendum A.

3.2.2 Data sets

The asymmetry data collection is described in section 2.8. The asymmetry data runs are replayed separately for the two halves of the G^0 FPD, the FR and the NA sections. The reminder of this chapter is concerned with the offline replay of the asymmetry data for the FR and NA FPDs from the first G^0 engineering run. A presentation of the analysis program as implemented for this data sample follows.

The accumulated asymmetry data is replayed with the G^0 offline replay engine. Some cuts are applied to the data at this level and summary results can be written to the G^0 database or stored in ROOT files. For the mass replay of the data the default option is writing to the database. Databases used for this data analysis are *gzero-eng* for the NA FPD and *gzero-eng-4threplay* for the FR FPD.

The cuts implemented in the replay of the data are related to the beam quality, helicity reporting and detector/electronics. The beam cuts implemented for the first engineering run are: the replay engine throws out events with beam intensities lower than 5 μA or higher than 51 μA. After a beam trip, the first 2000 MPSs during beam recovery are discarded. During the time of a beam recovery, the distribution of the normalized yield in a typical detector has non-gaussian tails as explained in section 2.4.2. A reevaluation of this cut for the second engineering run reduced its time length from 2000 MPSs or 66 s of data acquisition time, to 750 MPS or 25 s of data acquisition time. The helicity cut throws out MPSs for which there is an inconsistency with the helicity reporting scheme. The cut checks the reported helicity, which is delayed by 8 MPSs, against the algorithm for predicting it. The detector/electronics cuts are checks of consistency in the detection chain (*e.g.* when electronics get stuck) and are implemented on events that have passed the beam and helicity cuts.

If an MPS/event passes these cuts it is tagged as *"good"* and the normalized FPD yields for it are computed and histogrammed. If all four MPSs of a quartet pass the cuts the quartet is tagged as *"good"* and the quartet asymmetry gets computed and histogrammed. In this scheme the amount of good asymmetry data (or the number of good quartets) may vary slightly from FPD to FPD as the FPD/electronics cuts are implemented individually for each FPD segment.

A different kind of cut has been applied for the data retrieved from the database. Asymmetry runs were considered good if the average charge asymmetry at the end of the run was less than 25 ppm and the average helicity correlated beam position differences in both x and y at the end of the run were less than 150 nm. The reason for this cut lies in the sometime poor performance of the beam feedbacks responsible for controlling the parity quality of the G^0 beam (see more about this in section 2.6.2).

A variety of options (or flags) are available for the offline replay engine for replaying the raw data. A single replay process of the whole data is called pass. To extract FPD asymmetries from the raw data at least one pass is necessary. In the default implementation of the first pass replay the asymmetry data are cleaned of bad events, are corrected for detection deadtime and averaged normalized yield slopes versus six beam parameters (charge, energy, x and y position, and θ_x and θ_y angles at the target) are computed on a run by run basis and stored. Using the normalized yield slopes from the first pass replay a second pass replay can be performed to linearly regress the asymmetry data with respect to the six beam parameters mentioned, also on a run by run basis. In this implementation the linear regression is done on the FPDs' yield on an MPS by MPS basis and the FPD asymmetries are recomputed using the corrected normalized elastic yields. For the data analyzed here the linear regression has been implemented by averaging the normalized yield slopes over the data sample as it will be described in section 3.2.5.

After detection deadtime correction and beam induced false asymmetries correction the FPD asymmetry data are corrected for background under the elastic peak for each individual FPD for background dilution and interpolated background asymmetry. A final correction to the FPD asymmetry data is applied due to the less than 1 electron beam longitudinal polarization. The total asymmetry and its uncertainty for a FPD segment is computed by summing the corresponding FR and NA asymmetries and their uncertainties as statistically independent measurements. Separately, using a simulation package based on GEANT 3, the 4-momentum transfer, Q^2, is determined for each FPD. The electron beam energy loss and electromagnetic external radiative corrections in the target are taken into account in the simulation package. Finally, from the asymmetry dependence on the 4-momentum transfer, $A(Q^2)$, the combinations of vector strange form factors $G_E^s(Q^2) + \alpha(\theta_e, Q^2)\cdot G_M^s(Q^2)$ could be extracted, where $\alpha = (\tau(Q^2)G_{Mp}^{\gamma}(Q^2))/(\epsilon(\theta_e, Q^2)G_{Ep}^{\gamma}(Q^2))$ is a smooth function of the electron scattering angle, θ_e, and the 4-momentum transfer in the elastic $e-p$ reaction. The elastic asymmetry error budget per FPD is presented at the end after all the asymmetry corrections described above are performed.

3.2.3 Asymmetry tests

Before performing corrections on the elastic proton peak asymmetry, which will be called the elastic asymmetry from now on, the measured elastic asymmetry is tested for its overall statistical behavior, for its statistical behavior over time, and for its parity-violating nature.

Statistical behavior

The elastic asymmetries quoted at the end of each run are histogrammed over the number of runs for each detector. The weight of an individual run elastic asymmetry in this histogram is its inverse square uncertainty, $w_i = \sigma_{A_i}^{-2}$ (i being the run index). The sign is reversed for the elastic asymmetries from runs with the IHWP = IN state before histogramming, and it is left intact for elastic asymmetries from runs with the IHWP = OUT. The histograms for individual detectors from each half of the G^0 detector, separately for FR and NA respectively, are then fitted with gaussian probability distribution functions (p.d.f.) [5]

$$f_G(x|\mu,\Sigma) = \frac{I}{\sqrt{2\pi}\Sigma} \cdot exp\Big[-\Big(\frac{x-\mu}{\sqrt{2}\Sigma}\Big)^2\Big] \tag{3.7}$$

where I is the integral of the histogram and μ and Σ are the mean and the width of the distribution. The integral of the distribution is given by (j is the bin index)

$$I = \sum_{j=1}^{N_{bin}} W_j \tag{3.8}$$

where W$_j$ is the content of bin j, and N$_{bin}$ is the number of bins in the histogram.

The χ^2 for *goodness-of-fit* for the gaussian fit of the asymmetry histograms per detector can be determined with [5]

$$\chi^2 = \sum_{j=1}^{N_{bin}} \frac{[W_j - f_G(x_j)]^2}{f_G(x_j)} \tag{3.9}$$

where x_j is bin j. The χ^2 is computed by the ROOT fitting routine along with the p-value for goodness-of-fit, which is the probability that a data sample for the p.d.f. f_G yields a χ^2 greater than the one determined for this data sample

$$p = \int_{\chi^2}^{\infty} f_{\chi^2}(z|n_d)dz \tag{3.10}$$

where $f_{\chi^2}(z)$ is the p.d.f. for χ^2, and n_d is the number of degrees of freedom (for a gaussian $n_d = N_{bin} - 3$).

Fig. (3-2) and fig. (3-3) show the fitting results for the FR and NA detectors respectively.

The table 3.1 summarizes the fitting parameters for figs. (3-2) and (3-3): The two sides of the G^0 FPD, FR and NA, can be considered as statistically independent. Based on this test it appears that both of them behave well statistically with none of them conspicuously worse than the other. This result validates the computation of a total elastic asymmetry for an FPD ring, as the sum of statistically independent elastic asymmetry averages over the data from the two sides of the G^0 FPD, the FR and NA.

Time behavior

The individual FPD elastic asymmetries and their widths per run can be plotted versus run number to look at the their explicit time behavior. This is another way of looking at the gaussian nature, eq. (3.7), of the elastic asymmetry distribution per FPD. The run by run behavior of the csf, eq. (3.6), are also displayed in figs. (3-4,3-5). Only two FPD segments are plotted from each half of the G^0 FPD, 4 and 12, but the time behavior

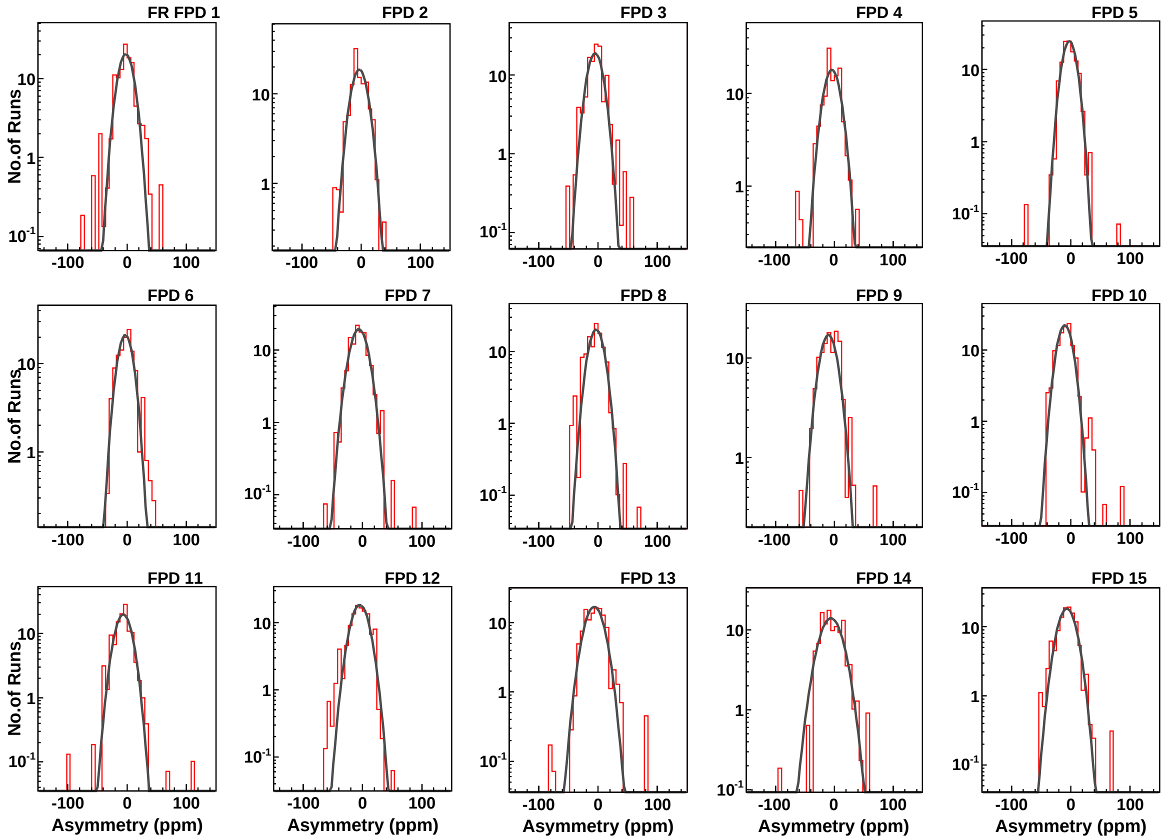

Figure 3-2: FR Detector: raw run elastic asymmetries histogrammed for each detector and fitted with a gaussian function f_G, eq. (3.7).

is in the same limits for all the FPDs, with no one FPD segment being substantially different from the others (this is expected for the elastic asymmetry, since all the FPDs asymmetry data behaves like gaussian distributions as seen in the previous section, but it is not necessarily expected from the elastic asymmetry widths and the elastic peak counting statistics fraction). The asymmetry data runs were not all at the same beam current, so the asymmetry widths were adjusted before plotting to be compared with the elastic asymmetry widths produced by the nominal 40 μA beam (it is assumed that the asymmetry width varies like $1/\sqrt{I}$, where I is the beam current). The plots also show asymmetry runs of different time lengths. There was no cut on the extension of a run to eliminate runs from the analysis based on data acquisition time. Most of the FR and

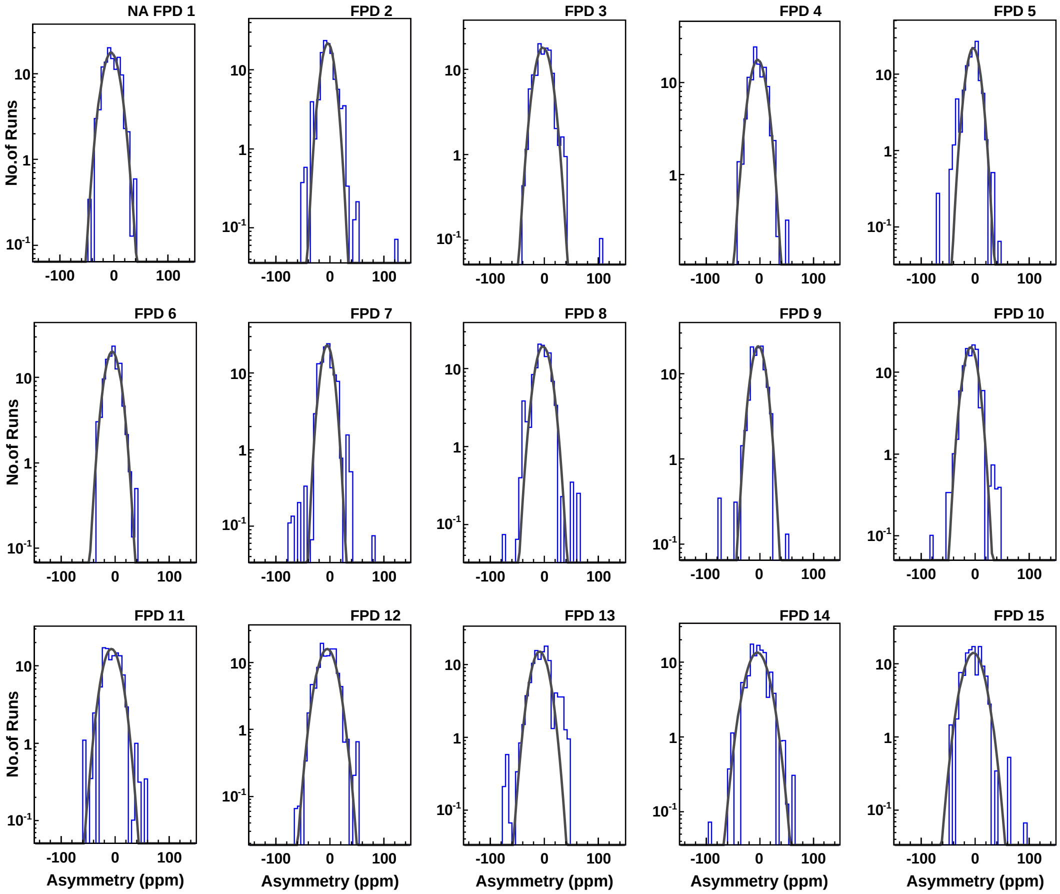

Figure 3-3: NA Detector: raw run elastic asymmetries histogrammed for each detector and fitted with gaussian function f_G, eq. (3.7).

NA elastic asymmetry widths lie within 10% of the average over the entire data sample, with one run for FR and one run for NA that has the corresponding elastic asymmetry width 20% off above the average. The same regular behavior is displayed by the counting statistics fractions for all the FR and NA FPD segments.

A summary plot with χ^2 and p-values for fits with constants (averaging) applied to the elastic asymmetries versus time (run number) for all FPD segments is shown in fig. (3-6): The elastic asymmetries behave well in time for both FR and NA FPDs respectively. The normalized χ^2's for fits with constants for these distributions is between 0.8 and 1.4 for FR and between 0.8 and 1.3 for NA, with no FPD segments having their

Table 3.1: Elastic asymmetries histogrammed and fitted with gaussian functions, separately for FR and NA detectors. The mean μ and its error σ_μ below are the values from the gaussian fit.

Det	FR				NA			
	$\mu \pm \sigma_\mu$(ppm)	χ^2	n_d	p	$\mu \pm \sigma_\mu$(ppm)	χ^2	n_d	p
1	-2.46±1.17	13.7	15	0.54	-5.28±1.45	7.7	11	0.73
2	-3.03±1.39	13.1	11	0.28	-3.98±1.28	12.8	14	0.54
3	-5.11±1.23	19.6	14	0.14	-2.79±1.36	8.5	12	0.74
4	-4.22±1.43	15.1	11	0.18	-4.18±1.39	8.5	11	0.67
5	-2.31±1.07	5.5	11	0.90	-3.62±1.12	10.3	12	0.58
6	-2.9±1.17	11.2	11	0.42	-5.41±1.27	4.5	10	0.92
7	-6.18±1.29	5.4	14	0.98	-5.16±1.24	13.9	14	0.45
8	-3.25±1.16	16.1	13	0.24	-2.68±1.29	8.3	14	0.87
9	-10.08±1.58	15.0	12	0.24	-2.84±1.24	5.7	10	0.84
10	-9.94±1.29	8.4	13	0.82	-8.38±1.22	10.8	14	0.69
11	-6.3±1.23	11.6	14	0.63	-6.9±1.67	11.3	13	0.58
12	-4.67±1.39	9.7	15	0.84	-5.13±1.56	9.8	15	0.83
13	-6.54±1.45	11.4	15	0.72	-8.75±1.51	20.3	17	0.26
14	-5.98±1.93	11.2	14	0.67	-4.88±2.04	12.9	15	0.61

corresponding elastic asymmetry uncertainty either overestimated (too good χ^2 values) or underestimated (too bad χ^2 values). These fits yield the average elastic asymmetry and its uncertainty over time.

Summary plots with averaged elastic asymmetry widths over the number of asymmetry runs and averaged counting statistics fractions per FPD are shown in fig. (3-7). Averages were made as for statistically independent measurements, eq. (3.8). The averaged elastic asymmetry widths for FR and NA FPD segments follow each other and are at most about 1% apart from each other. The highest counting statistics rings are 2 and 3 with about 1650 ppm and the lowest are rings 13 and 14 with 2300 and 2350 ppm respectively. The counting statistics fractions are for all FR and NA FPD segments above 0.92. The csfs were computed after the detection deadtime corrections were applied to the data. The deadtime correction induces noise into the asymmetry distribution [66]

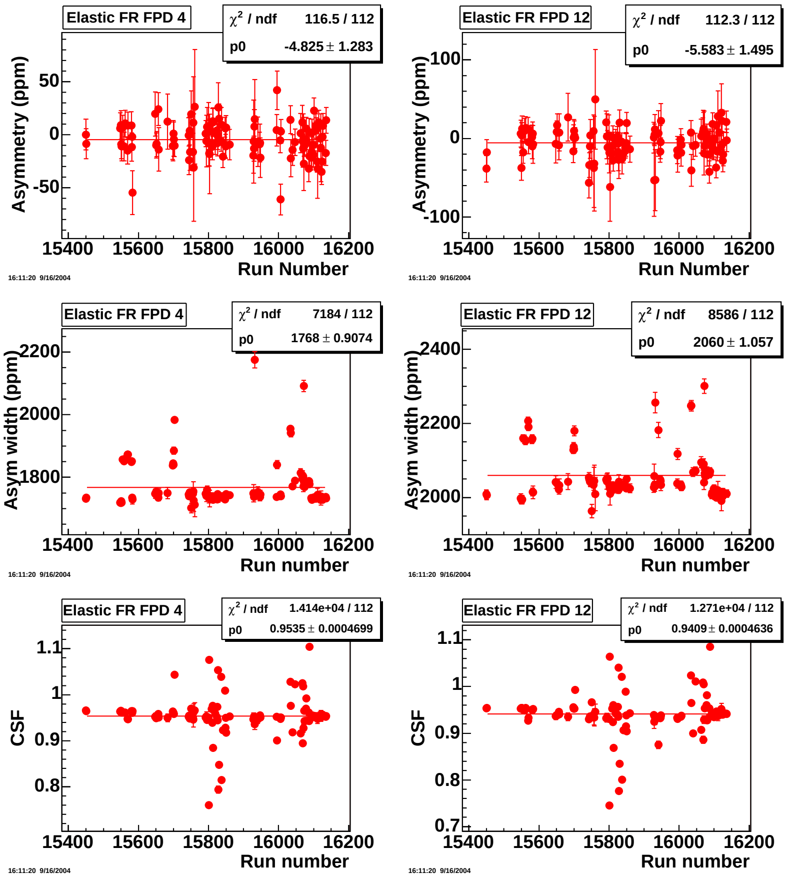

Figure 3-4: FR FPDs 4 and 12: first row of plots from top displays raw run elastic asymmetries versus run number, second row displays elastic asymmetry widths versus run number and the third row displays the counting statistics fraction for the elastic peak (defined by eq. (3.6)) versus run number.

reflected in an enlargement of the width of the distribution by a factor of $\sim \sqrt{1+f}$, where f is the deadtime fraction. The deadtime fraction for the G^0 FPDs is about 10-15%, which accounts for about a 5-7% correction to the elastic asymmetry width. The liquid hydrogen target also induces noise into the asymmetry width at most at a level of 240 ppm (see the addendum B on this), which accounts for about 1% correction to the elastic asymmetry width. With the deadtime correction and target noise sources taken into account the csfs on the elastic proton peaks are all within 2-3% of 1. In the

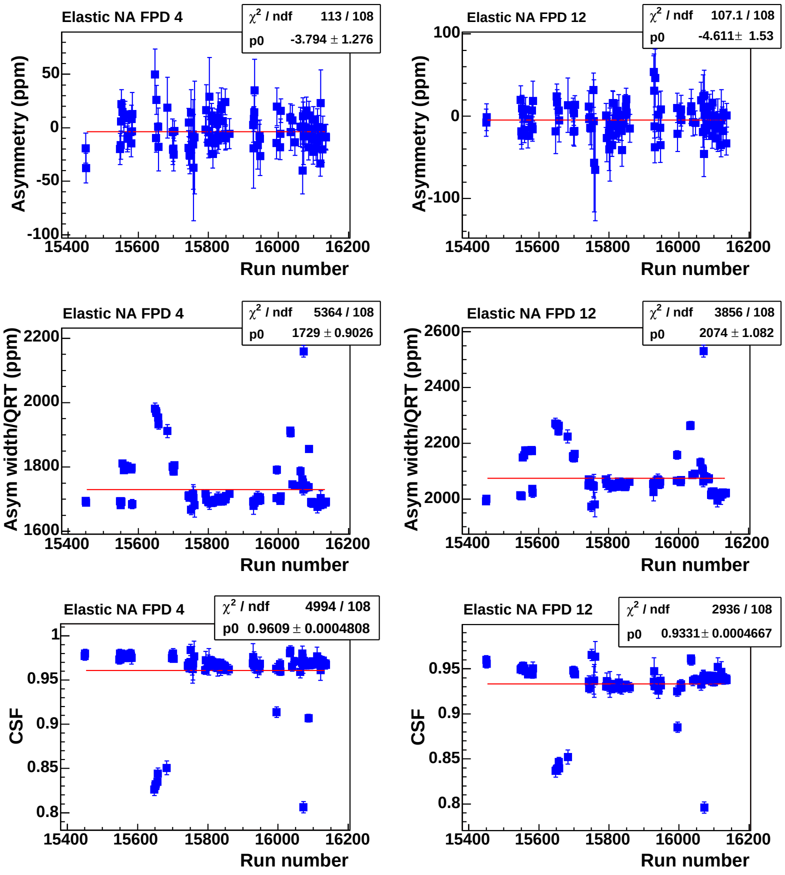

Figure 3-5: FR FPDs 4 and 12: first row of plots from top displays raw run elastic asymmetries versus run number, second row displays elastic asymmetry widths versus run number and the third row displays the counting statistics fraction for the elastic peak (defined by eq. (3.6)) versus run number.

simulation presented in the addendum A on detection timing instabilities, for the case of a measurement dominated by statistics, fluctuations of the csf for a peak were seen at a level of a few percent over a time scale of 10^4 quartets (0.5 h of data acquisition).

In conclusion there is not any significant source of noise that reflects on the elastic asymmetry widths at 30 Hz. The data analyzed here are statistically distributed as expected from counting statistics within 4%.

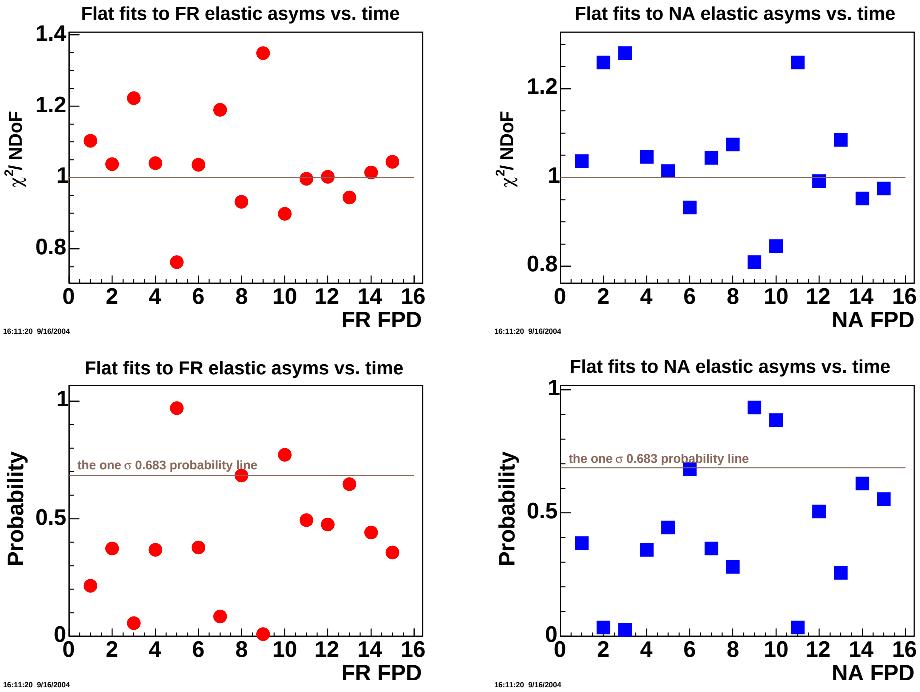

Figure 3-6: FR and NA FPD: χ^2 and p-values for fits with constants to the plots of elastic asymmetries versus run number (time).

Geometric behavior

One source of false asymmetries could be a component of transverse polarization in addition to the longitudinal polarization of the electron beam. The transverse polarization of the electrons can be the source of a parity conserving asymmetry that varies with the azimuthal angle measured from the transverse polarization vector's direction. Following the conventions of [61], the expression for the transverse polarization induced asymmetry is

$$A(\phi) = A_T sin(\phi + \delta) \tag{3.11}$$

where ϕ is the azimuthal angle, δ is a phase factor and A_T is the Mott asymmetry for transversely polarized electron scattering [60]. Elastic asymmetries summed over the whole data, separately for individual octants can be seen in fig. (3-8). The figure shows

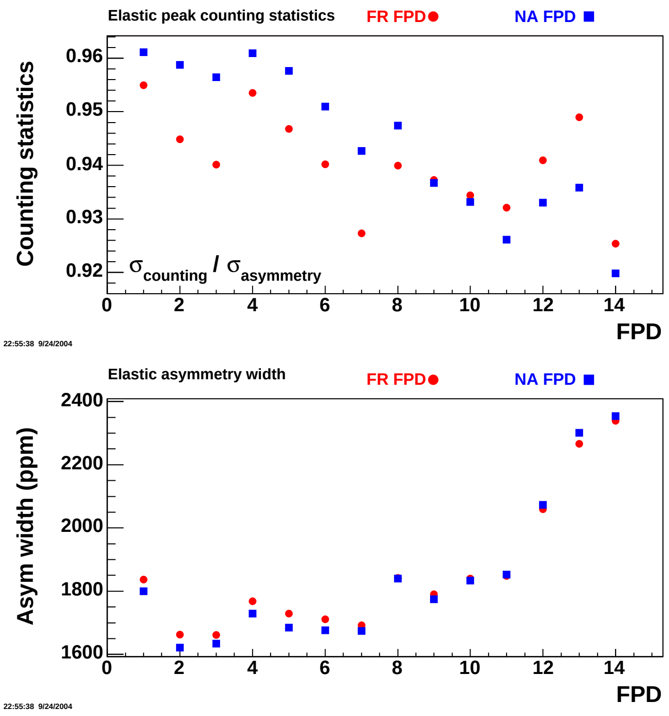

Figure 3-7: FR and NA FPDs: elastic asymmetry widths and counting statistics fractions averaged over the number of runs for each FPD segment.

a sample of four FPD segments (1, 5, 9 and 13), distributed along the focal surface of the G^0 magnet. Within the statistical uncertainties for the elastic asymmetries versus octant angle there is no apparent ϕ dependence of the measured asymmetries, suggesting that there is no significant transverse polarization contamination for the electron beam. No correction to the measured elastic asymmetries has been done due to a transverse polarization component of the electron beam for this data sample.

Parity-violating nature

The insertable half wavelength (IHWP) device has been described in section 2.6.1. The data are divided into two sets according to the states of the IHWP, IN and OUT. If the elastic asymmetry doesn't change sign with the IHWP state then the asymmetry

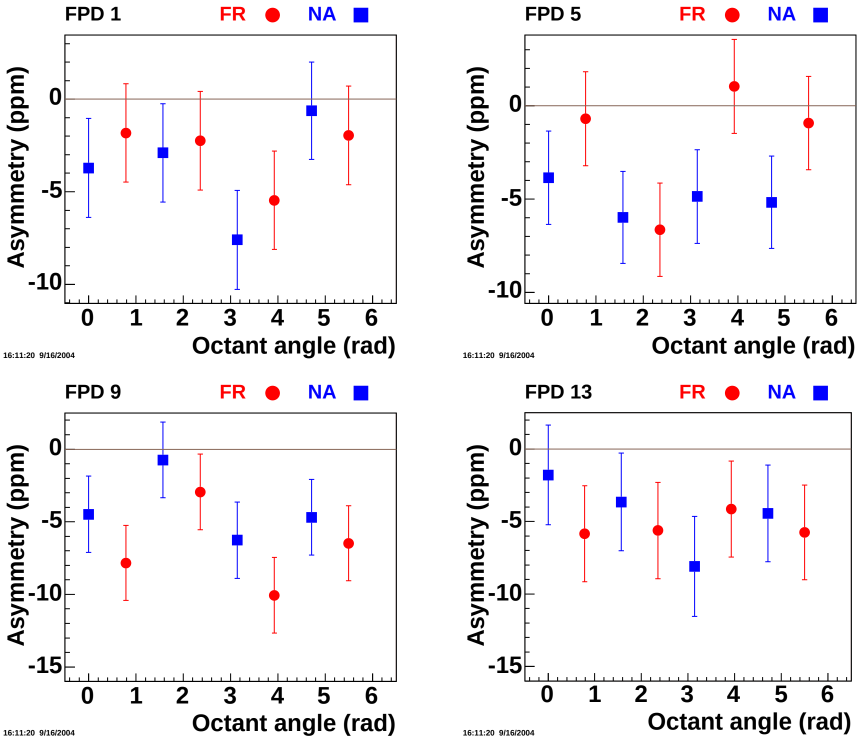

Figure 3-8: FPDs 1, 5, 9 and 13, both FR and NA: elastic asymmetries, averaged over all data, versus octant angle.

is not caused by a parity violation mechanism but rather by systematic effects in the experimental apparatus. An important *null asymmetry* test is used to check the quality of the data by summing the corresponding asymmetries for the two IHWP states with no sign change. For one FPD and one state of the IHWP the asymmetries are summed as statistically independent measurements of the same gaussian distributed quantity

$$A_{j,IHWP} = \frac{\sum_{i=1}^{N_{IHWP}} \frac{A_{ji}}{\sigma_{ji}^2}}{\frac{1}{\sigma_{j,IHWP}^2}}, \text{ and } \frac{1}{\sigma_{j,IHWP}^2} = \sum_{i=1}^{N_{IHWP}} \frac{1}{\sigma_{ji}} \tag{3.12}$$

where IHWP $=$ OUT(IN), N_{IHWP} is the respective number of runs for that state of the IHWP and A_{ji}, σ_{ji} are the average asymmetry and its error at the end of the run i for detector j. For parity violating asymmetries the IHWP changes the sign of the centroid of a statistical distribution but not the probability distribution or the shape of the statistical distribution. In this case by changing the sign to the asymmetries from IHWP = IN they should belong to the statistical distribution for asymmetries in the IHWP = OUT state, and this is how the total asymmetry is computed for a detector segment j, using eq. (3.12)

$$A_j = \frac{\frac{A_{j,OUT}}{\sigma^2_{j,OUT}} - \frac{A_{j,IN}}{\sigma^2_{j,IN}}}{\frac{1}{\sigma^2_{j,OUT}} + \frac{1}{\sigma^2_{j,IN}}}, \text{ and its error } \frac{1}{\sigma^2_j} = \frac{1}{\sigma^2_{j,OUT}} + \frac{1}{\sigma^2_{j,IN}} \tag{3.13}$$

where j is the index for the detector segments.

In the case of the null asymmetry test, summing the asymmetries from the two IHWP states with no sign change for IHWP = IN, makes for summing data samples from two different statistical distributions

$$A_{j,NULL} = A_{j,OUT} + A_{j,IN} \text{ and } \sigma^2_{j,NULL} = \sigma^2_{j,IN} + \sigma^2_{j,OUT} \tag{3.14}$$

The results for the summations with eqs. (3.12, 3.14) are shown in fig(3-9) There is a net sign change between the two states of the IHWP for both NA and FR FPDs which provides strong evidence that the elastic asymmetries measured in this data sample are parity-violating in nature. Most of the sums of the null asymmetries are within 1σ from zero with only FPD segment 13 having both the FR and the NA more than 1σ from zero. The null sums averaged over the whole FPD segments are within 1σ from zero for both the FR and NA FPDs. These tests confirm the parity-violating nature of the elastic asymmetries in all the FPD segments. The average null asymmetry for each of the FR and NA FPDs is less than 0.7 ppm and as a systematic effect is much smaller than the background corrections for each FPD segment as it will be seen latter.

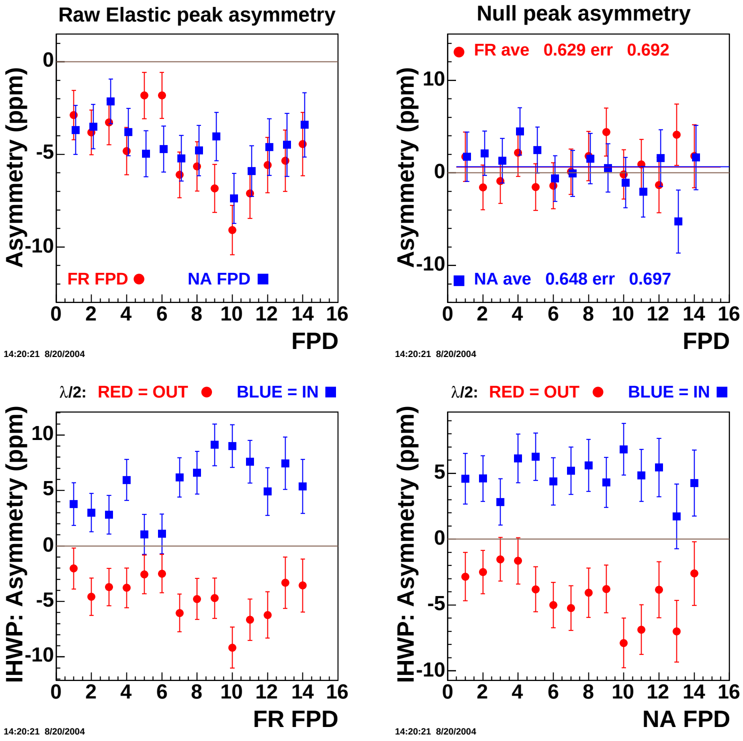

Figure 3-9: G^0 FPD: First row has raw elastic asymmetries and the null asymmetry plot. Second row has the elastic asymmetries for FR and NA FPDs versus IHWP.

3.2.4 Deadtime effects

In this section the influence of detection deadtime on the elastic asymmetry will be analyzed and an upper limit on the false asymmetry generated by these effects will be placed.

The notation of eqs. (3.3, 3.4) will be kept in what follows. The measured quartet asymmetry is then

$$A_m \approx A_p - A_Q \tag{3.15}$$

where A_p and A_Q are the respective asymmetries in the number of particles detected and in the number of electrons in the beam over the period of a quartet. The detection deadtime has the effect of reducing the real rate of particles detected in a given period of time due to the detector/electronics unresponsiveness after an event is detected for a certain time interval called the deadtime period τ. If the measured detection rate is N$_p$ then the deadtime fraction is $f = \tau{\cdot}N_p$. The deadtime fraction varies with the beam current. The detection rate is corrected for deadtime with

$$N_{p,corr} = \frac{N_p}{1-f} = \frac{N_p}{1-\tau{\cdot}N_p} \tag{3.16}$$

The deadtime corrected detection rate is nonlinear in the measured rate. Applying eq. (3.16) to eq. (3.4) in order to relate the measured parity-violating asymmetry with the beam charge asymmetry yields

$$A_{corr} = \frac{\frac{N_p+\Delta N_p}{(N_Q+\Delta N_Q)(1-f^+)} - \frac{N_p}{N_Q(1-f^-)}}{\frac{N_p+\Delta N_p}{(N_Q+\Delta N_Q)(1-f^+)} + \frac{N_p}{N_Q(1-f^-)}} \tag{3.17}$$

which becomes, using the definitions for A$_p$ and A$_Q$ from eq. (3.3)

$$\begin{aligned} A_{corr} &= \frac{N_Q(N_p+\Delta N_p)(1-f^-) - N_p(N_Q+\Delta N_Q)(1-f^+)}{N_Q(N_p+\Delta N_p)(1-f^-) + N_p(N_Q+\Delta N_Q)(1-f^+)} & (3.18)\\ &= \frac{\frac{f^+-f^-}{2} + A_p(1-f^-) - A_Q(1-f^+)}{1-\frac{f^++f^-}{2} + A_p(1-f^-) + A_Q(1-f^+)} & (3.19) \end{aligned}$$

Making the notation $f^- = \tau N_p^- = \tau N_p = f$ and $f^+ = \tau N_p^+ = \tau(N_p{+}\Delta N_p) = f{+}\tau\Delta N_p = f + \tau 2 N_p A_p = f(1+2A_p)$, then $f^+ - f^- = 2fA_p$ and $f^+ + f^- = 2f(1+A_p)$ and eq. (3.19) becomes

$$A_{corr} = \frac{A_p - (1-f^+)A_Q}{1-f+(1-2f)A_p+(1-f^+)A_Q} \tag{3.20}$$

which becomes, neglecting products of asymmetries in the approximation of small asymmetries

$$(1-f)A_{corr} \approx A_p - (1-f^+)A_Q \approx A_p - (1-f)A_Q \tag{3.21}$$

Using the result of eq. (3.4), $A_m \approx A_p - A_Q$, eq. (3.21) becomes

$$A_m = (1 - f)A_{corr} - fA_Q \tag{3.22}$$

Eq. (3.22) is the base result for the eponymous effect that has come to be known as the Wells effect after the name of Steve Wells, the G^0 collaborator who discovered it. It relates the direct effect of the beam's charge asymmetry on the measured parity-violating asymmetry in this type of experiment. It is also a means of measuring the deadtime fraction for the detection system by plotting A_m versus A_Q and extracting the slope from the graph, which is just -f. To have a better precision on the measured deadtime fraction through this method large beam charge asymmetries are forcefully induced by applying extreme voltages (1, 5 and 9 V) to the IA cell (see section 2.6.1 on how the IA works). Special runs are taken in this configurations, fig. (3-10), and the slope of the measured FPD asymmetry versus beam charge asymmetry is extracted. Fig. (3-11) shows a summary of the slopes determined with Wells scans.

Although the nominal beam current for G^0 is 40 μA, these runs were taken at 30 μA because reaching 40 μA was attainable during the first engineering run, but keeping the beam current at 40 μA was a problem, and a Wells scan would take about 2-3 h of beam time at 40 μA The resulting detection deadtime fraction averages from this type of measurement are in good agreement with each other for both the FR and NA FPDs, in absolute value $f_{FR}(30\mu A) = 6.6 \pm 0.1\%$ and $f_{NA}(30\mu A) = 6.5 \pm 0.1\%$ within the error bars.

With the present implementation of the algorithms for detection deadtime correction in both halves FR and NA FPD/electronics, there is still a residual slope of the deadtime corrected normalized detector yield versus beam current. The residual slope accounts for a deadtime corrected normalized detector yield reduction of about 4% between low beam currents (5-10 μA) and the nominal beam current of 40 μA for both FR and NA FPDs.

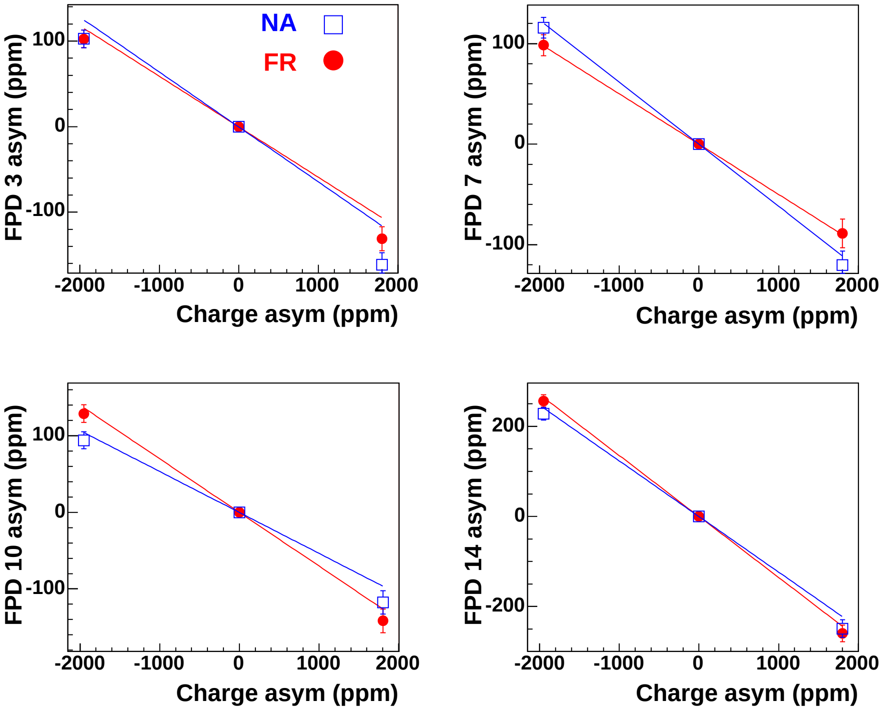

Figure 3-10: Wells plot at 30 μA beam current, FR and NA separated.

This reduction cannot be blamed entirely on the target global density reduction between low beam currents and nominal beam current (see the target section B.1.1). As seen in section B.1.1 the detector normalized yield reduction due to target density reduction is at most a 1.5% normalized detector yield reduction, as measured by the G^0 and a 0.4% reduction, as measured by the luminosity detectors.

The size of the false asymmetry due to detection deadtime effects in measuring the parity-violating asymmetry is given by eq. (3.22), and is

$$\delta A_{false}^{deadtime} = f \cdot A_Q \tag{3.23}$$

Although the detection deadtime correction algorithms for both FR and NA FPDs do not work perfectly and there is still a residual deadtime slope after the correction, due to the satisfactory work of the beam charge asymmetry feedback, which reduced the

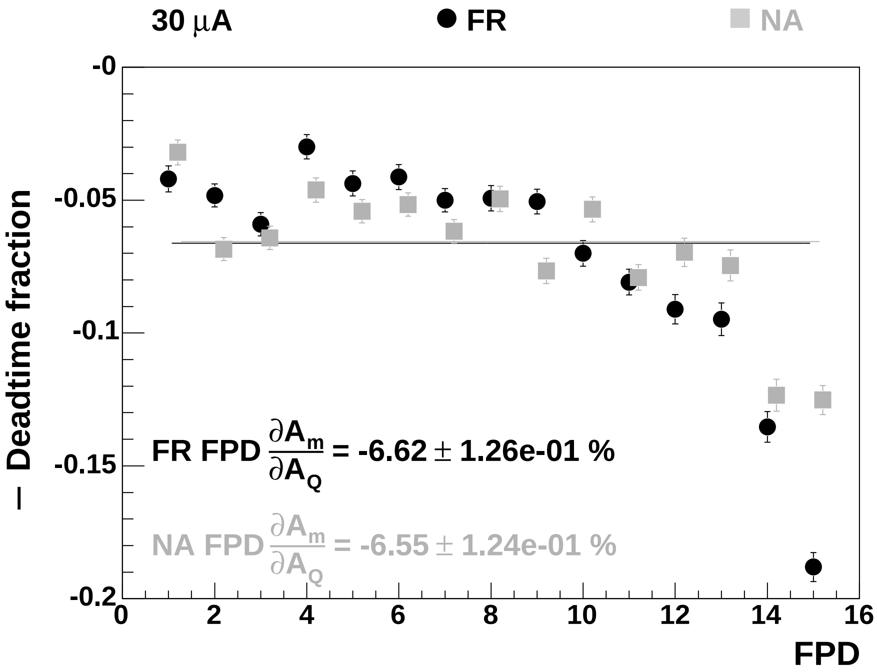

Figure 3-11: G^0 Detector deadtime: Summary Wells plot at 30 μA beam current. Individual points are the extracted slopes from individual detector segments for each sides of the detector, FR and NA, respectively.

beam charge asymmetry to about 1 ppm over the period of taking these data, see figs. (2-19,2-20) the upper limit of the false asymmetries caused by the residual deadtime is placed at

$$f_{residual} \approx 4\%, \text{ and } \delta A^{deadtime}_{false} \leq 0.04 ppm \tag{3.24}$$

which is a very small contribution and will be neglected in what follows.

3.2.5 Linear regression

A source of false asymmetries to the measured parity-violating G^0 asymmetries may come from the helicity correlated electron beam parameter variations. During the period of a data taking run beam parameters vary around mean values and the instantaneous values they take may influence the number of particles scattered into the detector at that instance in time. It is the helicity correlated beam parameters variations that are of interest for asymmetry measurement as these variations are systematic effects on the parity-violating asymmetry measurement. There are six beam parameters considered here for their systematic effects on the elastic asymmetry: four geometric degrees of freedom that completely describe the beam position on target, the beam charge asymmetry and the beam energy.

The beam position on target can be determined completely with four parameters, in general either four different spatial coordinates or two different spatial coordinates and two different spatial angles. In this experiment the electron beam position on target is expressed with two coordinates and two angles. The coordinates are along two perpendicular axes, x and y, and the angles are measured along these axes, θ_x and θ_y. The G^0 coordinate system is with the z axis along the beam pointing the positive direction in the direction of motion of the electrons, the y axis being in the vertical plane with the positive direction pointing to beam-up, and the x axis is in the bending plane of the beam with the positive sense pointing to beam-right.

The main contribution to the detected normalized yield in a FPD segment comes from the scattering processes in the target. It is assumed that the electron beam parameters influence the normalized yield in a typical FPD segment linearly in the first approximation (k is the MPS index)

$$Y_{k,m} = Y_{k,corr} + \sum_{i=1}^{6} \alpha_i \Delta x_{k,i} \tag{3.25}$$

where $Y_{k,m}$ is the measured normalized FPD yield in MPS k, $Y_{k,corr}$ is the corrected for beam effects normalized FPD yield (the part of the measured normalized yield that is independent of beam influences), i is the index for beam parameter x_i, $\alpha_i = \partial Y / \partial x_i$ is the slope of the normalized FPD yield versus beam parameter i and $\Delta x_{ki} = x_{ki} - \bar{x}_i$ is the beam parameter x_i deviation for MPS k from its average over a run, $\bar{x}_i$.

At a quartet level, the corrected asymmetry for beam parameter influences is (j

is the quartet index, superscript +/− signify helicity states, and subscript m signifies *measured*)

$$\begin{aligned}
A_{j,corr} &= \frac{Y^+_{j,corr} - Y^-_{j,corr}}{Y^+_{j,corr} + Y^-_{j,corr}} && (3.26)\\
&= \frac{Y^+_{j,m} - Y^-_{j,m} - \sum_i \alpha_i (x^+_{ij} - x^-_{ij})}{Y^+_{j,m} + Y^-_{j,m} + \sum_i \alpha_i (x^+_{ij} + x^-_{ij} - 2\bar{x}_i)} && (3.27)\\
&= A_{j,m} \frac{1 - \sum_i \alpha_i \frac{x^+_{ij} - x^-_{ij}}{\Delta Y_{j,m}}}{1 + \sum_i \alpha_i \frac{x^+_{ij} + x^-_{ij} - 2\bar{x}_i}{2Y_{j,m}}} && (3.28)\\
&= A_{j,m} - \sum_i \frac{\alpha_i (x^+_{ij} - x^-_{ij})}{2Y_{j,m}} && (3.29)
\end{aligned}$$

where the sum over i runs over the number of beam parameters, six, and terms of the order beam parameters differences from their averages divided by normalized FPD yield have been neglected. Noting $x^+_{ij} - x^-_{ij} = \delta x_{ij}$ and averaging the corrected FPD segment asymmetry, eq. (3.29) per quartet over a run yields

$$A_{corr} = A_m - \delta A_{beam}, \text{ where } \delta A_{beam} = \sum_{i=1}^{6} (\bar{\alpha}_i / 2Y_m) \cdot \bar{\delta x}_i = \sum_{i=1}^{6} \bar{\alpha}'_i \cdot \bar{\delta x}_i \qquad (3.30)$$

The uncertainty for A$_{corr}$ is given by

$$\Delta^2 A_{corr} = \Delta^2 A_m + \Delta^2 \delta A_{beam} \qquad (3.31)$$

The uncertainty for δA_{beam} is given by

$$\Delta^2(\delta A_{beam}) = \sum_i (\bar{\alpha}'_i \bar{\delta x}_i)^2 \Big[\Big(\frac{\Delta\alpha'_i}{\alpha'_i}\Big)^2 + \Big(\frac{\Delta\delta x_i}{\delta x_i}\Big)^2\Big] \qquad (3.32)$$

The size of the false asymmetries to the measured parity-violating asymmetry due to the helicity correlated beam parameters differences is given by δA_{beam}. As seen in eq. (3.30)

$\bar{\delta x_i}$ is the average helicity correlated beam parameter x_i differences over a run or over a range of runs. Although a slope is defined as $\alpha_i \equiv \partial Y/\partial x_i$, it is customary sometime to refer to the quantity $\alpha'_i \equiv \alpha_i/2Y = \partial Y/(2Y\partial x_i)$ as the slope of the normalized yield versus beam parameter x_i, and this convention will be adopted from now on. This latter quantity, α'_i, is usually expressed in units [%/(beam parameter's unit)] and it reflects the sensitivity of the detector to the respective beam parameter.

The G^0 beam is delivered rastered to the target (see section B.1). The frequency of the raster system is about 25 kHz, much higher than the frequency of the helicity change, 30 Hz. Due to this a beam parameter for a helicity state is the average measured by the respective beam monitor for that helicity state. The beam position is the position of the rastered beam on the target.

The parity-violating asymmetry measured in this experiment can be corrected for helicity correlated beam parameter differences either by doing the corrections on the yield, using eq. (3.25), or by doing the corrections on the asymmetry, using eq. (3.30). The corrections on the yield are done through a multiple parameter linear regression. To do the corrections through either method, determination of the yield slopes versus beam parameters (the α'_i, $i = \overline{1,6}$) is needed. The slopes can be determined from the data acquisition runs for each run individually. During the time period of a run the beam parameters fluctuate around their averages and induce changes in the measured normalized FPD yields. The deviation of a FPD yield in MPS k from its average for a run can be expressed as

$$Y_k - \bar{Y} = \sum_i (\partial Y/\partial x_i)\cdot(x_{ki} - \bar{x_i}) = \sum_i \alpha_i \cdot dx_{ki} \tag{3.33}$$

Multiplying both sides of eq. (3.33) with the deviation dx_{kj} of beam parameter j during the same MPS, k, and averaging over the entire run (over the number of MPS's in the run) yields

$$\overline{(Y-\bar{Y})(x_j-\bar{x_j})} = \sum_i \alpha_i \overline{(x_i-\bar{x_i})(x_j-\bar{x_j})} \tag{3.34}$$

which represents a system of six linear equations in the unknowns $\alpha_i, i = \overline{1,6}$. The mixed products in the eq. (3.34) are the correlation coefficients between yield and x$_j$ on the left hand side of the equation and between beam parameters x$_i$ and x$_j$ on the right hand side. Computing the correlation coefficients from data for a run and inverting the system of linear equations in (3.34) yields the α_i, $i = \overline{1,6}$. Then corrections to the yield can be done on an MPS by MPS basis using eq. (3.25). This correction procedure is a two step process. In a first step the asymmetry data runs are replayed and the normalized detector yield slopes (the α_i, $i = \overline{1,6}$) are determined with eq. (3.34) and stored in the database, in a subsequent step the corrections are applied to the normalized yield through eq. (3.25).

Another way of correcting the asymmetry data for helicity correlated beam parameter differences is through eq. (3.29). This procedure requires also a first pass replay to determine the yield slopes (the α_i', $i = \overline{1,6}$ this time) with eq. (3.34) and then the false asymmetries, δA_{beam}, can be computed and the measured asymmetries can be corrected directly using eq. (3.30). The plots in fig. (3-12) are representative for the G^0 FPD. As can be seen in fig. (3-12), the slopes determined (by slope here it is meant the $\alpha's$) on a run by run basis, histogrammed with weights representing their uncertainties are not gaussian distributed. Slopes versus run number (over time) show changes of sign in time with no apparent difference with the change in the state of the IHWP. This may mean that it is not the state of the IHWP that drives these changes in the detector's sensitivities over time. When the yield slopes versus beam position are averaged over the whole data sample (the whole number of runs), the expected behavior is seen versus octant angle (a harmonic variation is expected: for the slope versus beam position x, the slope should vary like $sin(\phi)$, with ϕ the angle measured from y axis - octant 1 has $\phi = 0$,

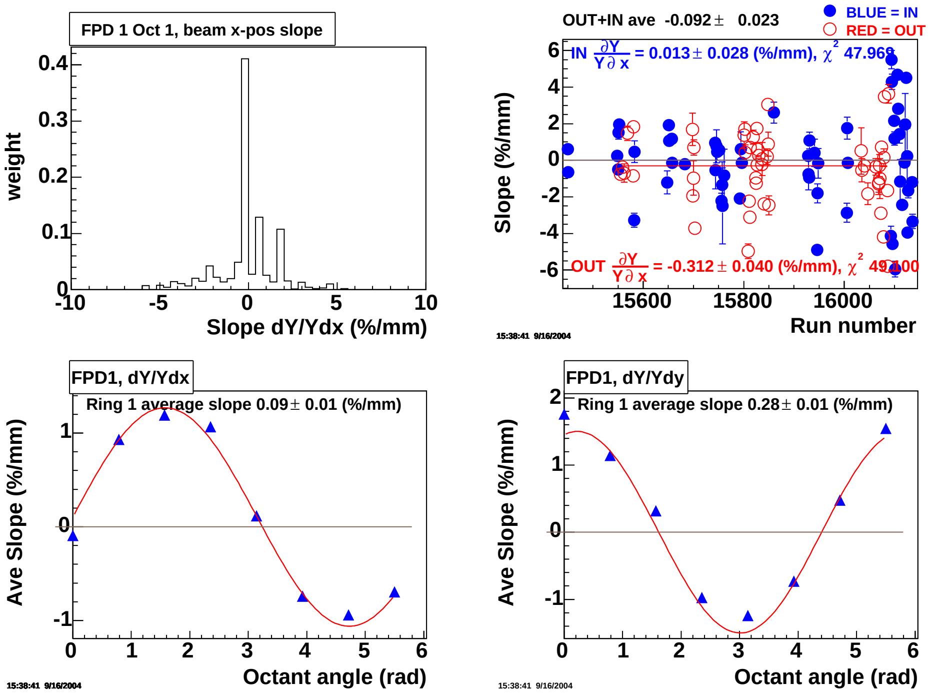

Figure 3-12: Detector 1 normalized yield slopes versus beam position x and y. The upper row of plots shows a histogram of the yield slope (α'_x) versus beam position x and the behavior of this slope versus run number (or over time). In the histogram the slopes have been weighted by their uncertainty. The lower row of plots show the geometric behavior of the average slopes over the whole data sample versus beam position x and beam position y at the target.

for the slope versus beam position y the *sine* function should have a $\pi/2$ phase change - and this is exactly what's been observed, see fig. (3-12)). It is because of this run by run behavior of the slopes that a run by run correction procedure based on the linear regression on the yield, eqs. (refeq:linreg3, 3.25), is not applied on this data sample.

The measured parity-violating asymmetries, for the data sample analyzed here, have been corrected for helicity correlated beam parameters differences using the second method eq. (3.30), by applying the corrections directly on the asymmetry. The yield slopes were determined on a first pass replay of the data, as described above. The corrections to the measured elastic asymmetries have been applied according to eq. (3.30) for each FPD segment in each octant for each IHWP separately, before summing over a ring for FR/NA and over the IHWP states. The size of the false asymmetry, δA_{beam}, is

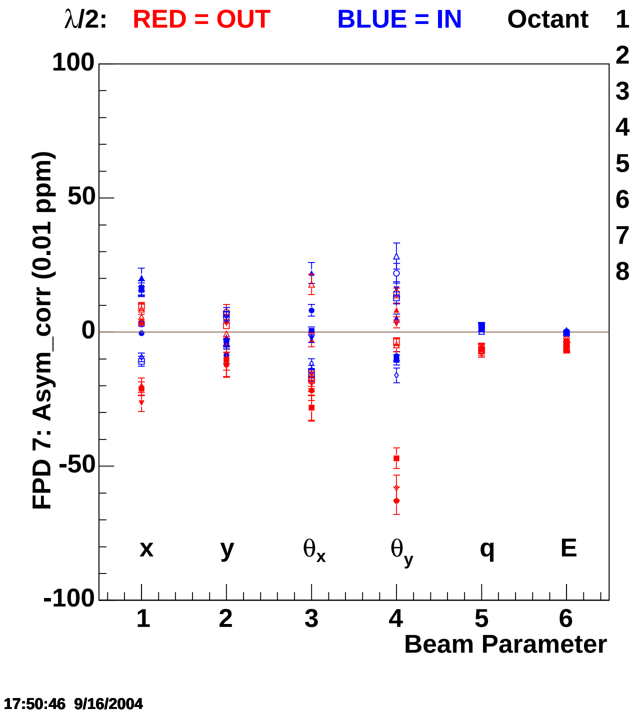

Figure 3-13: FPD 7: the size of the false asymmetry, δA_{beam}, versus octant and versus beam parameters. This is a typical example for a G^0 FPD. It can be seen that the beam charge and beam energy have the smallest contributions to the false asymmetry, below 0.1 ppm in absolute value, and that the geometric correction, due to beam position on target, have the biggest false asymmetry, though below 0.5−0.6 ppm.

given not only by the size of the average FPD slopes/sensitivities, $\bar{\alpha}'s$ but also by the size of the average helicity differences in beam parameters, $\bar{\delta x_i}$. Because of this, it is preferred in parity experiments to keep the helicity differences in beam parameters as small as possible through feedback systems. Extensive studies have been done to understand the FPD slope behavior over time [80]. By the end of the first engineering run this effect was still not fully understood, although its contribution/correction to the measured parity-violating asymmetry is small, at or below 0.5 ppm.

3.2.6 Background correction

The G^0 experiment was designed to have a detection scheme that separates elastic events from anything else. The detection scheme is based on a time of flight (ToF) spectrum of counted scattered particles originating in the target (the liquid hydrogen and the Al windows mainly, the helium in the helium cell has negligible thickness compared with the Al windows and the liquid hydrogen target). As there is no direct line of sight from the target to any of the FPD rings, neutrals originating in the target are shielded out. The positively charged particles with the appropriate kinematics are focused by the magnet into an FPD and get detected.

A typical measured ToF spectrum can be seen in fig. (3-1). There are three visible peaks in this spectrum, two rather sharp peaks at both ends of the spectrum in time and an extended peak in between. The sharp peak located at low times of flight is produced by fast particles, nominally π^+, which, having smaller mass compared to protons, move faster and reach an FPD segment in about 8 ns. The sharp peak located at high times of flight is produced by the elastically recoiled protons from the liquid hydrogen target. The protons, being heavier than the pions, are slow moving compared with pions and reach an FPD segment in about 20 ns. There is a net separation of about 10 ns between the two peaks, and so no contamination of pion events is expected in the elastic peak. Between the pion and the elastic proton peaks there is an extended peak, a third peak in the ToF, produced by particles heavier than pions and outside of the proton elastic kinematics. This peak is produced by background events, mostly inelastically scattered protons. As it can be seen from fig. (3-1), the elastic proton peak is located on the high times of flight tail of this background peak.

Due to this "*leaking*" of background events under the elastic peak not all the counts in the elastic peak are elastic events. The background correction refers to the procedure to correct the measured elastic asymmetries for dilution and asymmetry of the background events under the elastic peak and it is the subject of the present section.

Asymmetries can be formed in any time of flight bins according to eq. (3.2). In a similar way with the asymmetry formation for the elastic peak, helicity based asymmetries can be formed for any timebin for good quartets. These quartet asymmetries can be averaged over a run and the average can be quoted as the run asymmetry for that respective timebin. Over a number of runs these timebin run asymmetries can be summed as statistically independent measurements and a total average asymmetry can be obtained for that respective timebin over the whole data. The same procedure applied for summing up elastic asymmetries for an FPD segment is applied here: asymmetries are summed separately, for each timebin, over an IHWP state and the two IHWP states are combined together following eq. (3.13). In order to improve on the uncertainty of the timebin asymmetries over the whole data sample for the FR FPDs, which have timebins of 0.25 ns width, four timebins have been combined together into 1 ns timebins. Results for asymmetries versus ToF for four FPD segments, separately for FR and NA, are shown in figs. (3-14,3-15).

The four FPD segments in figs. (3-14,3-15) (4, 8, 10 and 14) have been picked to represent the range of the magnet's focal plane.

Asymmetries for timebins outside the elastic peak will be called background asymmetries. There is an apparent trend in figs. (3-14,3-15) for timebin asymmetries outside the elastic peak, common for both FR and NA (for a definition of the elastic peak please refer to fig. (3-1)). There seems to be a peak of positive background asymmetries that is located closer to the pion peak in the lower number FPDs, which *moves* toward the elastic peak as the FPD segment number increases. In FPD 14, the positive background asymmetry peak seems to enter the elastic peak.

If an asymmetry over the background peak is formed in the same way it is formed over the elastic peak, it has been observed that this asymmetry changes sign with the IHWP, and so it appears to be parity-violating in nature. The process that generates the

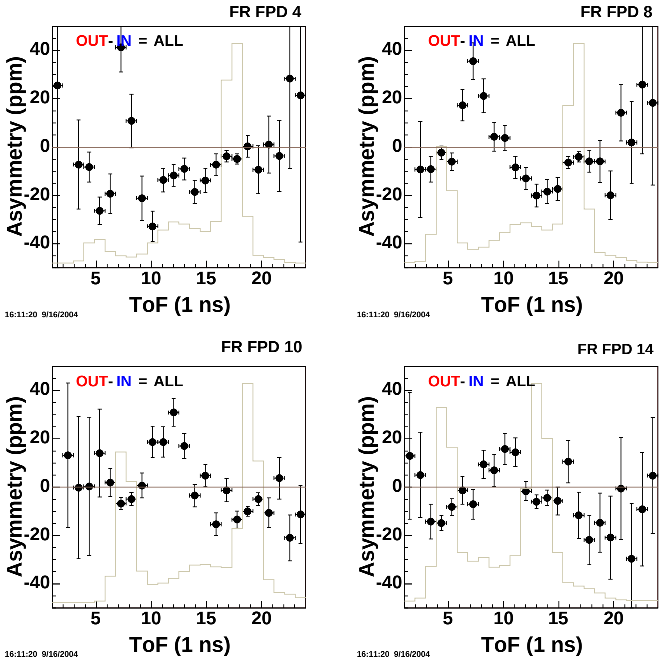

Figure 3-14: Asymmetry and normalized yield versus time of flight in a sample of four FR FPD segments (4, 8, 10 and 14). The 0.25 ns FR timebins are combined into 1 ns bins by summing four consecutive 0.25 ns bins together for one run and then summing all the runs over the whole data sample. Of the 32 ns ToF period only data for 24 ns around the elastic peak are plotted. The asymmetries are plotted in black color. The measured normalized yield versus timebin is displayed in light grey color. The vertical scale applies to asymmetries only, the ToF spectrum of the normalized yield has been scaled to fit in.

background asymmetries is unknown. Therefore the size and the sign of the background asymmetries are not understood and cannot be explained yet.

A simulation program [81, 82] has been developed based on Geant 3 package from CERN [83], called G0Geant, to try to understand the background in the experiment. Although the G0Geant simulation has been successful in accounting for the background dilution factors per FPD, it has no mechanism for generating asymmetries in the inelastic regions of the ToF. Fig. (3-16) displays the comparison between data from the first engineering run and the G0Geant simulation package. The ToF spectra were cut to display the region of interest around the elastic peak only. The simulation underpredicts

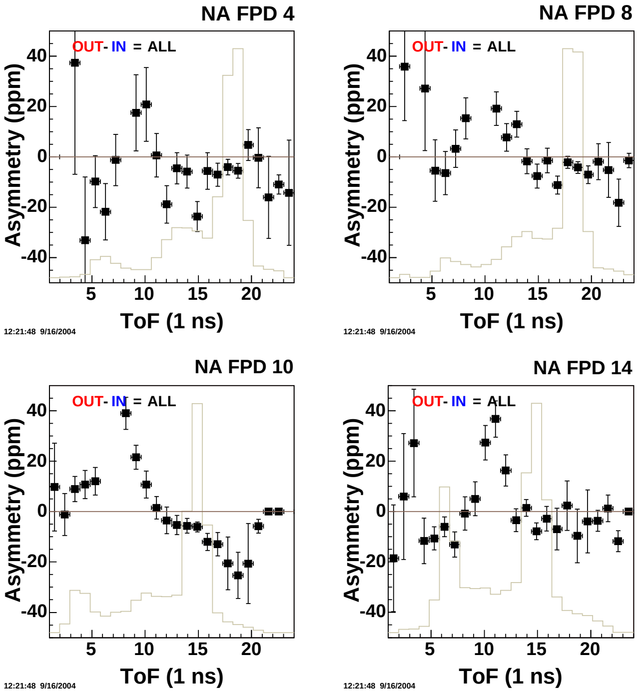

Figure 3-15: Asymmetry and normalized yield versus time of flight in a sample of four NA FPD segments (4, 8, 10 and 14). The NA timebins are 1 ns in width. The data has been summed for all the runs over the whole data sample. Of the 32 ns ToF period only data for 24 ns around the elastic peak have been plotted. The asymmetries are plotted in black color. The normalized yield versus timebin is displayed in the background in light grey color. The vertical scale applies to asymmetries only, the ToF spectrum of the normalized yield has been scaled to fit in.

the background data in the lower number FPDs and is in good agreement with the data for the higher number FPDs.

To make the background correction to the elastic data, knowledge of the background dilution under the elastic peak and the background asymmetry under the elastic peak is needed. There is no way that the generator of elastic events could be suppressed, and all the other experimental conditions would stay the same, to measure the background at the elastic peak location with sufficient statistics to make the correction. Because of this an indirect subtraction scheme for background under the elastic peak has been developed. In this scheme, data for timebins located on both sides of the elastic peak

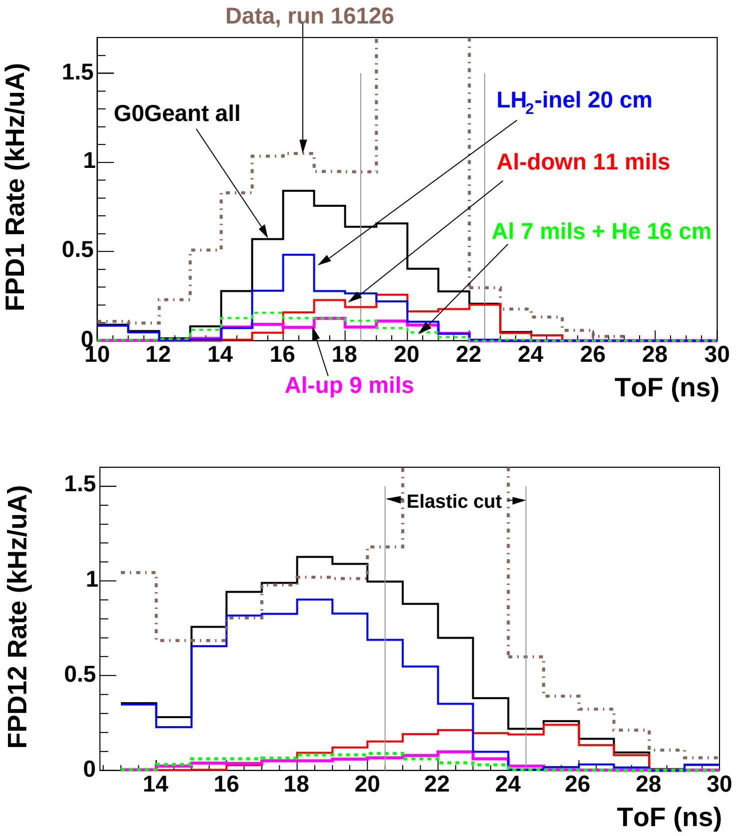

Figure 3-16: Normalized background event rates generated with G0Geant for FPDs 1 and 12. Total simulation rate, the simulation rates itemized by source, and rates from a data run are superimposed.

are used. Fits are made for both background yield and background asymmetry to the side bands of the elastic peak and interpolations are used to determine the background dilution and background asymmetry under the elastic peak. The corrections are done individually for each FR and NA FPD segment. For the FR FPDs three timebins were selected on the left of the elastic peak and three timebins on the right of the peak for fitting. For the NA FPD five timebins were selected on the left of the elastic peak and two on the right of the peak for fitting. Linear fits were considered for the FR FPDs for both yield and asymmetry. For NA FPDs quadratic fits were considered for yield and linear fits for asymmetry. Up to five combinations were considered of timebins from the

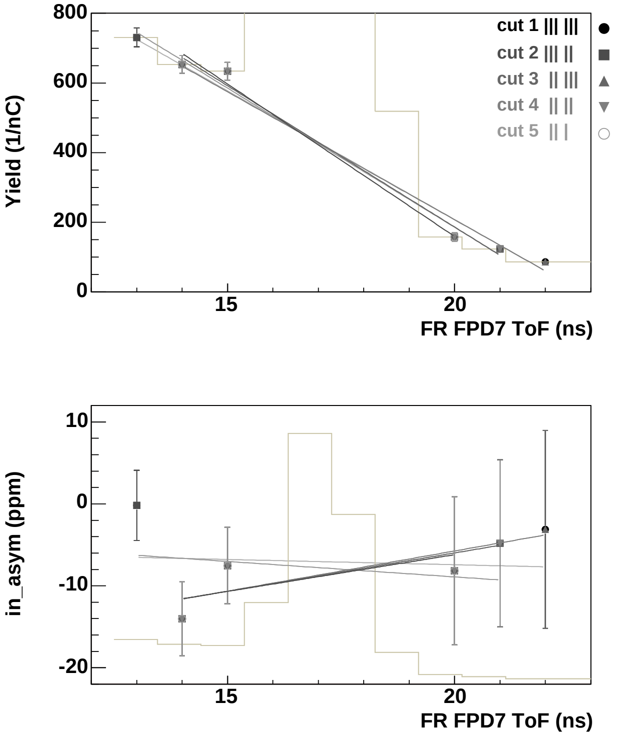

Figure 3-17: Background side bands for FR FPD 7, whole data. Upper plot: linear fits to the normalized yield in the ToF side bands of the elastic peak. The timebins in the side bands of the elastic peak that were taken into account for fitting are shown with vertical bars in the upper right corner. The lower plot shows the same procedure applied to the background asymmetry in the side bands, also with linear fits. In the lower plot the yield ToF spectrum is shown in light grey color. The vertical scale in this plot applies to background asymmetries, the ToF normalized yield has been scaled to fit in.

left with timebins from the right of the elastic peak. A combination of side band timebins is called cut. The cuts are illustrated with vertical bars (a bar signifies a timebin) in figs. (3-17,3-18) and in the summary figs. (3-19,3-20). For example, cut 1 for a FR FPD is made of three timebins from the left and three timebins from the right of the elastic peak, and cut 1 for a NA FPD is made of five timebins from the left and two timebins from the right of the elastic peak.

Considering the measured yield over the elastic peak in a quartet j to be factored into an elastic part and an background part: $\mathrm{Y}_j = \mathrm{Y}_{j,el} + \mathrm{Y}_{j,b}$, the measured asymmetry

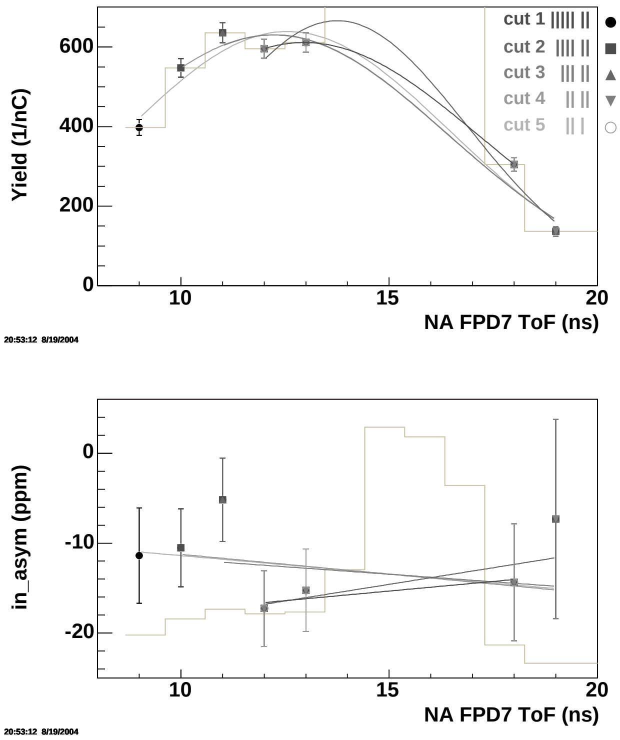

Figure 3-18: Background side bands for NA FPD 7, whole data. Upper plot: quadratic fits to the normalized yield in the ToF side bands of the elastic peak. The timebins in the side bands of the elastic peak that were taken into account for fitting are shown with vertical bars in the upper right corner. The lower plot shows the same procedure applied to the background asymmetry in the side bands, with linear fits. In the lower plot the yield ToF spectrum is shown in light grey color. The vertical scale in this plot applies to background asymmetries, the ToF normalized yield has been scaled to fit in.

over the elastic peak, eq. (3.2), can be written as

$$
\begin{aligned}
A_j &= \frac{Y_j^+ - Y_j^-}{Y_j^+ + Y_j^-} && (3.35)\\
&= \frac{Y_{j,el}^+ + Y_{j,b}^+ - Y_{j,el}^- - Y_{j,b}^-}{Y_{j,el}^+ + Y_{j,b}^+ + Y_{j,el}^- + Y_{j,b}^-} && (3.36)\\
&= \frac{\Delta Y_{j,el} + \Delta Y_{j,b}}{2(Y_{j,el} + Y_{j,b})} && (3.37)\\
&= \frac{Y_{j,el}}{Y_j}\frac{\Delta Y_{j,el}}{2Y_{j,el}} + \frac{Y_{j,b}}{Y_j}\frac{\Delta Y_{j,b}}{2Y_{j,b}} && (3.38)\\
&= f_{j,el}A_{j,el} + f_{j,b}A_{j,b} && (3.39)
\end{aligned}
$$

where subscripts *el* and *b* mean elastic and background respectively, and the dilution factors have been noted with f_{el} for the fraction of elastic events under the elastic peak, and f_b for the fraction of background events under the elastic peak; obviously $\mathrm{f}_{j,el}$ + $\mathrm{f}_{j,b}$ = 1. As asymmetries are measured in quartets and yields in MPSs they are statistically independent quantities, so averaging eq. (3.39) over the data sample, yields

$$A_m = (1 - f_b)A_{el} + f_b A_b \tag{3.40}$$

where f_b is the average background dilution for the elastic proton peak, A_b is the average background asymmetry under the elastic proton peak, and A_{el} is the corrected for background measured elastic asymmetry over the elastic proton peak. The uncertainty of the corrected for background elastic asymmetry, A_{el}, is given by

$$(\Delta A_{el})^2 = \Big(\frac{A_{el}}{1 - f_b}\Big)^2 (\Delta f_b)^2 + \frac{(\Delta A_m)^2}{(1 - f_b)^2} + \frac{1}{(1 - f_b)^2}[f_b^2(\Delta A_b)^2 + A_b^2(\Delta f_b)^2] \tag{3.41}$$

Since there are 3-4 timebins (1 ns each) in the elastic peak depending on the FPD number, the dilution factor can be determined from a fit with:

$$f_b = \sum_{i=1}^{N_{peak}} \frac{Y_{i,b}}{Y_{peak}} \tag{3.42}$$

where N_{peak} is the number of bins in the peak, $\mathrm{Y}_{i,b}$ is the background yield in bin *i*, and Y_{peak} is the total measured yield in the elastic peak. $\mathrm{Y}_{i,b}$ is determined from the fit. A statistical uncertainty can be assigned to the background dilution factor, f_b, based on eq. (3.42) (*i* is the bin index)

$$(\Delta f_b)^2 = \sum_{i=1}^{N_{peak}} \Big(\frac{\Delta Y_{i,b}}{Y_{peak}}\Big)^2 + \sum_{i=1}^{N_{peak}} \Big(\frac{Y_{i,b}}{Y_{peak}^2}\Big)(\Delta Y_{peak})^2 \tag{3.43}$$

where the uncertainty on the peak yield, $\Delta \mathrm{Y}_{peak}$, is determined from the data and the uncertainty on the extrapolated background yield in peak bin i, $\Delta \mathrm{Y}_{i,b}$, is matched with the side band yield uncertainties to follow statistics (normalized yield is counts/charge and the uncertainty in the mean of normalized counts is considered to follow statistics $\sim 1/\sqrt{Y}$.)

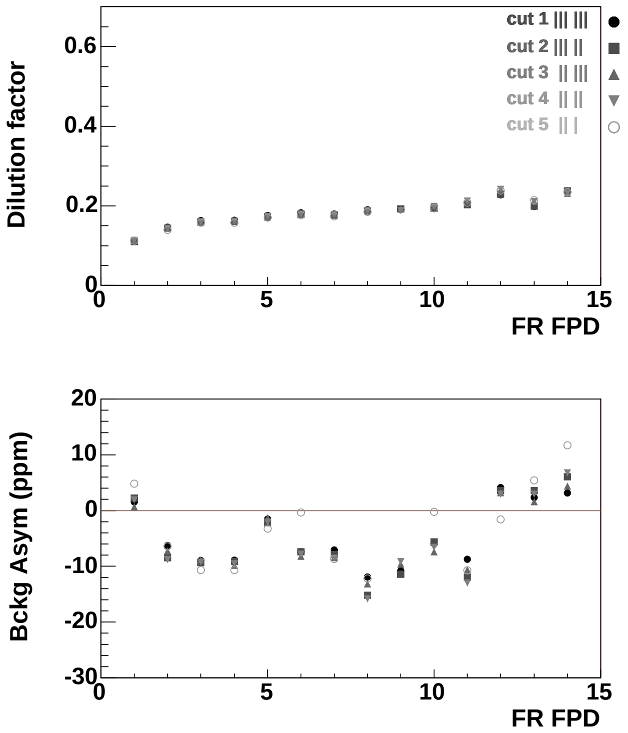

Figure 3-19: Background FR FPDs, whole data. Upper plot: variations of the dilution factors per FPD segment with the side band cuts to the elastic peak. Lower plot: variations of the background asymmetry under the elastic peak with the same cuts on the side bands. The range of variations in each case has been taken to be the systematic uncertainty for f_b, respectively for A_b.

The background asymmetry under the elastic peak can be determined with

$$A_b = \frac{\sum_{i=1}^{N_{peak}} Y_{i,b} A_{i,b}}{\sum_{i=1}^{N_{peak}} Y_{i,b}} \tag{3.44}$$

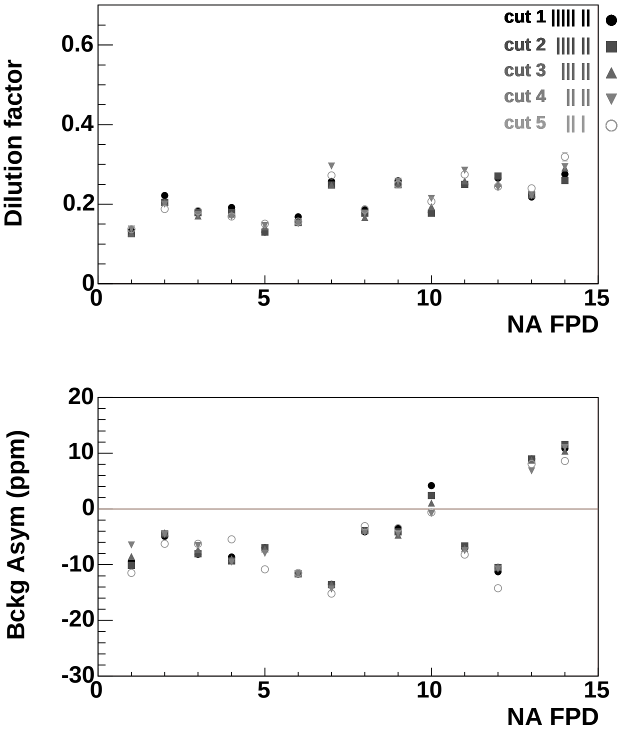

Figure 3-20: Background NA FPDs, whole data. Upper plot: variations of the dilution factors per FPD segment with the side band cuts to the elastic peak. Lower plot: variations of the background asymmetry under the elastic peak with the same cuts on the side bands. The range of variations in each case has been taken to be the systematic uncertainty for f$_b$, respectively for A$_b$.

where Y$_{i,b}$ and A$_{i,b}$ are the background yield and background asymmetry in bin i of the peak, and are determined from fitting. A statistical uncertainty can be assigned to A$_b$ in the same way it was assigned to the dilution factor, f$_b$, considering all the parts of eq. (3.44) as uncorrelated

$$(\Delta A_b)^2 = \sum_j \Big[\frac{A_{j,b}\sum_i Y_{i,b} - \sum_i (Y_{i,b}A_{i,b})}{(\sum_i Y_{i,b})^2}\Big]^2 (\Delta Y_{i,b})^2 + \sum_j \Big(\frac{Y_{j,b}}{\sum_i Y_{i,b}}\Big)^2 (\Delta A_{i,b})^2 \tag{3.45}$$

where the sums over j and i are over the number of bins in the elastic peak, and ΔA$_{i,b}$ it is not the fit uncertainty on A$_{i,b}$, but it is determined like the uncertainty for background yield, $\mathrm{Y}_{i,b}$, by matching it with the side band bins uncertainties on the background asymmetries to reflect the backgrounds events statistics in bin i of the elastic peak (which is $1/\sqrt{N_{i,b}}$, $\mathrm{N}_{i,b} = 4\mathrm{QY}_{i,b}$).

The fits to the side bands of the elastic peak are shown in fig. (3-17) for the FR FPD segment 7 and in fig. (3-18) for the NA FPD segment 7. As many as five side band cuts have been considered in fitting. Multiple cuts were considered to study the variation of the dilution factor and the background asymmetry and assign a systematic uncertainty for each one of them based on this. The systematic uncertainty for the interpolation method, for each FPD, for background dilution factors and asymmetry is taken to be the range of variation of the fitted quantity over all cuts. A summary of the ranges for dilution factor and background asymmetry is shown in fig. (3-19) for FR FPDs and in fig. (3-20) for NA FPDs. This method of assigning a systematic uncertainty for background dilution factor and asymmetry depends on the fitting procedure. The total uncertainties for background dilution factor, f_b, and background asymmetry, A_b are determined by summing for each FPD the statistical and systematic uncertainties in quadrature. The centroid is taken as the value determined from the fit with the best χ^2. The final results are shown in fig. (3-21) and numerical values are in tables C.1 and C.2, in addendum C. The FR background dilution factors show a regular monotonic increase with the FPD number with smaller and more regular uncertainties compared with the NA FPDs. The combined relative uncertainty (statistical and systematic) for a FR FPD is about 6%, while for NA it is about 10%. The shape of the f_b curve versus FPD number seems to be the same for both FR and NA, with the NA dilution factors varying around the FR ones. The background asymmetry under the elastic peak shows a trend too: it appears that the asymmetries are negative for FPDs up to about segment 11 for FR and segment 12 for NA, after which they change sign and become positive, this may be an indication of their Q^2 dependence, as the Q^2 increases with the FPD number. In absolute value, it appears that relatively large background asymmetries, as big as 10-15 ppm, are likely under the

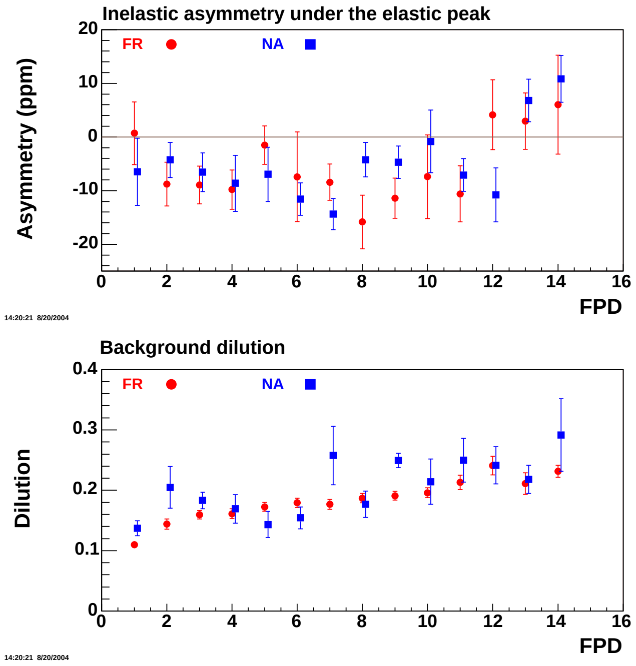

Figure 3-21: Summary plots for interpolated background under the elastic peak. Upper plot: background asymmetries. Lower plot: background dilution factors.

elastic peaks. Fig. (3-22) shows a summary of how the measured, *raw*, elastic asymmetry per FPD, and its uncertainty varied with each correction applied, except the correction related to the longitudinal beam polarization. Subtracting the false asymmetry generated by the helicity correlated beam parameters has a small effect on the measured elastic asymmetries. The correction for background, though, has a substantial contribution for some FPDs. The background subtracted elastic asymmetry uncertainty in fig. (3-22) is given by eq. (3.41).

Background asymmetries are less certain and stable through interpolating under the elastic proton peak. A different method (called the left-right method) from the interpolating method has been considered for estimating the systematic uncertainty for the elastic asymmetry due to the unknown shape and range of the background asymmetries under the elastic peak in an FPD segment. In this method the background asymmetry under the elastic peak is considered once to be given by the background asymmetry aver-

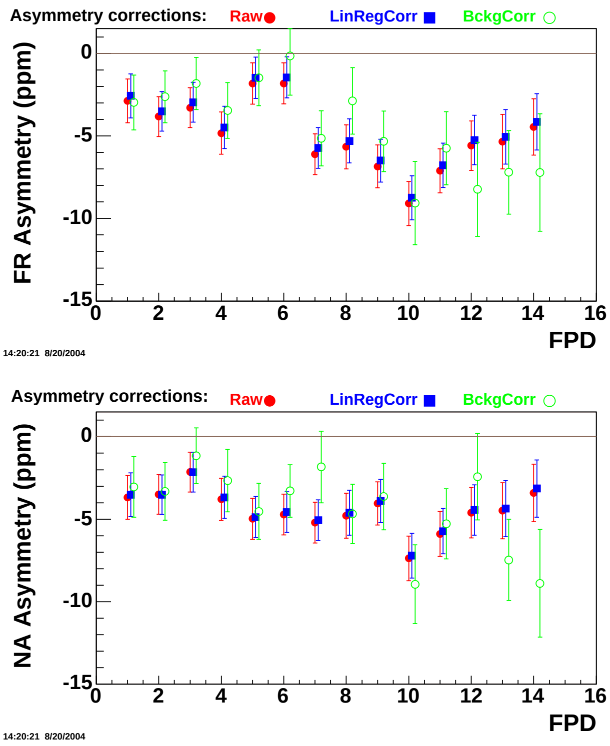

Figure 3-22: G^0 FPDs, separated in FR and NA, whole data. Elastic asymmetry per FPD: measured (raw), corrected for helicity correlated beam parameters (LinRegCorr) and corrected for background through interpolation (BckgCorr).

age on the right of the elastic peak band and once by the background asymmetry average on the left of the elastic peak band. A background correction to the measured elastic asymmetry is performed using eq. (3.40) with the “left” background asymmetry and the result is called the left- elastic-asymmetry, $A_{el,left}$. The same procedure is applied to the measured elastic asymmetry by using the “right” background asymmetry and the result is called the right-elastic-asymmetry, $A_{el,right}$. The systematic uncertainty due to the left/right background asymmetries is then given by

$$\Delta A_{el,lr} = 0.5 * |A_{el,left} - A_{el_{right}}| \tag{3.46}$$

This systematic uncertainty on the elastic asymmetry, eq. (3.46), is added in quadrature to the uncertainty for the elastic FPD asymmetry after the background subtraction is done using interpolating values for background dilution and asymmetry, eq. (3.41)

$$(\Delta A_{el,tot})^2 = (\Delta A_{el})^2 + (\Delta A_{el,lr})^2 \tag{3.47}$$

A correction is applied to the measured elastic asymmetry due to the longitudinal electron beam polarization. The electron beam polarization over the data sample was averaged to be $P_b = 77.52 \pm 0.12\%$, fig. (2-21). The elastic asymmetry is corrected for it with

$$A_{el,c} = \frac{A_{el}}{P_b} \text{ and } (\Delta A_{el,c})^2 = \frac{(\Delta A_{el,tot})^2}{P_b^2} + \frac{A_{el}^2}{P_b^2}\sigma_{P_b}^2 \tag{3.48}$$

where A_{el} is the background corrected elastic asymmetry, eq. (3.40) and $\Delta A_{el,tot}$ is given by eq. (3.47).

3.2.7 $\mathbf{Q^2}$ determination

The final step in the analysis is to distribute the measured and corrected elastic asymmetries, eq. (3.48), versus 4-momentum transfer, Q^2, in the elastic reaction *ep*. The 4-momentum transfer, Q^2, in the elastic kinematics for the reaction *ep*, in the ultrarelativistic limit for the incoming electron, is given in the proton coordinates in the lab frame by

$$Q^2 = \frac{4\lambda M_p^2}{1-\lambda}, \text{ where } \lambda \equiv \Big(\frac{E}{E+M_p}\Big)^2 cos^2\theta_p \tag{3.49}$$

where θ_p is the proton scattering angle in the lab frame. The Q^2 depends on two independent variables, according to eq. (3.49), on the incoming electron's energy, E, and on the scattered proton's angle, θ_p. The incoming electron energy is fixed by the CEBAF machine at 3 GeV in G^0 in the forward angle mode. The Q^2 varies with the proton scattering angle only and the angular acceptance in this running mode is between 76^o and 52^o, see table 1.6. The proton angular kinematics depends on the alignment of the

G^0 apparatus (target cell to SMS, SMS to ferris wheel and the G0 apparatus to beam line), on the magnetic field in the SMS, and on the ToF resolution.

Assigning Q^2 values to the G^0 FPD segments is done through the use of the G0Geant simulation package. In the simulation package electron's energy loss in the target and external electromagnetic radiative corrections are accounted for in determining the electron's energy at the scattering vertex, in the target, E. A complete account of the electromagnetic radiative corrections to the Q^2 is still in progress and preliminary results [84] suggest that these corrections are about 1% to the elastic asymmetry.

The profile of the Q^2 dependence on the ToF from the G0Geant simulation can be seen in fig. (3-23). FPDs 1-14 (the ones analyzed here) have the elastic peak situated between 20 and 24 ns in the ToF and the Q^2 values between 0.1 and 0.5 $(\mathrm{GeV})^2$. FPD 15 has a spread out elastic peak in the ToF with an almost linear Q^2 dependence on the ToF and a Q^2 acceptance between about 0.5 and 1 $(\mathrm{GeV})^2$. A proper factorization of the elastic peak in FPD 15 for both FR and NA octants into Q^2 bins requires high statistics data. It is not feasible to do this separation for this data sample and so FPD 15 is excluded from this analysis of the elastic asymmetries. The alignment precision of the G^0 apparatus influences the absolute precision of the ToF spectra recorded by the FPDs. The Q^2 dependence on the G^0 octants geometric offsets and the magnetic field in the SMS can be put as [85]

$$\frac{\Delta Q^2}{Q^2_{nom}} = a^B_{Q^2}\big(\frac{B}{B_{nom}} - 1\big) + a^x_{Q^2}\Delta x + a^z_{Q^2}\Delta z \tag{3.50}$$

where the $a^{B,x,z}_{Q^2}$ are the slopes, *nom* are nominal values in the experiment, and Δx, Δz are octant misalignments with respect to their ideal position along x and z axes of the G^0 coordinate system. The G^0 octants have been aligned to their ideal position to better than 3 mm in x and to better than 2 mm in z [87]. The $a^B_{Q^2}$ can be determined with the G0Geant simulation set for various values of the magnetic field in the SMS around

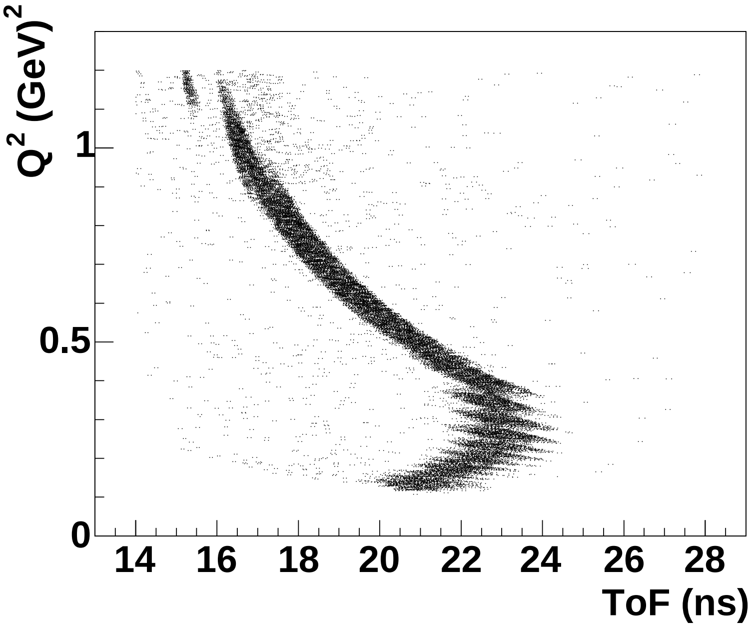

Figure 3-23: G0Geant simulation of elastic channel Q^2 dependence on time of flight.

the nominal value, like in fig. (3-24). The slope of the Q^2 versus magnetic field inceases mildly up to about FPD 11, from about 2.1%/% for FPD 1 to about 3.2%/% for FPD 11. The slope has a sharper increase for the FPDs 12, 13 and 14 to become about 5.4%/% for FPD 14. The magnetic field in the SMS is known to about 0.02% based on the stability of the dc current that flows in the magnet coils, [86], and on the precision of the ToF spectra, [85]. An upper limit on the Q^2 uncertainty due to the magnetic field can be placed at 0.1%. Combining this with the octant alignment values yields a total systematic precision for the Q^2 determination of better than 0.3%. The Q^2 bin values per FPD determined with the G0Geant package for the elastic channel are shown in table 3.2.

3.2.8 The physics asymmetries and strange vector form factors

The measured FPD elastic asymmetries have been computed on detection deadtime corrected data. These asymmetries were corrected for the false asymmetries caused by the

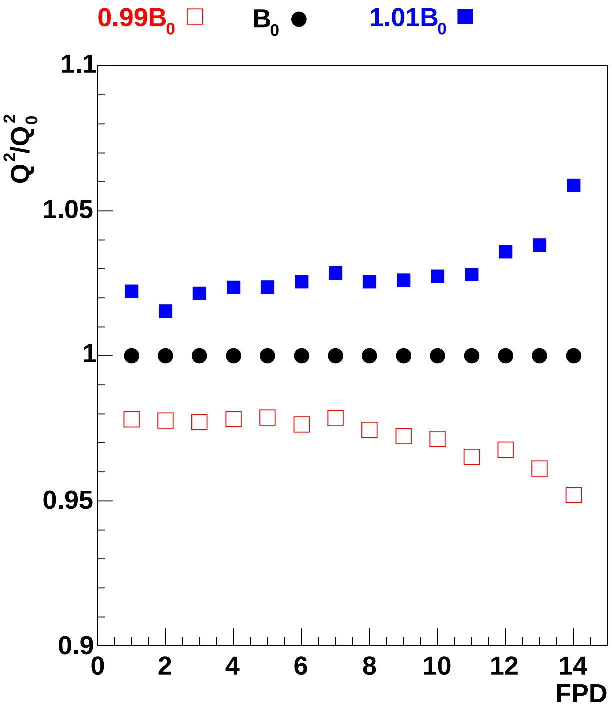

Figure 3-24: G0Geant simulation of elastic channel Q^2 variation with the magnetic field in the magnet.

helicity correlated beam parameters, for the background dilution and asymmetry under the elastic peak, and for longitudinal beam polarization. The corrections have been performed separately for the FR and NA FPDs. The corrected FR and NA FPDs elastic asymmetries have been combined together as statistically independent quantities and an asymmetry per FPD is quoted in the upper plot of fig. (3-25). In the lower plot is shown the Q^2 measured dependence of the physics parity-violating FPD asymmetries.

The physics asymmetry error budget is detailed in fig. (3-26), separately for the FR and NA FPDs and for the summed up asymmetries of the G^0 FPD. The contributions to the total uncertainty of a physics asymmetry have been considered to come from statistics, helicity induced beam parameters (linear regression), background (only the interpolation method uncertainties included in it, interpolated statistics and systematics of the interpolation method), background systematics (extracted with the left-right

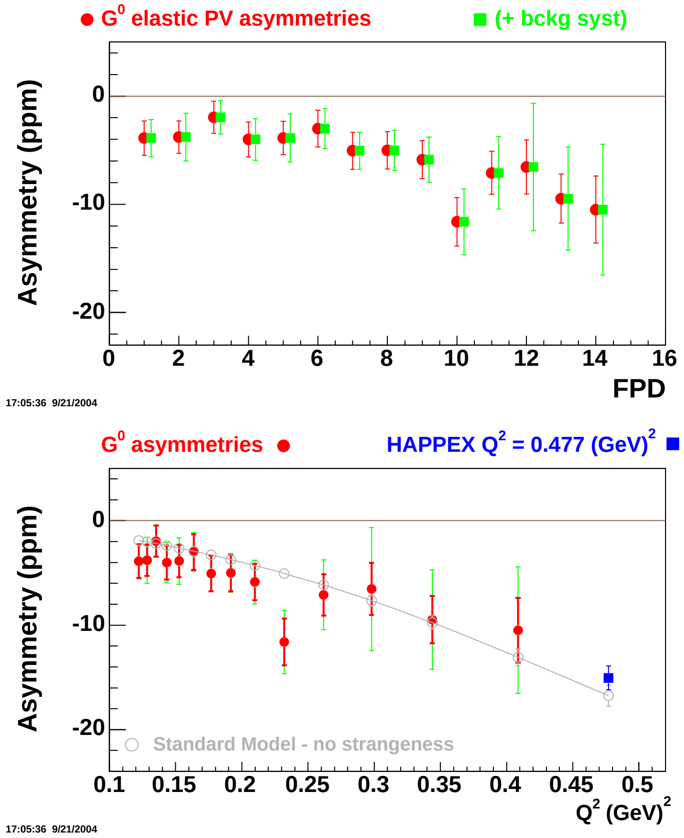

Figure 3-25: G^0 FPD physics asymmetries. Upper plot: asymmetry vs. FPD. Lower plot: asymmetry vs. Q^2. In the lower plot the data from HAPPEX I is plotted along with the standard model prediction for the parity-violating asymmetries in the case of no strangeness, eq. (1.52). The smaller error bars refer to the ΔA_{el}, eq. (3.41), while the larger error bars refer to eq. (3.47).

method) and beam polarization. The physics asymmetries uncertainties are dominated by background and statistics, with the lower number FPDs, up to about FPD 10 (low Q^2), dominated by statistics uncertainty and the higher number FPDs (mid-range Q^2) dominated by the systematic uncertainties. Linear regression and beam polarization corrections account for less than 1% contribution to the total FPD asymmetry uncertainty for all the FPDs.

Table 3.2 contains also the extracted vector strange form factors of the nucleon with

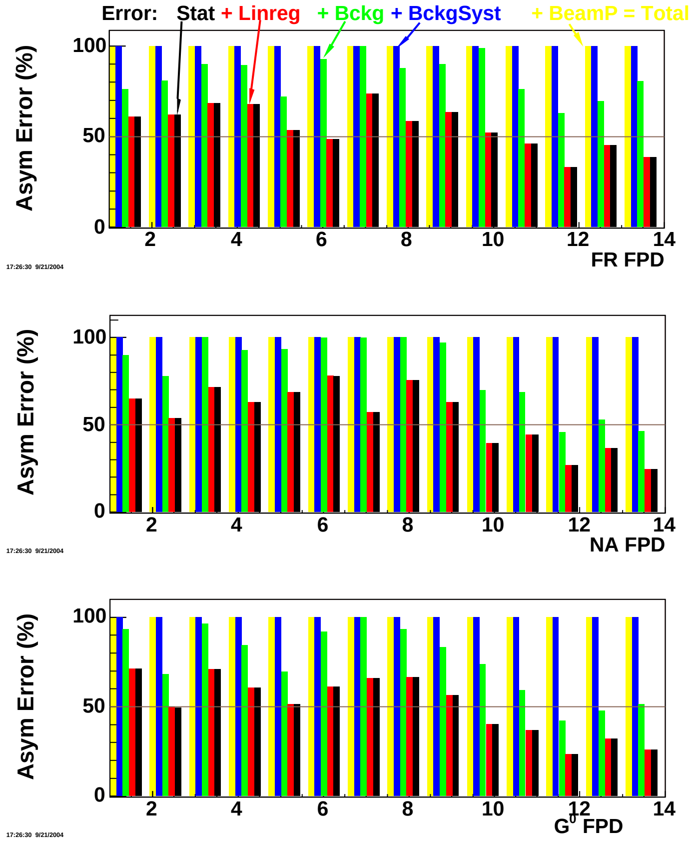

Figure 3-26: G^0 FPDs, elastic asymmetries error budget

eq. (1.52) versus Q^2, with the axial form factor determined with the eq. (1.59).

3.3 Outlook

The final results extracted from the analysis of this data sample are shown in the table 3.2. These are the results of the first measurement with the G^0 apparatus of a low statistics (9 C of beam charge on target) data sample in the forward angle mode. The completion of the G^0 physics program, as described in section 1.6, requires a high statistics (100 C of beam charge on target) physics run in the forward angle mode and six physics runs in the backward angle mode. The physics run in the forward angle mode acquired data in Feb-

Table 3.2: The physics asymmetries and form factors. The first uncertainty of form factors combinations is due to the nucleon electromagnetic form factors uncertainties, the second uncertainty is due to the measured physics asymmetry.

Det	Q^2 (GeV)^2	$A_p \pm \Delta A_{el,tot}$ (ppm)	α	$G_E^s + \alpha G_M^s$
1	0.1223	-3.876 ± 1.999	0.097	-0.161 ± 0.015 ± 0.141
2	0.1284	-3.784 ± 3.576	0.102	-0.135 ± 0.015 ± 0.173
3	0.1353	-1.950 ± 1.702	0.108	0.018 ± 0.015 ± 0.114
4	0.1433	-4.003 ± 2.631	0.114	-0.111 ± 0.016 ± 0.134
5	0.1526	-3.865 ± 3.535	0.122	-0.079 ± 0.016 ± 0.143
6	0.1636	-2.997 ± 2.236	0.130	-0.005 ± 0.016 ± 0.110
7	0.1767	-5.048 ± 1.702	0.141	-0.096 ± 0.017 ± 0.094
8	0.1916	-5.010 ± 2.176	0.153	-0.064 ± 0.017 ± 0.093
9	0.2097	-5.874 ± 2.915	0.168	-0.072 ± 0.018 ± 0.096
10	0.2321	-11.614 ± 4.679	0.187	-0.264 ± 0.018 ± 0.125
11	0.2618	-7.095 ± 5.745	0.211	-0.033 ± 0.019 ± 0.118
12	0.2979	-6.544 ± 10.978	0.242	0.034 ± 0.020 ± 0.178
13	0.3438	-9.469 ± 8.683	0.281	0.001 ± 0.021 ± 0.123
14	0.4087	-10.481 ± 10.829	0.337	0.054 ± 0.022 ± 0.127

May, 2004, and the analysis of these data is currently unde way. For the backward angle running modes the G^0 apparatus will be turned by 180^o about the electron beam line and three Q^2 bins will be sampled in sets of two runs each, one run on a liquid hydrogen target and one run on a liquid deuterium target (see details in section 1.6). Besides turning by 180^o there are no changes to the SMS for backward angle running modes. The target cell will sit about 60 cm further downstream from the service module with respect to the position it had for the forward angle mode. The FPD will be complemented with two sets of new detectors: the cryostat exit detector (CED) and the Aerogel Cerenkov detector

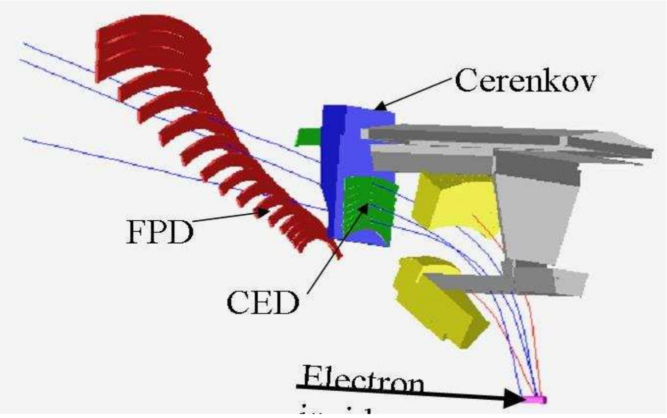

Figure 3-27: G^0 backangle detection.

(AED), see fig. (3-27). In the backangle mode the particle detected is the electron. The CED is made, like the FPD, of 8 octants, positioned right at the exit Ti windows of the SMS, fig. (3-27). Each octant is made of 9 single scintillator paddles. The detection scheme in the backangle mode is based on a coincidence method between pairs of CED-FPD scintillators. In the backangle mode only the front scintillator of a FPD segment is used. In this detection scheme asymmetries for elastic and inelastic events will be measured. The ACD will be used for the runs with a liquid deuterium target. The ACD has been designed to provide pion rejection across the full G^0 momentum range [88].

The first backangle run is scheduled to take data in the winter of 2005-2006 for the Q^2 bin of 0.8 $(\mathrm{GeV})^2$. It will take about three more years for the whole G^0 physics program to be completed. At the completion of the experiment the vector strange electric and magnetic and the axial form factors of the nucleon will be separated for three Q^2 bins, 0.3, 0.5, and 0.8 $(\mathrm{GeV})^2$.

Appendix A

Asymmetry summation studies

The measured parity-violating asymmetry can be summed up in different ways over the timebins in the elastic peak and over the number of quartets in a run. Studies have been done to determine which summation method is more stable if time jitters are present in the ToF spectra. The results of these studies are presented in this appendix.

A.1 Asymmetry summation

The asymmetry definition, eq. (3.2), for a timebin over a quartet is unique, but there are different ways of summing over a peak and over a number of quartets. Due to this a consistent summation scheme for asymmetry over the elastic peak has to be developed. As it will be seen in what follows there are three different ways in which the summation of the elastic asymmetry over the elastic peak and over a number of quartets can be defined. It can be proven mathematically that if the timebins are statistically independent the three summation methods are equivalent over a run. During the acquisition of the data analyzed here the beam pickoff (the YO) signal was at times unstable. One effect that these timing instabilities or jitters have is to correlate the yield and asymmetry as measured by different bins in the same ToF spectrum. This affects mostly the FR half of the G^0 detector as the FR electronics has a more intimate use of the YO signal in generating the 0.25 ns timebins in the ToF. This timing jitter affects the asymmetry summation in the FR detection scheme.

The definition of the asymmetry summation schemes will be given in what follows and a simulation program aimed at sorting out the best summation method will be discussed.

A.1.1 Asymmetry summation

There are three asymmetry summation methods: the summation over the elastic proton peak treated as a single bin, the independent bin summation over the bins in the elastic peak and the counting statistics summation. Let i be the bin index in the peak, j be the quartet index in a run, N_b be the number of bins in the peak and N_q be the number of quartets in a run. The P index will designate *"peak"* and p will designate *"particle"*.

1. For the **peak summation** method the quartet asymmetry is made in normalized yields over the peak in a quartet. The peak yield is the sum of same helicity state normalized yields in the bins in the peak.

$$A_{Pj} = \frac{Y^+_{Pj} - Y^-_{Pj}}{Y^+_{Pj} + Y^-_{Pj}} = \frac{\sum_{i=1}^{N_b} Y^+_{ij} - \sum_{i=1}^{N_b} Y^-_{ij}}{\sum_{i=1}^{N_b} Y^+_{ij} + \sum_{i=1}^{N_b} Y^-_{ij}} = \frac{\sum_i \Delta Y_{ij}}{\sum_i Y_{ij}} = \frac{\sum_i Y_{ij} \cdot A_{ij}}{\sum_i Y_{ij}} \tag{A.1}$$

Where A_{ij} is bin i asymmetry in quartet j, and Y_{ij} is the measured normalized yield in bin i during quartet j. Histogramming A_{Pj} over N_q quartets yields the peak run asymmetry and its error.

$$A_P = \frac{1}{N_q} \cdot \sum_{j=1}^{N_q} A_{Pj}, \text{ and } \sigma_P^2 = \frac{1}{N_q(N_q-1)} \sum_j (A_{Pj} - A_P)^2 \tag{A.2}$$

From this run asymmetry and error (where the error on the mean has been computed by using an unbiased estimator of the sample's variance), the final asymmetry and error are computed as an independent measurements sum of (A_P, σ_P) over the number of runs. The definition of the $p$eak summation method follows the definition implemented in the official offline replay engine for this experiment.

2. For the **independent timebin summation** method the individual timebin quartet asymmetry is as given by eq. (A.1) without the sum over bins. The timebin quartet asymmetry gets histogrammed and at the end of the run, after N_q quartets, the bin asymmetry is given by something like eq. (A.2), (A_i, σ_i), and the timebin asymmetries and errors are summed over the elastic peak as statistically independent measurements to yield an asymmetry over the peak and its error for that run. Over a number of runs, the run asymmetries and their errors are summed as statistically independent measurements (just like the peak asymmetries are):

$$A_{PI} = \frac{\sum_{i=1}^{N_b} \frac{A_i}{\sigma_i^2}}{\sum_{i=1}^{N_b} \frac{1}{\sigma_i^2}}, \; \frac{1}{\sigma_{PI}^2} = \sum_{i=1}^{N_b} \frac{1}{\sigma_i^2}, \text{ where } A_i = \frac{1}{N_q} \sum_j A_{ij}, \text{ and } \sigma_i^2 = \frac{1}{N_q(N_q-1)} \sum_j (A_{ij} - A_i)^2 \tag{A.3}$$

3. For the **counting statistics summation** the timebin asymmetry in a quartet is as given by eq. (3.2), the peak asymmetry over a quartet is as given by eq. (A.1), and the run asymmetry, over N_q quartets is given by:

$$A_{CS} = \frac{\sum_{j=1}^{N_q} N_{Qj} \sum_{i=1}^{N_b} Y_{ij} A_{ij}}{\sum_j N_{Qj} \sum_i Y_{ij}}, \text{ and } \frac{1}{\sigma_{CS}^2} = \sum_j (N_{Qj} \sum_i Y_{ij}) \tag{A.4}$$

where N_{Qj} is the charge in quartet j.

In the case of a number of runs, A_{CS}, σ_{CS} will be given by the respective sums eqs. (A.4) over the number of quartets in all the runs, as if there is just one big run with a never ending chain of quartets.

Using the above mentioned definitions for the three summation methods to show that they are all equivalent among themselves, actually leads to mathematical absurdities due to the choice of *peak summation*. To show that eq. (A.2) is the same as eq. (A.3), eq. (A.2) is expanded as:

$$A_P = \frac{1}{N_q}\sum_{j=1}^{N_q} A_{Pj} = \frac{1}{N_q}\sum_{j=1}^{N_q}\frac{\sum_i Y_{ij}A_{ij}}{\sum_i Y_{ij}} = \frac{1}{N_q}\sum_{j=1}^{N_q}\frac{a_j}{b_j} \tag{A.5}$$

where a$_j$ and b$_j$ are just notations for the respective numerator and denominator sums over number of quartets. Expanding eq. (A.3) with the assumption that the timebins satisfy counting statistics: $\sigma_i^{-2} = N_Q Y_i = \sum_j N_{Qj} Y_{ij}$ (where N_Q is a generic notation to keep track of the fact that in the summation over the number of quartets the charge in a quartet has to be included) and using the definition of A_i as given by eq. (A.3):

$$A_{PI} = \frac{\sum_i N_Q A_i Y_i}{\sum_i N_Q Y_i} = \frac{1}{N_q}\frac{\sum_i \sum_j N_Q A_{ij} Y_i}{\sum_i N_Q Y_i} \tag{A.6}$$

Using the fact that the quartet asymmetry and yield in a bin should be statistically independent, which means that $Y_i \sum_j A_{ij} = \sum_j A_{ij} \sum_k Y_{ik} = N_q \sum_j A_{ij} Y_{ij}$ and the fact that two successive sums commute with each other ($\sum_i \sum_j a_{ij} = \sum_j \sum_i a_{ij}$), eq. (A.6) becomes:

$$A_{PI} = \frac{\sum_i \sum_j N_{Qj} A_{ij} Y_{ij}}{\sum_i \sum_j N_{Qj} Y_{ij}} = \frac{\sum_j N_{Qj} \sum_i A_{ij} Y_{ij}}{\sum_j N_{Qj} \sum_i Y_{ij}} = \frac{\sum_j N_{Qj} a_j}{\sum_j N_{Qj} b_j} \tag{A.7}$$

Eqs. (A.5) and (A.7) are not the same, but eq. (A.4) is the same as eq. (A.7), which means that the independent timebin summation as defined by eq. (A.3) is equivalent with the counting statistics summation as defined by eq. (A.4), but that they are mathematically different from the peak summation as defined by eq. (A.2). In an experiment sitting on counting statistics, the straight sum of peak quartet asymmetries to get the mean asymmetry is just wrong, rather a sum like this is correct:

$$A_P = \frac{\sum_j \frac{A_{Pj}}{\sigma_j^2}}{\sum_j \frac{1}{\sigma_j^2}} = \frac{\sum_j N_{Qj} A_{Pj} Y_j}{\sum_j N_{Qj} Y_j} = \frac{\sum_j N_{Qj} \sum_i Y_{ij} A_{ij}}{\sum_j N_{Qj} \sum_i Y_{ij}} \tag{A.8}$$

which makes all three summation methods mathematically equivalent $A_P \equiv A_{PI} \equiv A_{CS}$.

In conclusion eq. (A.2) is not a mathematically consistent definition of the asymmetry summation for an experiment that sits on counting statistics, which doesn't mean that in the G^0 experiment it has to be changed to eq. (A.8). In the real experiment the counting statistics condition is only met approximately, and, even if the quartet counting is dominated statistically, there are systematic uncertainties that are not contained in σ_j (which is the peak asymmetry width or statistics over a quartet j). Using a wrong weight for asymmetry summation is worse than leaving the quartet asymmetry weightless and use other methods to extract the systematic uncertainties to the measured asymmetry. A case for eq. (A.2) as a summation method for asymmetry over timebins in a peak and over quartets in a run will be made in what follows.

A.1.2 Timing simulation

A simulation program has been written to try to sort out the best summation method in the context of timing (YO) jitters. There are no beam charge asymmetry and electronics deadtime considerations taken into account in it.

The simulation is based on reconstructing the elastic proton peak from the real experiment based on scattered events rather than beam events. It was assumed that the elastic peak in a typical detector is described by a gaussian distribution sampled with histograms with 24 identical timebins, which is suitable enough to catch the whole distribution of an elastic peak that in the real experiment spans on average 16 FR timebins. For convenience the gaussians' mean was put in the middle of the histogram, in timebin 12, and the width of the distribution was made to mimic the real distribution's width of about 2 timebins. A background was added on top of the gaussian to try to get closer to the real experiment. The types of backgrounds considered here were linearly dropping from left-side to the right-side of the elastic peak or flat. In the end the background type was found to have no influence on the results and conclusions. For these results the background level was taken to be about 20% of the *"elastic"* yield and it was considered to be linearly dropping from the left of the peak to the right of it.

The choice for a gaussian distribution of detected events was made based on the counting statistics in the real experiment. The typical rate in a single detector paddle in G^0 in the forward running mode is 1-2 MHz. In a quartet there are then more than $2{\cdot}10^5$ particles detected, of those at least half are elastic events distributed over 16 FR timebins in the ToF, or on average, even in the low statistics timebins of the peak, more than 10^3 events. The poissonian distributed counts can then be approximated as gaussian distributed in all the timebins in the elastic peak and also in the peak itself, which to some extent can be viewed just as a *"big"* timebin.

There are three loops central to the simulation, one over the number of quartets, one embedded in it, over the number on macropulses, and one embedded in the second one over the number of particles detected in a macropulse. The number of particles detected in a macropulse is taken to be Poisson distributed, with the mean close to the experimental one. Events/particles are generated one by one according to a gaussian distribution function using a random number generator provided by Root (). Two macropulses worth of data are filled in a histogram, and the other two macropulses from the same quartet in a different histogram. Asymmetries are formed the same way they are in the real experiment, between the two *"polarities"* of a quartet. Since there is no *"mechanism"* for generating an actual asymmetry in this simulation, the simulated asymmetry should just be an estimator of zero.

The elastic peak was distributed with a gaussian $p.d.f.$ like:

$$f(x) = C \cdot e^{-\frac{(x-\mu(t))^2}{2\cdot\sigma^2}} \tag{A.9}$$

where

$$\mu(t) = 12 \cdot [1 + J \cdot sin(2\pi\nu t)] \tag{A.10}$$

where J is the amplitude of the time jitter, taken to be the absolute resolution in time of flight of the FR electronics, 0.2 of a timebin or 50 ps, and t is the control variable that gets affected by the so-called jitter frequency. The choice of *sine* function is somewhat arbitrary and has no special meaning in this context other than a way of producing time jitters on the mean of the Gaussian between $-J$ and $+J$. A change of the t variable reflects a *"kick"* in time felt by the real gaussian distribution from timing instabilities, most probably inside electronics modules, cables, leaking signals etc. Changes in t have been modulated inside the loop for *"detected"* particles and transformed into approximate detection frequencies.

There were six elastic peak cuts considered and six J values or frequencies. The peak cuts were considered to determine the running of the asymmetry error and to study the loss of statistics with the cut. The cuts implemented for this simulation were all symmetric around the mean, but asymmetric cuts were also considered separately, which didn't have any effect due to the asymmetry only on the csf or on the stability of the peak error with the jitter frequency. The six peak cuts and the six frequency cases have been superimposed on summary plots for the counting statistics fraction, eq. (3.6) and asymmetry error running. The counting statistics fraction csf, showed in fig. (A-1) was computed on a bin by bin basis for the peak summation method. The six points, in all the plots, at abscissa values greater than 25 are the csf over the peak for the six peak cuts considered. In fig. (A-1) the first plot has all the data, elastic + linear background and the second plot has the elastic only. The time jitter effect on csf is maximal at the MPS

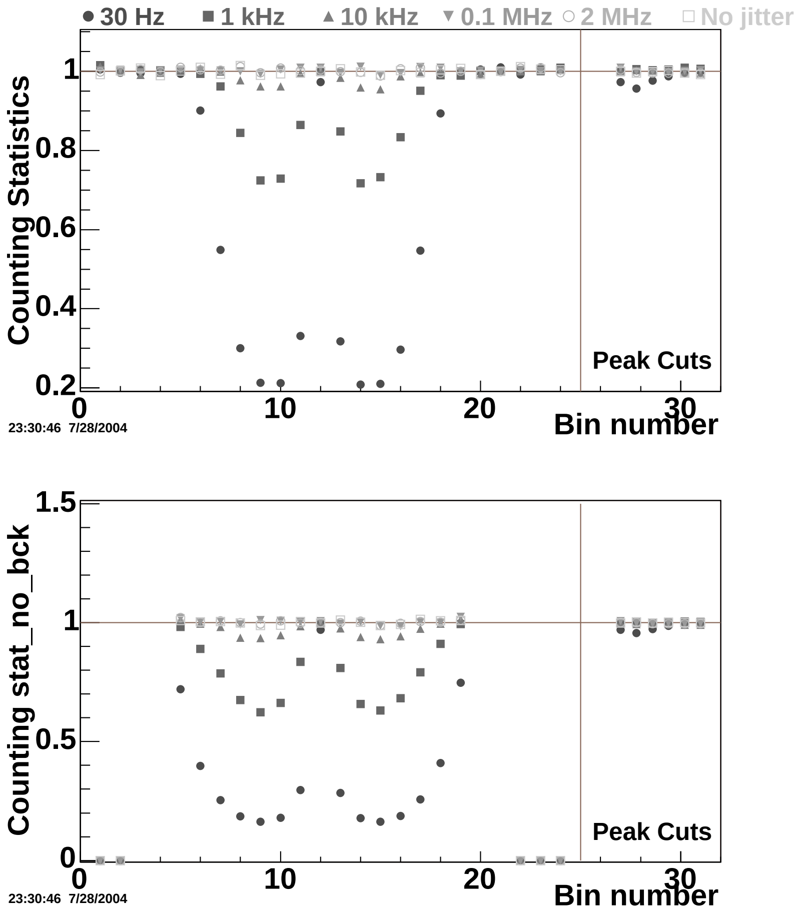

Figure A-1: Simulation: Counting statistics fraction behavior over the peak and with the peak's cut

level (30 Hz). The csf for the timebins in the elastic peak drops dramatically and has the lowest values in the timebins that contain the inflexion points of the real *p.d.f.*, about 0.2. This is a huge drop from what the value of this parameter should be for statistically dominated timebins (in a reasonably long run with more than 10000 quartets) just a few percents off unity.

The timebin with the mean of the peak doesn't get affected whatever the time jitter frequency might be. Another observed effect of the timing drifts in the *p.d.f.* is the onset of correlations between timebins in the peak for both yield and asymmetry. The

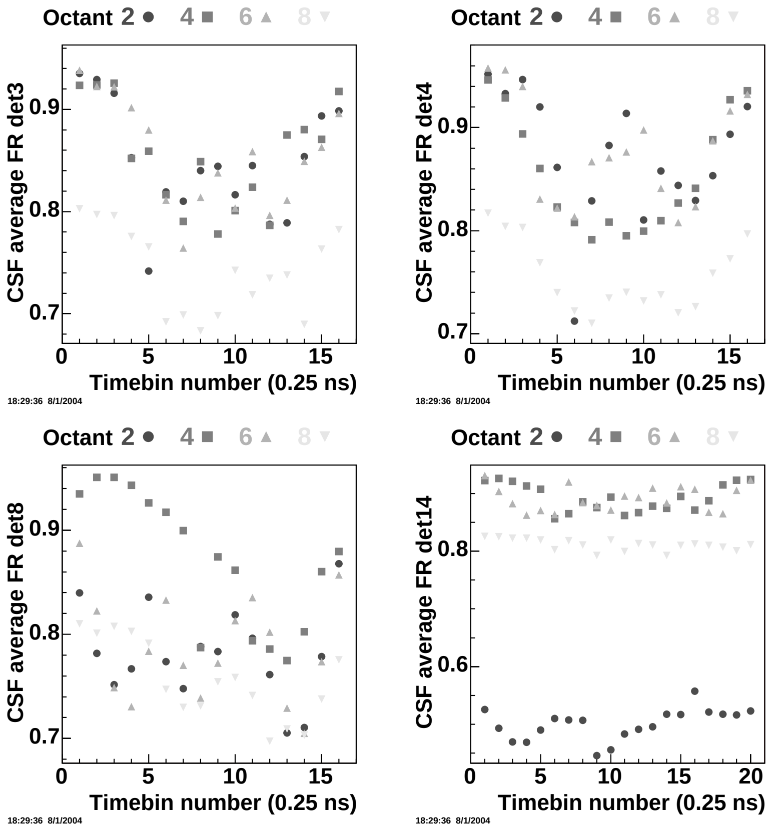

Figure A-2: Data: Counting statistics fraction for four different FR FPDs, all four octants separated, sum over runs

correlations happen among all the bins in the peak, not just between the closest neighbors. The correlation coefficients behave in a similar manner like csf, they are maximal at 30 Hz and drop as the time jitter frequency increases. For jitters that happen at the detected particle level, the randomization is fully reestablished and the correlations all but disappear. An interesting effect appears in the case of time jitters at the QRT level or 7.5 Hz. In this situation only the yield is correlated but not the asymmetry. The asymmetry is computed in quartets and as expected asymmetry correlations should not happen beyond the MPS level, but yield correlations are possible at the QRT level. The fact the in the real experiment correlations are seen between both yield and asymmetry among different timebins and not just timebins' yield, means that the mechanism for correlations does not happen at the QRT level.

As a conclusion of the summary plot from fig. (A-1), for time jitter frequencies above 10 kHz the bin-bin correlations in both yield and asymmetry die completely and the csfs get into the counting statistics regime for all timebins in the peak for all the cuts over the peak. Comparing these results with data from the first G^0 engineering run, fig. (A-2) (the data have been summed over all good runs, and so it displays a time average of the csf per bins in the elastic cut, per detector, and each octant considered separately), it appears that the most likely time jitter frequencies reflected by the data are in the range $1-10$ kHz, by comparing the size of the dip in the *winged* region of the peak around the timebin that contains the centroid. Since in fig. (A-2) there is no dramatic dip in the csf in the timebins in the elastic peak it appears that jitter frequencies lower than 1 kHz are not present in the real data, at least not over extended periods of time. Fig. (A-2) shows four FR FPDs, 3 and 4 in the upper two plots, and 8 and 14 in the lower two, with each octant separately plotted. FPDs 3 and 4, octants 2 and 6 have a pronounced winged shape of the csf even after averaging over the whole data sample. The same conclusion cannot be drawn for the other FPDs and for 3 and 4, octants 4 and 8. Sampling the data from individual runs it was found that sometime there are correlations in yield and asymmetry between individual timebins in the elastic peak and sometime the timebins appear statistically independent.

The csfs for the peak cuts, see fig. (A-1) bins higher than 25, are stable with the peak cut and insensitive to the time jitter for all frequencies and in all the elastic peak cuts for both data sets, elastic + background and elastic only. According to the simulation it looks like the counting statistics is preserved in the peak (regardless of the peak cut and/or jitter frequency), although some of the bins in the peak could be severely impaired with respect to counting statistics, depending on the range of jitter frequency. Fig. (A-3) shows the behavior of the asymmetry uncertainty. The first plot displays the relative change in the asymmetry errors between two asymmetry summing methods, the independent bin

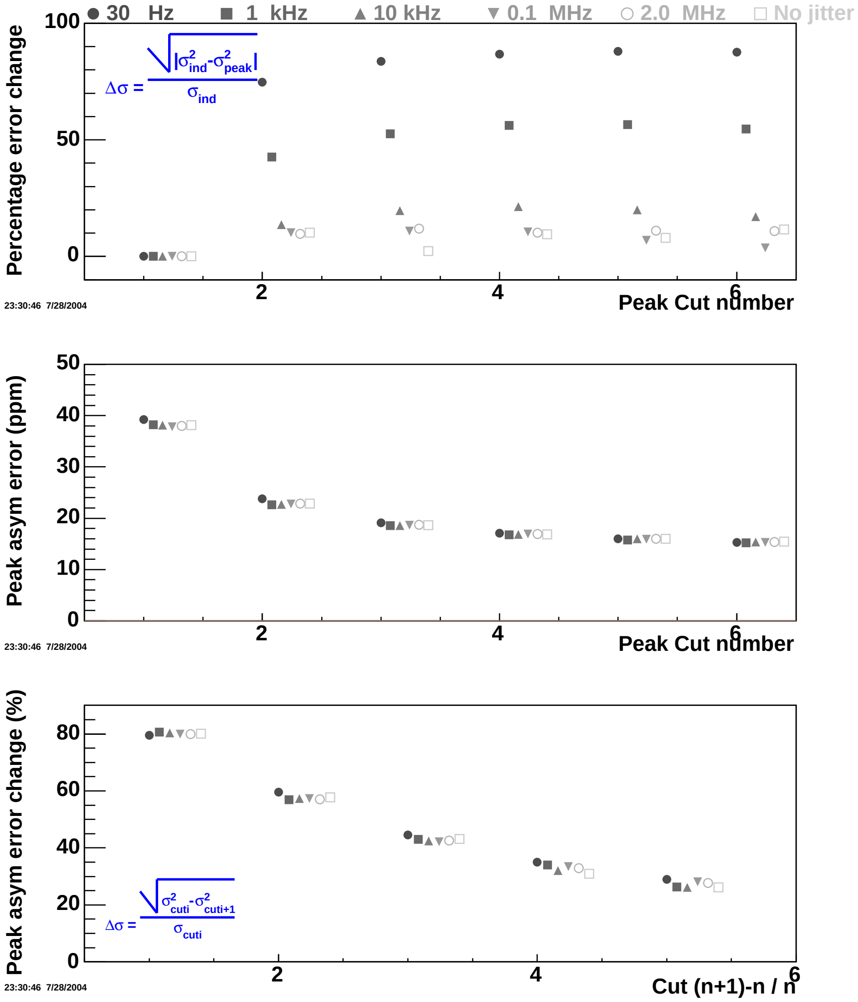

Figure A-3: Asymmetry error behavior for the peak summation with the peak's cut method and the peak method. The changes are recorded versus peak cut and time jitter. As can be seen from it the independent bin summation, when it is done bluntly, without accounting for bin-bin correlations, overestimates the asymmetry error by as much as 80% for a timing jitter at the MPS level (or 30 Hz). In the case of real data, where the time jitter seems to be in the kHz range, the overestimate in error is around 30%, which is consistent with what was determined in a comparison analysis between the two summations in the real data from the first engineering run. The second plot shows the behavior of the peak summation asymmetry uncertainty with peak cut and time jitter. The plot suggests that the uncertainty for the asymmetry as estimated with this method is very stable in all the peak cuts with the time jitter variations. The third plot displays the running of the asymmetry uncertainty as determined by the peak summation method between peak cuts. The idea here is to try to estimate the loss of elastic events statistics due to background clipping of the elastic peak tails. As expected from the second plot, the time jitter has no influence on how the asymmetry uncertainty varies with the cut. Extrapolating, the real experiment is in the case of Cut 4 to Cut 5, meaning that Cut 4 is taken into account, but Cut 5 gets smeared by background and the elastic events are lost. This suggests that there is about 15% loss of elastic events statistics in the real experiment due to the cut on the elastic peak because of the background.

These results strongly suggest that the peak summation method for determining asymmetries is very stable against peak cuts and jitters in timing at any level. The independent bin summation overestimates the uncertainty of the asymmetry depending on the level of correlations between bins, and the counting statistics summation underestimates it. The fact that bin-bin correlations in yield and asymmetry always seem to happen for pairs of octants suggests that the cause may be traceable to the DMCH module(s), as these modules serve a pair of octants. For the first engineering run it was believed that the cause of correlations ultimately lies with the instabilities in the YO signal, but in the second engineering run bin-bin correlations have been observed even when the YO signal was stable, suggesting that the cause lies mostly with the internal state of a DMCH module. The real cause has not been identified yet, but whatever the cause(s) might be, the peak summation seems to be unaffected by it(them). In conclusion, the peak method is used to sum the quartet asymmetries over the number of quartets in a run for each FPD.

Appendix B

Target density variation studies

This addendum contains the G^0 target density variations studies that were done during the two G^0 engineering runs. The conclusions of these studies with regard to their influence on the measured parity-violating (PV) asymmetry are presented in section 2.4.3.

B.1 Boiling studies

Dedicated data were acquired during each of the engineering runs to study the density fluctuations on the time scale of the asymmetry measurement. The detection technique in G^0 is based on a time of flight spectrum and has been described in section 2.5. There are two effects caused by the target that influence the measurement of the parity-violating asymmetry. Since the target is a liquid it can have density fluctuations and global density reduction. Density fluctuations are random changes in the liquid density driven mainly by either fluctuations in beam properties (like intensity, position etc.) or random effects due to the interactions between beam particles and the target liquid (microscopic bubble formation, window heating etc.). The mechanisms for density fluctuations are complex and realistic cases are poorly understood quantitatively. Their effect translates directly into an enlargement of the measured asymmetry width. This enlargement in turn is an additional source of statistical uncertainty in the asymmetry measurement and it thus increases the asymmetry error bar. Density reduction is a global reduction in the density of the liquid whenever there is beam on target. What it translates into is the reduction of the measured normalized yield from the liquid (as the effective target thickness is smaller) and in turn has the effect of reducing the statistics accumulated in a given period of time. When doing experiments on liquid targets, both the above mentioned density effects are unavoidable. Therefore, it is necessary to reduce them until they become negligible on the time scale of the helicity change, 30 Hz for G^0. The basic computing unit for the PV asymmetry in this experiment is a quartet. A quartet stands for four consecutive helicity states, either having a structure like $+--+$ or $-++-$. The measured asymmetry is formed between the sum of normalized yield with positive helicity and the sum of normalized yield with negative helicity, in the same quartet, divided by the sum of all four. The FPD yields have been normalized to beam charge.

The 40 μA G^0 beam delivered by the CEBAF machine is very focused in space, nominally about 200 microns in both x and y. Not only would this beam boil a liquid target in its path but it may also damage the target system as it has power densities in the kW/mm^2. To mitigate this the beam is rastered uniformly over a larger area. In this experiment the raster shape is a square, nominally with a side of 2 mm, or an area of 4 mm^2. Two triangular signals are swept along x and y with frequencies f_x = 24.96 kHz and f_y = 25.08 kHz with a linear speed of 1000 m/s to yield a square pattern with a uniformity of 95%. In these target density studies measurements the goal was to determine the extra width due to target density fluctuations on the measured asymmetry width at the nominal running point in the experiment, beam at 40 μA, 3 GeV, rastered at 2x2 mm^2 and the cryogenic target pump rotating at 31 Hz.

Density fluctuations

Target density variations are assumed to depend on the dynamical state of the fluid in the interaction region, on the state in the phase space occupied by the fluid and on beam parameters. The only parameter that affects the dynamical state of the target fluid in the interaction zone is the cryogenic pump rotational speed. The pump directly dictates the speed of the flow at all points around the cryogenic loop, the interaction area included, and so it is responsible, along with the geometry of the loop, for the dynamical state of the fluid in the interaction region. The state occupied by the fluid in the thermodynamic phase space (p,T) also influences density fluctuations. In the case the density fluctuations are dominated by micro-bubble formation, a colder fluid has fewer micro-pockets reaching the liquid-vapor curve and so density variations effects are reduced. Target density variations are also influenced by beam properties like intensity, raster size and intrinsic beam spot size. To summarize, target density fluctuations may depend on target medium temperature, cryogenic pump rotational speed and beam raster size, intensity and intrinsic spot size. Measurements were made to assess target density fluctuations versus raster size, pump speed and target medium temperature. During each measurement only one parameter a time was varied.

During the first engineering run, the G^0 detector was segmented in two statistically independent detectors to check if the measured effect was concurrent. To separate deadtime corrections from target density fluctuations the electronics were used in the scaler mode. In this mode the electronics just counts detector hits, with basically no deadtime. The grand total statistics achieved when the whole detector was summed up was about 320 ppm asymmetry width per quartet, at a raster of 2x2 mm^2, providing sufficient resolution to measure density fluctuations down to tens of ppm. The density fluctuations were studied at constant beam current by changing the raster and this was repeated at different pump speeds. In the second engineering run data was taken in the same conditions as in the first engineering run (except for a different target cell). A newly instrumented detector set, the luminosity detectors or lumis, was also used in the second run.

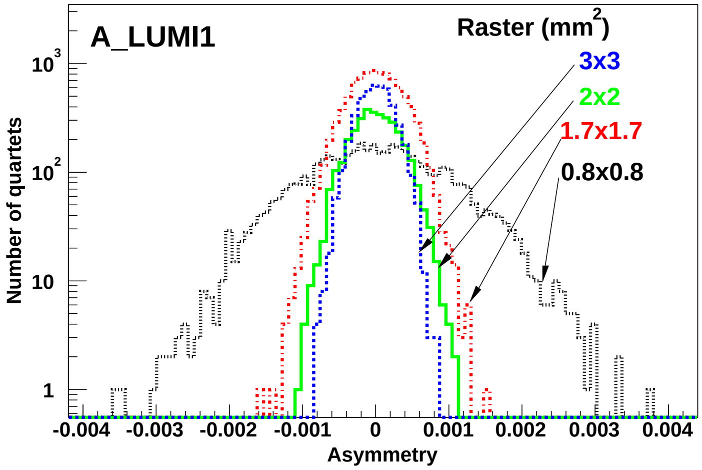

Figure B-1: Lumi1 asymmetry width at 40 μA beam and different raster sizes.

There were 8 lumi detectors placed in two sets of 4 at different locations along the beam line sensitive to very forward scattering, mostly Møller electrons and elastic electrons from e-e and e-p scattering in the target (from the beam line lumis 1-4 at 2° to the target, clocked at 45° in the x-y plane, and lumis 5-8 at 1.2° and along x-y axes, one up, one down, one left, one right).

A typical lumi detector asymmetry width is 200 ppm for a raster of 2 mm. Fig. (B-1) shows the variation of lumi1 asymmetry width with the raster size. Six of the lumis, 1-6, used photomultiplier tubes and two, 7 and 8, used vacuum photodiodes. Lumi 7 was malfunctioning during these studies and the data collected with it were discarded from the analysis. Each lumi detector was used as an independent measurement, no combinations were made. The lumis have higher statistics than the G^0 FPD and they have no deadtime (as their signals are integrated), which make them more suitable for measuring target density related effects. However, the lumis are also very sensitive to beam related effects that are independent of the target, like scrapping, halo etc..The plots below are from analysis of the data taken during the second engineering run.

A model for target density fluctuations was used to interpret the results obtained from data taken at constant beam current, constant pump speed and varying the beam raster. The asymmetry in a quartet is computed with

$$A = \frac{N^+ - N^-}{N^+ + N^-} = \frac{\Delta N}{N} \tag{B.1}$$

where ΔN = N^+ - N^-, N = N^+ + N^-, and N^+, N^- are number of detector hits per unit beam charge in the corresponding helicity state of a quartet. The width of the asymmetry in eq. (B.1) is given by $\sigma_A^2 = 1/N$ (which, in the absence of noise sources, is the detector's counting statistics). A source of noise that acts on the time scale of the helicity change will change σ_A into eq. (B.2). For a counting statistics dominated detector the noise source acts as a random perturbation and has the effect of enlarging the measured asymmetry width, eq. (B.2), subsequently the measured asymmetry width is given by

$$\sigma_m^2 = \sigma_0^2 + \sigma_b^2 \tag{B.2}$$

where σ_0 is the part of the detector asymmetry width independent of the beam raster (the asymptote of the asymmetry width when the raster goes to infinity), and σ_b (the index denotes *"boiling"*) encompasses all random noise sources that influence the detector's counting statistics and depend on the beam raster. In this model the assumption is that σ_b is dominated by target density fluctuations and depends on the beam raster size as an inverse power law

$$\sigma_b = \frac{\sigma_\rho}{r^x} \tag{B.3}$$

where σ_ρ is independent of raster size and r^x is the raster linear size to a power that can be a fit parameter or forced by a model to a specific value. Eq. (B.3) was compared to a fit with fixed raster size exponent $x = 2$, based on heuristic arguments that the extra width on the measured asymmetry is proportional to the size of the target density fluctuations and that target density fluctuations are inversely proportional to the target volume illuminated by the beam (which is the target length times raster area), $\sigma_b \sim \delta\rho \sim 1/A_{raster}$. Although the heuristic approach may be crude, it is a useful comparison.

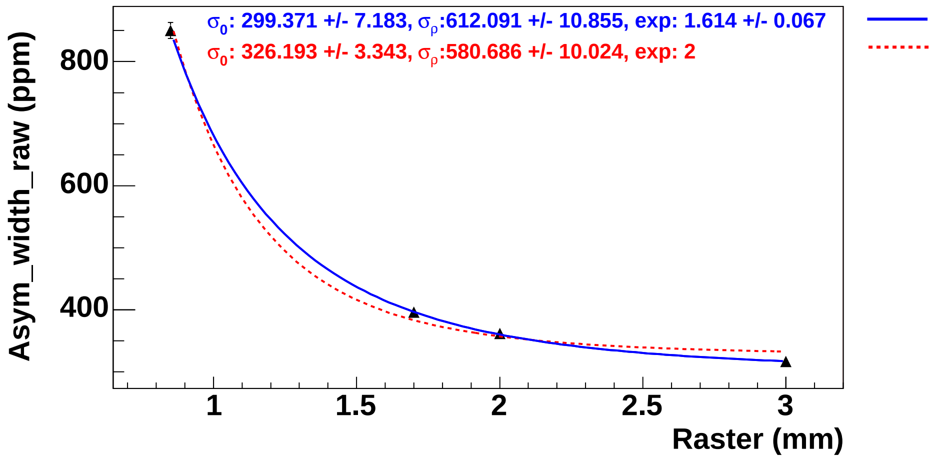

Figure B-2: G^0 detector asymmetry width. 40 μA beam - 31 Hz pump speed.

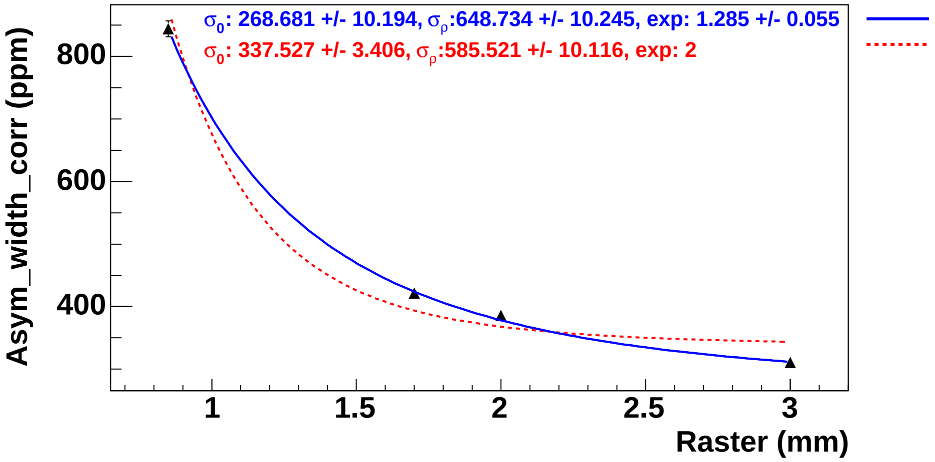

Figure B-3: G^0 detector beam linearly regressed asymmetry width. 40 μA beam - 31 Hz pump speed.

The measured asymmetry width versus raster size (see fig. (B-2), for example) displays a pronounced nonlinear behavior of the asymmetry width as a function of the raster size at constant beam and constant pump speed. Although the exact analytical dependence of the asymmetry width on the raster size is unknown it was found that an inverse power law eq. (B.3) fits the data well at 40 and 30 μA beam current. At lower beam currents the inverse power law works poorly, while the fixed power law ($x = 2$) works better. This may be due to the fact that as the beam intensity reduces, the density fluctuations decrease and the density becomes more or less constant on the time scale of a helicity state (30 Hz) over a wide range of raster sizes (which means that the heuristic arguments outlined above are holding better at lower beam currents). Both approaches were used to extract the density fluctuations versus raster size and they were compared. fig. (B-2) has the measured G^0 detector asymmetry width versus raster size with the beam at 40 μA and the pump rotating at 31 Hz. fig. (B-3) has the asymmetry width in the same conditions as fig. (B-2), but the asymmetries have been linearly regressed for beam parameter correlations (like positions and angles at the target, charge and energy). The solid line is the fit with three parameters (σ_0, σ_ρ, and x), while the dashed line is the fit for the heuristic model, with the raster exponent fixed ($x = 2$).

The results for the G^0 detector and the lumis at the nominal running point are summarized in the following table, where σ_b is extrapolated with eq. (B.3) to the nominal raster size of 2 mm (asymmetry width unit is ppm, fitting errors have been omitted for clarity):

Table B.1: Density fluctuation results, beam 40 μA, pump 31 Hz

Detector	exp x	σ_b	exp x	σ_{b_corr}
FPD	2	145.2	2	146.4
	1.61	199.9	1.3	266.2
Lumi 1-4	2	177.8	2	209.3
	1.61	236.6	1.56	295.8
Lumi 5-8	2	168.6	2	173.4
	1.55	237.9	1.48	304.4

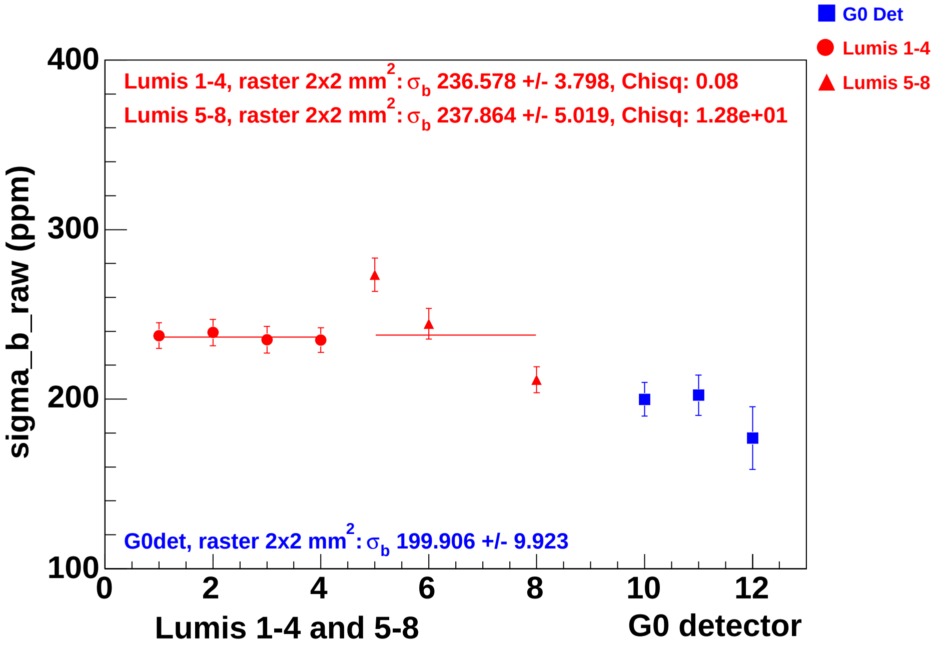

Figure B-4: Measured asymmetry width (beam 40 uA, pump 31 Hz).

Figs. (B-4, B-5) are a summary of the model extracted, eq. (B.3), target density fluctuations for the lumi and G^0 detectors at the nominal running point (beam 40 μA, raster 2x2 mm^2, and pump 31 Hz). Fig. (B-4) shows the extracted target density fluctuations from the measured detectors asymmetry widths. On the horizontal axis numbers 1-8 indicate the respective lumi detector (7 missing), number 10 denotes the G^0 detector, and numbers 11 and 12 denote the segmentation of the G^0 detector in two independent detectors, to check for concurrence of the extracted target effect (the two segments are summed in the analysis as the G^0 detector). The first 4 lumi detectors are in a remarkable agreement for the extracted target effect, lumis 5-8 are about 2 sigma away from each other, but average at the same value as lumis 1-4. The two segments of the G^0 detector measure similar effects between themselves (within 1 sigma), and their sum underestimates the σ_b extracted from the lumis data by 15%. Fig.B-5 shows the extracted σ_b from the corrected detectors asymmetry widths with the linear regression for beam parameters. After the linear regression was applied the extracted

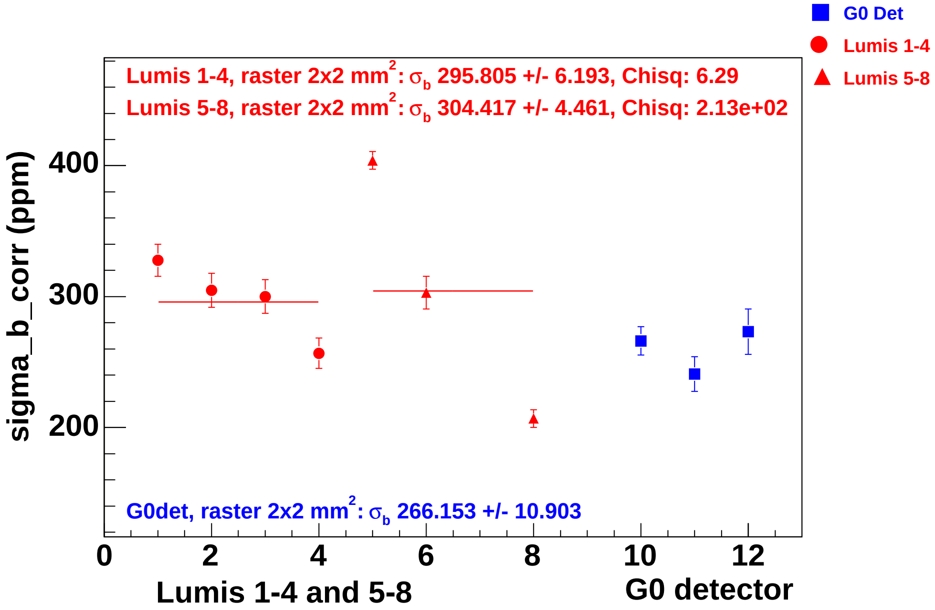

Figure B-5: Beam corrected asymmetry width (beam 40 μA, pump 31 Hz).

value for σ_b becomes larger. The increase is about the same, 60-65 ppm, for the average of lumis 1 to 4, the average of lumis 5 to 8 and the G^0 detectors. The individual data points are much more dispersed compared to the uncorrected data. Lumi 8 is the only detector whose extracted value for σ_b decreases with the regression. In our model, σ_b, defined by eq. (B.3), encompasses target and beam related effects. As a consequence it is expected that, after the asymmetry data are regressed for beam parameters, σ_b becomes smaller. In conclusion, it seems that the linear regression induces noise into the asymmetry measurement instead of subtracting it at a level of 65 ppm, consistent among the average of lumi 1-4, lumi 5-8 and the G^0 detectors. There are beam effects that cannot be extracted by a linear regression out of the asymmetry data, like scrapping and halo. For the nominal running conditions in the experiment (40 μA, 3 GeV beam rastered on a square of side 2 mm and with the pump rotating at 31 Hz) we quote an upper limit for target density fluctuations contribution to the asymmetry width of 240 ppm. In the normal running mode the asymmetries are measured in 16 Q^2 bins. The G^0 detector gets segmented accordingly, and in a typical Q^2 bin the asymmetry width is about 1200 ppm. A target related effect of 240 ppm on top of this nominal width increases the Q^2 bin asymmetry width by 2%, a negligible systematic effect for this experiment. Fig. (B-6) shows the extracted values for σ_b at 40 μA beam and two pump speeds, 31 and 42 Hz. Since there weren't enough data to make a model extraction (using eq. (B.3)) of the target density effect, the data for the two pump speeds have been compared to the heuristic approach ($x = 2$). The horizontal axis is the same as in figs. (B-4, B-5). The heuristic approach seems to extract consistent values for σ_b, at the same pump speed, among lumis and the two independent segments of the G^0 detector. In this approach a significant drop in the target density fluctuations is seen between the two states of the pump, 31 and 42 Hz, suggesting that the boiling contribution drops with a power of the frequency for this target (the power law favored by this approach is $\sigma_b \sim 1/f^3$.

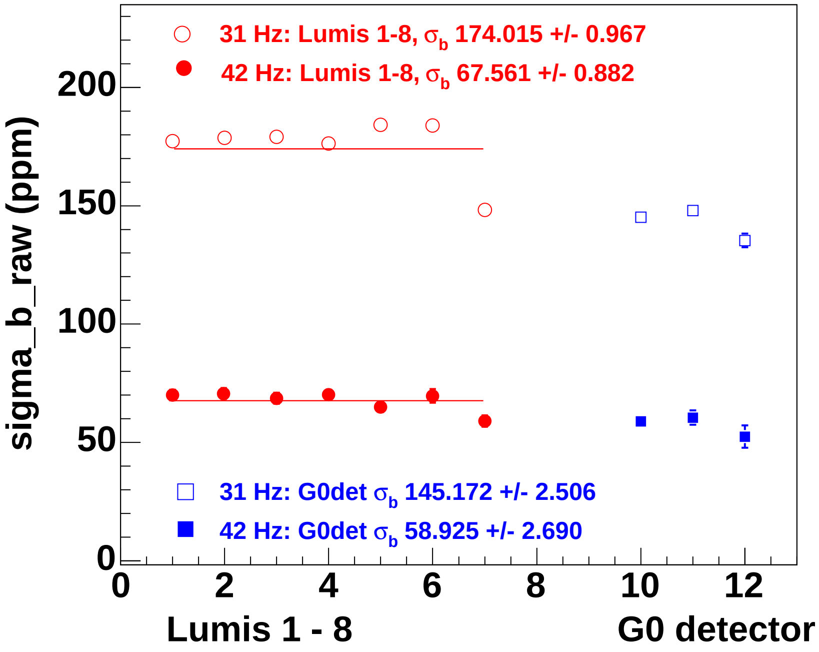

Figure B-6: Measured asymmetry width (beam 40 μA, pump 31 and 42 Hz).

The results from the first engineering run were analyzed with the heuristic approach, as there were not sufficient data at each beam current to make a fit with three parameters. However these results are about 20% lower than the results extracted with the same approach from the second engineering run. There were two changes in the running conditions that might be responsible for the increase in σ_b between the two runs. One difference between the two data sets was the in-beam thickness of the target cell exit window. As the thickness of the cell in beam was reduced 3.6 times between the two engineering runs it is expected that this change would reduce the target density fluctuations if it were to dominate them, and it should act opposite to the measured effect. Based on this it can be concluded that the density fluctuations in a target cell with high speed longitudinal fluid flow are not dominated by film boiling at the exit window. Another change was the intrinsic beam spot size, before rastering. The measured intrinsic beam spot size during the data taking for target boiling studies from the second engineering run was 0.107 mm in x and 0.03 mm in y, which is about ten times smaller than the nominal intrinsic beam spot size. There are, though, no direct studies to support the influence of the intrinsic beam spot size over target density fluctuations.

A study has been done to check the variation of the lumis asymmetry widths with the target mean temperature. Changing the target mean temperature between 18 and 21 K a 3% change in the lumis asymmetry widths was recorded [8], a negligible amount. This means that the density fluctuations mechanism in this target is not dominated by micro-bubble formation.

B.1.1 Density reduction

To extract the global FPD yield reduction versus beam current, and avoid deadtime corrections, data at the same beam current and different raster sizes were extrapolated to nominal raster size, different beam currents, but the same power density. In this approach a beam intensity of 40 μA and raster of 1 mm was assumed the same as 160 μA and raster of 2 mm, since in both situations the power density is the same on the target.

The slopes of the relative normalized FPD yield at two different beam currents, 40 and 30 μA, were measured versus beam extrapolated currents from different raster sizes and the results are shown in fig. (B-7), where ΔY is the relative normalized FPD yield with respect to the yield at 40 μA and at 30 μA respectively.

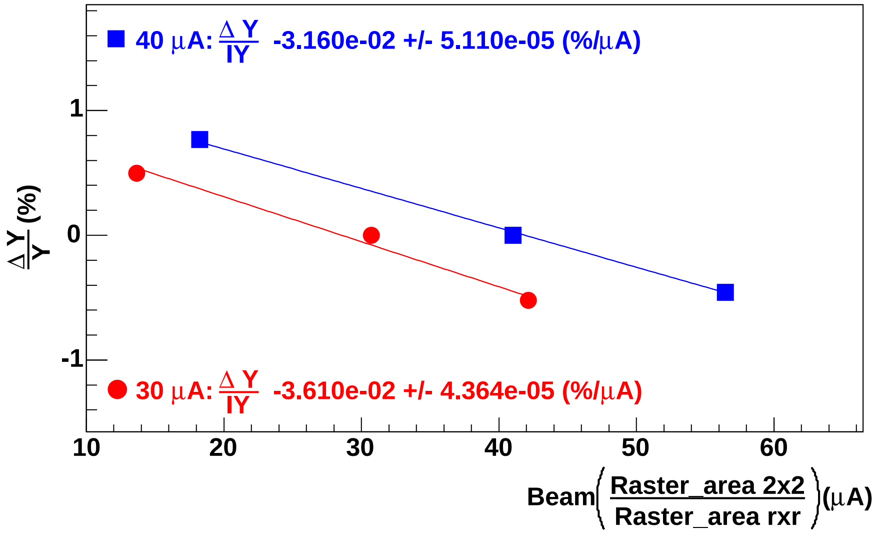

Figure B-7: Relative normalized FPD yield versus extrapolated beam current. Cryogenic pump rotating at 31 Hz.

At a pump speed of 31 Hz, the slopes measured with this indirect method are about the same at two different beam currents. The 40 μA measurement yielded -3.16e-2 $\pm$ 5.11e-5 (%/μA) and the 30 μA measurement yielded -3.61e-2 $\pm$ 4.36e-5 (%/μA). From these measurements it can be inferred that the global yield reduction when the pump rotates at 31 Hz is less than 1.5% at 40 μA beam on target. The same yield slope extraction approach at a pump speed of 42 Hz, yielded slopes one order of magnitude smaller than the slopes at 31 Hz.

The normalized yield reduction was also measured using the luminosity detectors. Since these detectors are not affected by deadtime, their yield reduction was determined by directly measuring the normalized yield versus beam current at a nominal raster size of 2 mm for each luminosity detector. The results are shown in fig. (B-8) for the six

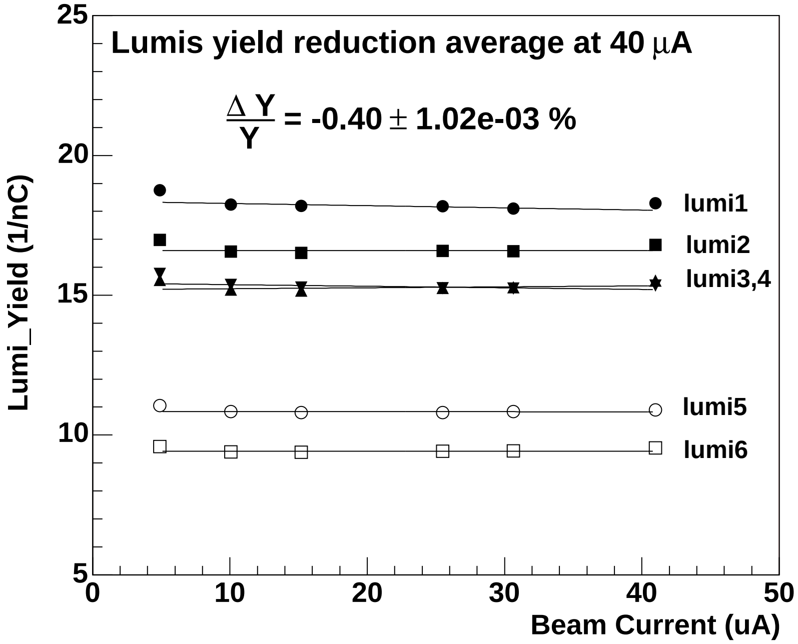

Figure B-8: Lumis 1-6 normalized yield slope versus beam current.

detectors instrumented with PMTs. The average yield reduction over the six luminosity detectors is 0.4%.

The FPD normalized yield reduction, due to the target, in the nominal running conditions in G^0 forward angle mode is negligible for this experiment.

Appendix C

Background subtraction

Tables with background interpolation under the elastic peak for dilution factors and asymmetry. Summary results presented in fig. (3-21).

Table C.1: FR FPD background under the elastic peak summary.

Det	FR					
	$f_b \pm \Delta f_b$(%)	$\Delta_{st} f_b$(%)	$\Delta_{sys} f_b$(%)	$A_b \pm \Delta A_b$(ppm)	$\Delta_{st} A_b$(ppm)	$\Delta_{sys} A_b$(ppm)
1	11.00±0.56	0.43	0.36	0.69±5.85	4.14	4.14
2	14.41±0.85	0.43	0.73	-8.77±4.08	3.22	2.51
3	15.96±0.70	0.45	0.53	-8.94±3.51	3.00	1.81
4	16.12±0.80	0.49	0.63	-9.80±3.67	3.20	1.80
5	17.25±0.71	0.50	0.51	-1.51±3.57	3.00	1.94
6	17.91±0.78	0.50	0.78	-7.41±8.37	2.91	7.85
7	17.68±0.82	0.49	0.65	-8.43±3.39	2.98	1.62
8	18.69±0.77	0.55	0.53	-15.84±5.00	3.08	3.94
9	19.10±0.71	0.54	0.45	-11.42±3.75	2.79	2.28
10	19.58±0.82	0.57	0.59	-7.39±7.79	3.03	7.17
11	21.31±1.17	0.60	1.01	-10.60±5.20	2.97	4.27
12	24.09±1.53	0.70	1.36	4.15±6.48	3.05	5.72
13	21.12±1.79	0.73	1.64	2.96±5.23	3.58	3.81
14	23.16±0.99	0.76	0.63	6.04±9.22	3.37	8.58

Table C.2: NA FPD background under the elastic peak summary.

Det	NA					
	$f_b \pm \Delta f_b$(%)	$\Delta_{st} f_b$(%)	$\Delta_{sys} f_b$(%)	$A_b \pm \Delta A_b$(ppm)	$\Delta_{st} A_b$(ppm)	$\Delta_{sys} A_b$(ppm)
1	13.72±1.23	0.52	1.11	-6.50±6.24	3.78	4.97
2	20.48±3.44	0.58	3.40	-4.27±3.27	2.59	2.00
3	18.33±1.36	0.57	1.23	-6.56±3.61	3.09	1.87
4	16.93±2.36	0.54	2.29	-8.64±5.20	3.16	4.12
5	14.32±2.17	0.48	2.11	-6.94±5.06	3.25	3.88
6	15.43±1.83	0.47	1.77	-11.58±3.00	2.99	0.18
7	25.75±4.84	0.66	4.79	-14.37±2.91	2.39	1.65
8	17.70±2.18	0.55	2.11	-4.24±3.22	3.01	1.15
9	24.95±1.19	0.71	0.95	-4.72±3.02	2.73	1.29
10	21.43±3.75	0.64	3.69	-0.84±5.84	2.98	5.02
11	25.00±3.62	0.71	3.55	-7.08±3.03	2.60	1.56
12	24.15±3.08	0.81	2.97	-10.78±5.03	3.23	3.86
13	21.82±2.32	0.78	2.18	6.81±3.98	3.34	2.17
14	29.15±6.01	1.02	5.92	10.83±4.35	3.18	2.97

Bibliography

[1] R. Frisch and O. Stern, *Z. Physik* 85, 4 (1933).

[2] R. Hofsttadter, *Phys. Rev.* 35, 48 (1956).

[3] A. O. Bazarko et al., *Z. Phys.* C65, 189 (1995).

[4] J. Ellis and R. L. Jaffe, *Phys. Rev.* D9, 1444 (1974); *Phys. Rev.* D10, 1669 (1974).

[5] Particle Data Group, *Phys. Lett.* B592, (2004).

[6] R. L. Jaffe and A. V. Manohar, *Nucl. Phys.* B337, 509 (1990).

[7] J. Gasser et al., *Phys. Lett.* B253, 163 (1991).

[8] S. J. Dong et al., *Phys. Rev.* D54, 5496 (1996).

[9] S. V. Wright et al., *Nucl. Phys.* A680, 137 (2000).

[10] D. Kaplan and A. V. Manohar, *Phys. Lett.* B310, 527 (1988).

[11] R. D. McKeown, *Phys. Lett.* B219, 140 (1989).

[12] D. H. Beck, *Phys. Rev.* D39, 3248 (1989).

[13] T. D. Lee and C. N. Yang, *Phys. Rev.* 104, 254 (1956).

[14] C-S. Wu et al., *Phys. Rev.* 105, 4 (1957).

[15] M. J. Musolf et al., *Phys. Rep.* 239, 1 (1994).

[16] F. Halzen and A. D. Martin, *Quarks and Leptons: An Introductory Course in Modern Particle Physics*, John Wiley & Sons, New York (1984).

[17] D. H. Beck and B. R. Holstein, *Int. J. Mod. Phys.* E10, 1 (2001).

[18] D. J. Griffiths, *Introduction to Elementary Particles*, John Wiley & Sons., New York (1987).

[19] F. J Arnst, R. G. Sachs, and K. C. Wali, *Phys. Rev.* 119, 1105 (1960).

[20] R. G. Sachs, *Phys. Rev.* 126, 2256 (1962).

[21] Haiyan Gao, *Int. J. Mod. Phys.* E12, 1 (2003).

[22] G. A. Miller, *Phys. Rev.* C 57, 1492 (1998).

[23] S. Galster et al., *Nucl. Phys.* B 32, 221 (1971).

[24] A. Liesenfeld et al., *Phys. Lett.* B 468, 20 (1999).

[25] J. Friedrich and Th. Walcher *Eur. Phys. J.* A 17, 607 (2003).

[26] E. J. Brash et al., *Phys. Rev.* C 65, 051001 (2002).

[27] I. Zel'dovich, *JTEP Lett.* 33, 1531 (1957).

[28] S.-L. Zhu et al., *Phys. Rev.* D 62, 033008 (2000).

[29] D. H. Beck and R. D. McKeown, *Ann. Rev. Nucl.* 51, 189 (2001).

[30] M. J. Ramsey-Musolf and H. Ito, *Phys. Rev.* C 55, 3066 (1997).

[31] M. J. Ramsey-Musolf, *Proceedings*, PAVI02 Workshop, Mainz, Germany, June 2002.

[32] H.-W. Hammer et al., *Phys. Lett.* B 562, 208 (2003).

[33] T. R. Hemmert et al., *Phy. Lett.* B 437, 184 (1998).

[34] S. J. Dong et al., *Phys. Rev.* D 58, 074502 (1998).

[35] R. Lewis et al., *Phys. Rev.* D 67, 013003 (2003).

[36] G. Höhler et al., *Nucl. Phys.* B 114, 505 (1976).

[37] R. L. Jaffe, *Phys. Lett.* B 229, 275 (1989).

[38] J. F. Donoghue and B. R. Holstein, *Phys. Lett.* B 436, 331 (1998).

[39] M. J. Ramsey-Musolf and M. Burkardt, *Z. Phys.* C 61, 433, (1994).

[40] M. J. Ramsey-Musolf et al., *Phys. Rev.* D 55, 2741, (1997).

[41] R. Machleidt, *Adv. Nucl. Phys.* 19, ed. J. W. Negele and E. Vogt, Plenum, New York (1989).

[42] W. Koepf et al., *Phys. Lett.* B 288, 11 (1992).

[43] T. Cohen et al., *Phys. Lett.* B 316, 1 (1993).

[44] V. Bernard et al., *Nucl. Phys.* B 308, 753 (1988).

[45] H. Wiegel et al., *Phys. Lett.* B 353, 20 (1995).

[46] A. Silva et al., *Phys. Rev.* D 65, 014016 (2002).

[47] C. Y. Prescott et al., *Phys. Lett.* B 77, 347 (1976).

[48] D. T. Spayde et al., *Phys. Lett.* B 583, 79 (2004).

[49] T. M. Ito et al., *Phys. Rev. Lett.* 92 102003 (2004).

[50] K. A. Aniol et al., *Phys. Rev.* C 69, 065501 (2004).

[51] F. E. Maas et al., *Phys. Rev. Lett.* 93 022002 (2004).

[52] L. M. Bartoszek et al., *Internal G^0 report G0-96-003*, May (1996).

[53] G^0 Collaboration, *Jefferson Lab experiment 00-006*, D. H. Beck spokesperson. 383 (1996).

[54] G^0 Collaboration, C.E. Jones and E.J. Beise, *The G0 Liquid Hydrogen Target Preliminary Design Document* Internal Report, November 25, 1998.

[55] E.J. Beise et al., *Nucl. Instr. and Meth.* A378 (1996) 383.

[56] G^0 Collaboration, E.J. Beise et al., *The G0 Target Controls Manual*, Internal Report, revised February 2004.

[57] G^0 Collaboration, R.Carr and S. Covrig, *The G0 Target User's Guide*, Internal Report, October 2002.

[58] H. Y. Wong, *Handbook of essential formulae and data on heat transfer for engineers* published 1977.

[59] G. Smith, *private communication*, February 2004.

[60] N. F. Mott, *Proc. Roy. Soc.* (London) A13, 429 (1932).

[61] SAMPLE Collaboration, S. P. Wells et al., *Phys. Rev.* C 63 (2001) 064001

[62] J. Roche et al., *Internal G^0 report G0-02-071*, August (2002), and ref. therein.

[63] R. Clark and B. Quinn, *Internal G^0 report G0-98-010*, June (1998), and ref. therein.

[64] G. Batigne, *Mesure du contenu etrange du nucleon: experience G^0*, Ph.D. thesis, Universite Joseph Fourier - Grenoble 1, Dec. (2003)

[65] A. Biselli, *Internal G^0 report G0-03-088*, September (2003).

[66] J. W. Müller, *Nucl. Inst. Meth.* 117, 401 (1974).

[67] G. Niculescu, some internal cebaf report...

[68] Jefferson Lab, website *www.jlab.org*

[69] M. Baylac et al., PAVI2002, *Mainz Parity Workshop Proceedings*, November (2002).

[70] C. K. Sinclair, *Proc. Part. Acc. Conf.*, New York (1999).

[71] J. M. Grames, *Measurement of weak polarization sensitivity* Ph.D. thesis, University of Illinois at Urbana-Champagne, (1994).

[72] M. Loppacher, *Moller polarimetry for CEBAF Hall C*, Dissertation, Universität Basel, (1996).

[73] Hall C website, *http://www.jlab.org/Hall-C/equipment/Moller/moller.html*

[74] D. Spayde website, *http://www.jlab.org/ spayde/beam-polarization.html*

[75] Cebaf Online Data Aquisition, *http://coda.jlab.org*

[76] Experimental Physics and Industrial Control System, *http://www.aps.anl.gov/epics*

[77] ROOT, *http://root.cern.ch*

[78] MySQL, *http://www.mysql.com*

[79] W. R. Leo, *Techniques for Nuclear and Particle Physics Experiments*, second revised ed., Springer-Verlag, Berlin, (1994).

[80] K. Nakahara, *Internal G^0 report G0-03-096*, September, (2003).

[81] E. R. de Beaumont, *Internal G^0 report G0-98-031*, Octomber, (1998) & *Internal G^0 report G0-99-035*, June, (1999).

[82] L. Hannelius, *Internal G^0 reports G0-03-044 and G0-03-102*, (2003).

[83] GEANT, *http://wwwasdoc.web.cern.ch/wwwasdoc/geant_html3/geantall.html*

[84] J. Arvieux, *private communication*, June, (2004).

[85] G. Batigne et al., *Internal G^0 report G0-03-002*, February, (2003).

[86] K. Nakahara, *private communication*, August, (2004).

[87] J. Dahlberg, *private communication*, Nov. 1, (2002).

[88] G^0 Collaboration, *Internal G^0 report G0-04-002*, May, (2004).

List of Figures

List of Tables